



# **Evolution and dynamic properties of photospheric plasma in solar active regions**

**Jose Iván Campos Rozo**

Universidad Nacional de Colombia  
Facultad de Ciencias, Observatorio Astronómico Nacional  
Bogotá, Colombia  
2017



# **Evolution and dynamic properties of photospheric plasma in solar active regions**

**Jose Iván Campos Rozo**

Tesis o trabajo de grado presentada(o) como requisito parcial para optar al título de:  
**Magister en Ciencias-Astronomía**

Supervisor:  
Doctor Santiago Vargas Domínguez

External Supervisor:  
Doctor Dominik Utz

Línea de Investigación:  
Solar Astrophysics  
Grupo de Investigación:  
Group of Solar Astrophysics (Grupo de Astrofísica Solar)

Universidad Nacional de Colombia  
Facultad de Ciencias, Observatorio Astronómico Nacional  
Bogotá, Colombia  
2017



**“There is nothing new under the sun.  
It has all been done before.”—Sherlock Holmes**

I dedicate my Master thesis work to my family and many friends. A special feeling of gratitude to my loving mother, María Helena Rozo H. whose words of encouragement and her own tenacity ring in my ears. My brothers, Manuel Felipe and Juan Carlos, who are always working so hard for me and my family. Finally, I dedicate my work to Adriana Ibeth Martínez, who has never left my side and is indeed a very special and kind person.

I had a project for my life which involved 10 years of wandering, then some years of medical studies and, if any time was left, the great adventure of physics.

Che Guevara



## Acknowledgements

I wish to thank my supervisors Santiago Vargas Domínguez and Dominik Utz who were more than generous with their expertise and precious time, and more than that, they have been my friends and supported me along the way for completing this thesis work. A special thanks goes to professor Benjamín Calvo Mozo, my boss, guide and friend for his countless hours of reflecting, guidance, encouraging, and most of all, his patience, throughout the entire process since my undergraduate times. Thank you Islena Bonilla who is the institute secretary and the most helpful woman that I know. I would like to acknowledge and thank the whole staff of the Observatorio Astronómico Nacional for allowing me to accomplish my research and providing every assistance requested. Special thanks goes to the members of staff development and human resources department for their continued support.

I also thank my friends in my home town who have supported me throughout the process. I will always appreciate all of what they have done for me, especially my patroness Anaceida Martínez for helping me to develop my personal skills and for her friendship, and I want to say thank you to Dayhana Rojas, thanks because you always forced me to continue in my firsts steps at the University.

Finally I would like to thank my former teachers, mentor-teachers, and the administrators in our University that assisted me with this project.



## Resumen

Este trabajo se ha realizado para la iniciación en la investigación del autor en el área de la física solar. El trabajo está dividido en dos partes. La primera parte da una visión global de los temas relacionados con la física solar dando un viaje a través del Sol, desde el interior pasando por todas sus capas hasta la atmósfera solar.

La segunda parte hace una presentación de las herramientas computacionales que se usan en el presente trabajo. Se han desarrollado librerías por parte del autor para el grupo de desarrolladores internacionales del paquete de Python para física solar, SunPy. En esta parte también se muestra un bosquejo de la técnica de seguimiento de correlación local o LCT por sus siglas en inglés. Por último, en esta introducción se presenta la aplicación de interfaz gráfica desarrollada para análisis preliminares de la aplicación del algoritmo de LCT. Los últimos dos capítulos están centrados en el estudio de los flujos horizontales y verticales en regiones activas solares. Se utilizan observaciones ya calibradas del instrumento HMI (Heliographics Magnetogram Imager) a bordo del telescopio espacial SDO (Solar Dynamics Observatory), tales como mapas de intensidad en el continuo y magnetogramas en la línea de visión o LOS por sus siglas en inglés. Se hace una descripción del pre-tratamiento necesario para obtener datos co-alineados y un filtrado para remover ciertas vibraciones naturales del Sol llamadas modos-p, necesario para el estudio temporal. Sobre estos cubos de datos se hace el tratamiento de correlación local, obteniendo los flujos horizontales y verticales de las regiones observadas. Tras haber encontrado ciertas estructuras y comportamientos peculiares, se hace un análisis similar usando los magnetogramas en la línea de visión; se compara el comportamiento tanto del plasma en las imágenes de continuo como las estructuras magnéticas en los magnetogramas. Teniendo los flujos horizontales de ambas observaciones podemos cuantificar y analizar los resultados obtenidos infiriendo una fuerte relación entre la emergencia de celdas mesogranulares, rápidas regiones de plasma ascendente y la emergencia de campo magnético positivo.

En el último capítulo se muestra un análisis de regiones activas seleccionadas basado en el criterio que sus penumbras no rodean totalmente la umbra, mostrando que en regiones donde no existe la penumbra no se encuentran flujos radiales salientes conocidos como flujos de moat.

**Palabras clave:** 1) Flujos de Moat. 2) Física Solar. 3) Correlación Local. 4) Análisis de Imágenes. 5) Atmósfera Solar. 6) Manchas Solares. 7) Movimientos Propios.

# Abstract

This work has been done for the initiation of the author into the field of solar physics. The work is divided in two main blocks. The first part gives an overview of topics in solar physics taking a journey from the center of the Sun starting in the solar interior through different layers up to the solar atmosphere.

The second part presents the computational tools used in this work as well as the development of several libraries created by the author for the international community of solar physics research. These routines were included into the packages for solar physics analysis (SunPy). Moreover, a sketch of the Local Correlation Tracking (LCT) technique is also outlined. A GUI application developed for preliminary analysis for the LCT algorithm is presented in the second part. The last two chapters of this block are focused on the study of horizontal and vertical flows in solar active regions. For this purpose, we used two datasets obtained and calibrated from the HMI (Heliographics Magnetogram Imager) - an instrument on board of the SDO (Solar Dynamics Observatory) spacecraft - that are continuum intensity maps and magnetograms in the line of sight (LOS). The following chapter describes the necessary pre-treatment procedure in order to obtain co-aligned datasets. For a proper temporal study, the so-called p-modes were removed applying a filtering routine. A local correlation tracking technique has been applied to obtain the horizontal and vertical flows of the selected regions. We compare the behavior of plasma flows measured in the continuum with the motion of magnetic structures. We found a strong relationship between the emergence of mesogranular cells, fast rising regions of plasma and the emergence of positive magnetic fields. In the last chapter, an observational analysis of active regions has been performed. The criterion used to select these sunspots is based on their umbrae lacking fully developed penumbra around them (partial penumbrae). The results indicate that in regions where there is no penumbra there is no radial outward flows, so-called moat flows, detectable around the sunspot.

**Keywords:** 1) Moat Flows. 2) Solar Physics. 3) Local Correlation. 4) Images Analysis. 5) Solar Atmosphere 6) Sunspots. 7) Proper Motions.

# Contents

<b>Acknowledgements</b>	vii
<b>Resumen</b>	ix
<b>I A brief Introduction to the Sun</b>	<b>2</b>
<b>1 From the Inner Structure to the Solar Atmosphere</b>	<b>3</b>
1.1 General Concepts . . . . .	3
1.2 Inner Structure . . . . .	5
1.3 The Solar Atmosphere . . . . .	6
<b>2 Solar Activity</b>	<b>15</b>
2.1 Introduction . . . . .	15
2.2 Explosive Phenomena . . . . .	16
2.3 Solar Cycle . . . . .	19
2.4 Active Regions . . . . .	21
<b>II Computational Tools, Algorithms, and the Investigation of Photospheric Proper Motions</b>	<b>25</b>
<b>3 Python for Solar Physics</b>	<b>26</b>
3.1 SunPy . . . . .	27
3.2 Algorithms and Computational Tools . . . . .	31
3.3 GUI for LCT Analysis . . . . .	37
<b>4 Study of Sunspots and Pores by means of Local Correlation Tracking Techniques</b>	<b>39</b>
4.1 Observations . . . . .	39
4.2 Data . . . . .	39
4.3 Emergence of Magnetic Fields in Exploding Granules . . . . .	45
<b>5 Identification of Moat Flows around Sunspots</b>	<b>103</b>
5.1 Introduction . . . . .	103
5.2 Observations and Data . . . . .	103
5.3 Masking Velocities to outline Moat Flows . . . . .	106
5.4 Moat Flows around Sunspots . . . . .	110
<b>6 Summary</b>	<b>113</b>
<b>Bibliography</b>	<b>115</b>

## **Part I.**

# **A brief Introduction to the Sun**

# 1. From the Inner Structure to the Solar Atmosphere

This chapter gives a brief description of basic features of the solar atmosphere and the different processes taking place at each of the solar atmospheric layers. See Fig. 1-1;

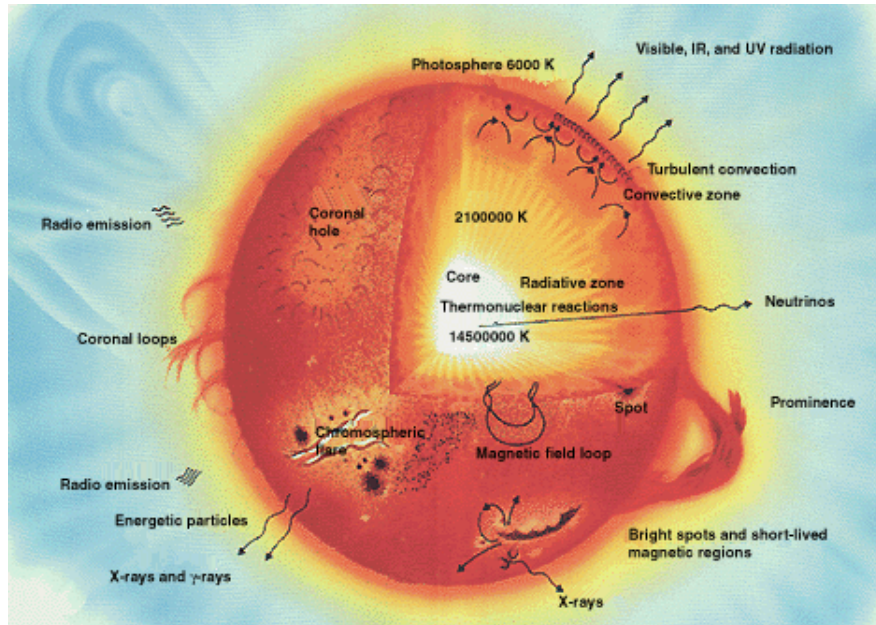


**Figure 1-1.:** A general sketch showing the multitude of basic features of the Sun and its overall structure.  
Image Credit: Calvin J. Hamilton (Views of the Solar System).

## 1.1. General Concepts

Due to the essential role that the Sun plays for the life on Earth (photosynthesis processes and weather, among others), from time immemorial the human being has always focused in our star, which has also been culturally significant within religions and beliefs. Furthermore, from a physical point of view, the Sun is the closest star to our planet, which gives us the opportunity to study in highest detail different physical processes that takes place in it, being, in this way, the best stellar laboratory. Basically, its unique proximity enables to

obtain information with high spatial and temporal resolutions<sup>1</sup>.

The most important basic features of our star can be summarized as follows<sup>2</sup>

- Age: formed roughly 4.6 billion years ago.
- Spectral classification: G2V star on the main sequence within the Hertzsprung-Russel diagram.
- Effective surface temperature: Close to 5770 K.
- Mass: roughly  $2 \times 10^{30}$  kg.
- Radius: approximately  $7 \times 10^8$  m.
- Distance from Sun to Earth: In the order of  $1.5 \times 10^{11}$  m or also known as one Astronomical Unit (AU).
- Luminosity: roughly  $4 \times 10^{26} W$ .

Although solar observations have been reported several centuries ago, the first systematic observations of the Sun were registered by Galileo Galilei<sup>3</sup>. But it was not until the middle of the twentieth century when humans conquered the space putting the firsts space telescopes into orbit and thus finally enabling completely new fascinating discoveries. This is due to the fact that Earth's atmosphere is not entirely transparent to the whole electromagnetic spectrum, allowing only a few observational windows (e.g. optical, infrared, or radio, as shown in Fig. 1-2).

Due to the little observational window (see Fig. 1-2) on the ground, the first attempts to do measurements with balloons that observed the solar ultraviolet radiation was in 1934 [Schmidtke, 2015]. The first solar space-mission was brought to space after the World War II; it was a german V-2 rocket observing far ultraviolet radiation. This experiment was executed in 1946, followed by others measuring X-rays in 1948, hard X-rays, and finally  $\gamma$ -rays in 1958. These technological developments represented a decisive milestone to study and understand the different solar atmospheric layers and a significant attempt to cover the entire electromagnetic spectrum. Recently, permanently deployed space telescopes provide new opportunities to obtain solar data steadily giving us access to yet unknown physical processes and secrets of the Sun.

---

<sup>1</sup>The second closest star to our planet is Proxima Centauri at a distance of roughly 4.22 light-year.

<sup>2</sup>This information is based on the information obtained from the solar fact sheet <http://nssdc.gsfc.nasa.gov/planetary/factsheet/sunfact.html>. Accessed: 2017-02-15

<sup>3</sup>His drawings were published in the letters that Galileo wrote to Marcus Wesler.

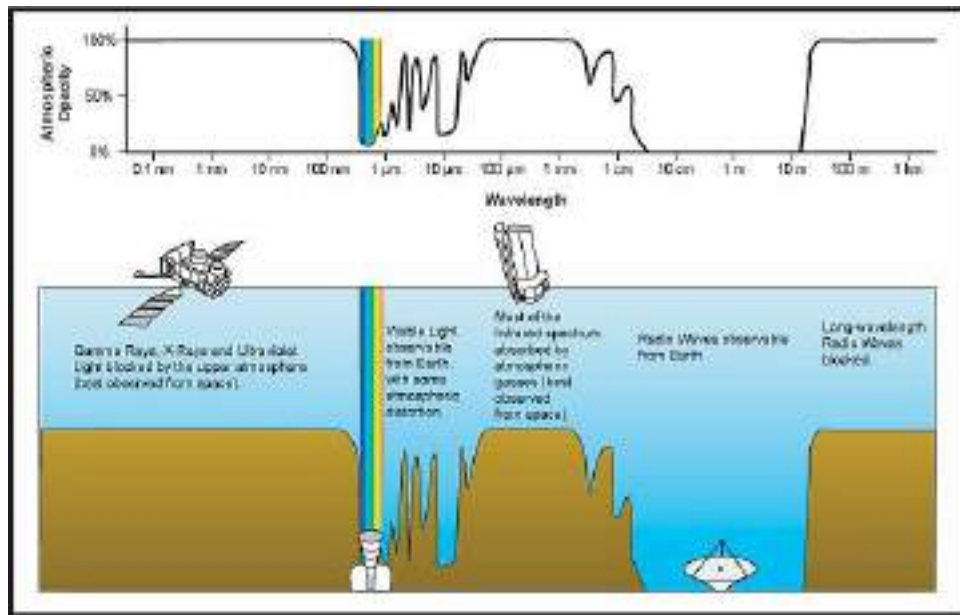


**Figure 1-2.**: Sketch showing the wavelength bands in which the propagation of photons through the Earth's atmosphere is allowed. Such bands are commonly called “observational windows”. Taken from: [http://coolcosmos.ipac.caltech.edu/cosmic\\_classroom/ir\\_tutorial/irwindows.html](http://coolcosmos.ipac.caltech.edu/cosmic_classroom/ir_tutorial/irwindows.html)

## 1.2. Inner Structure

Based on observations and theoretical modelling, the current understanding of the physics of the Sun suggests that it is structured as sketched in Fig. 1-1.

### The Core

The solar interior, according with the standard model, consists basically of three regions: the core, the radiative zone, and the convective zone. The emitted energy of the star is produced in its core by nuclear reactions [Bethe, 1939]. The plasma temperature and density are high enough to provide suitable physical conditions to trigger thermonuclear processes which are “burning” or fusing Hydrogen atoms into Helium mainly via the so-called proton-proton chain process [Gombosi, 1998].

### The Radiative Zone

Next to the core resides the radiative zone, in which the generated energy is transported via radiation. Due to the high plasma density the photon mean free path<sup>4</sup> is very short. Because of the high number of photon scattering events, the energy produced in the core

<sup>4</sup>The mean free path describes the average distance a photon can travel between two scattering events.

requires even hundreds of thousands of years to be transported through the radiative zone [Mitalas and Sills, 1992], to finally reach the interface region called tachocline. This region covers from about  $0.28 R_{\odot}$  to roughly  $0.7 R_{\odot}$  [Dwivedi and Narain, 2006].

## The Convective Zone

Continuing moving radially outwards, we find the onset of this layer at roughly  $0.7 R_{\odot}$ , according to [Rieutord and Rincon, 2010]. The temperature starts to drop and the Rosseland mean opacity (quantity that represents the ability of plasma to absorb radiation), increases rapidly. Due to this increase in opacity, the ability of the plasma to transport energy via photons decreases. The large temperature gradient in the convective zone generates plasma convective instabilities [Schwarzschild, 1958]. These instabilities subsequently cause hot bubbles of gas to start to rise up from the radiative zone boundary and eventually expand, releasing the hot material transported to the upper boundary of the convective zone, displaying typical upflowing velocities of  $1-2 \text{ km s}^{-1}$  [Title et al., 1986].

The convective instability is given when the absolute temperature gradient value is larger than the absolute adiabatic temperature gradient [Hansen, 1994].

### 1.3. The Solar Atmosphere

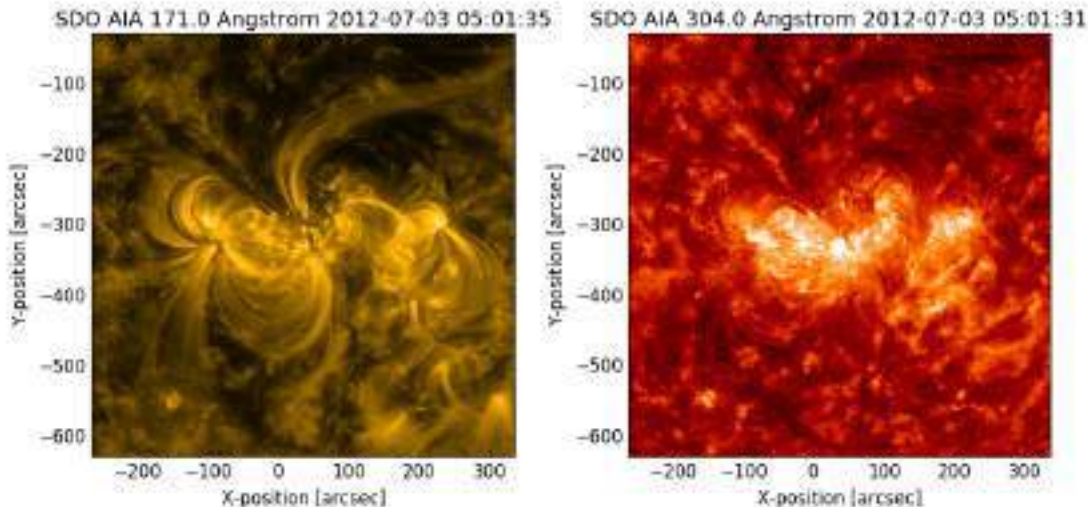


**Figure 1-3.:** On the left: magnetic loops embedded in the solar corona are observed with the AIA instrument (Atmospheric Imaging Assembly) on board the Solar Dynamics Observatory (SDO) in the  $171 \text{ \AA}$  channel. On the right: filaments can be seen in the upper solar chromosphere with SDO/AIA  $304 \text{ \AA}$  channel.

The so-called solar atmosphere embodies the region from the solar surface (photosphere)

to the corona. Normally, the solar atmosphere is divided in four layers, starting from the photosphere, followed by the chromosphere, the transition region, up to the corona. Within each of the atmospheric layers, a large amount of magnetic structures exist and evolve. Features as diverse as chromospheric filaments and magnetic loops in the corona (Fig. 1-3), or photospheric granules (Fig. 1-4), have been observed and studied throughout the solar atmosphere, being spatially and temporally very dynamic.

In the following paragraphs the different atmospheric layers will be described in more detail.

## The Photosphere

The photosphere, or light sphere, originates at a depth where the opacity is not sufficiently large anymore to block the light from escaping outwards. Its effective temperature is 5770 K with a thickness of about 500 km at  $\tau_{5000} = 1$ . The mean gas pressure in the photosphere is  $P_g \sim 10^4 \text{ Pa}$ <sup>5</sup>. As the temperature is comparably low in this region, particles are less ionized and the electron density is also lower. Due to these conditions, photons can easily escape from the surface without interruption. However, the photosphere is not a uniform region. As evidenced in high-resolution images, the photosphere is formed by irregular structures continuously moving. Different structures can be observed within the photospheric granulation pattern so-called convection cells or granules. Three different configuration sizes have been proposed within the granulation: granulation, mesogranulation, and supergranulation, depending on the spatial scale covered.

Solar granulation, the smallest of these patterns, is composed by granules whose central part is brighter than the edges due to rising hot material ( $0.4 \text{ km s}^{-1}$ ) which is then turned horizontal becoming an outwards moving plasma flow ( $0.25 \text{ km s}^{-1}$ ), to finally be turned into downflows at the edges [Title et al., 1986, Hathaway, 2000].

## Photospheric Magnetic Field

In the solar photosphere, the magnetic field is not structured in a simple way, i.e. in the sense of consisting solely of homogenous and unidirectional magnetic fields. On the contrary, the magnetic field consists of a number of large- and small-scale magnetic elements moving randomly as well as evolving rapidly. However, these structures are arranged in different ways to form magnetic structures. Some of these observable larger features are:

- Sunspots: They are large concentrations of magnetic field on the photosphere, which can be, in theory, even observed from Earth by naked eye and will be described in more detail in Chapter 2.
- Plage regions: Although plages are bright regions usually associated to chromospheric features (observed mostly in the spectral line CaK ( $3933.7\text{\AA}$ ), and situated specially

<sup>5</sup>Taken from the Sun Fact sheet in <http://nssdc.gsfc.nasa.gov/planetary/factsheet/sunfact.html>

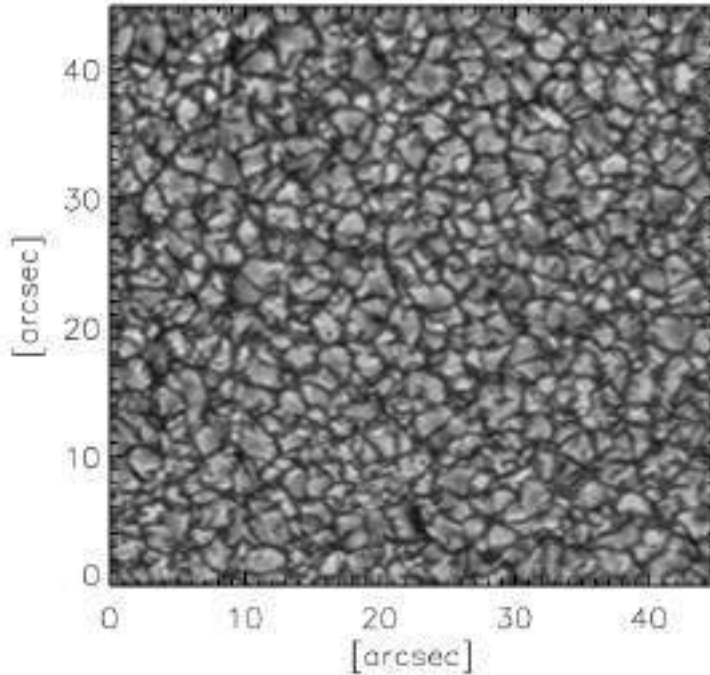


**Figure 1-4.:** High definition filtergram taken with SUNRISE/IMaX in the continuum of the Fe I ( $5250.2\text{\AA}$ ) line. The image shows granulation in high resolution. Date: 2009-06-09 in the range between 01:30:54 and 02:02:29 UT [Danilovic, 2010].

around sunspots), they can also be observed in the photosphere, evolving next to a sunspot and being even larger than the area occupied by the sunspot itself. In the photosphere the magnetic elements of the plages can be measured with mean magnetic field strengths of up to several hundreds of Gauss.

- Most of the photospheric magnetic fluxes, within the quiet Sun (outside active regions), are concentrated in the middle of the granular boundaries - in the so-called granular lanes. Such network fields could be made up of Magnetic Bright Points (MBPs; e.g. see Fig. 1-5; [Utz et al., 2009]), or magnetic knots or other small-scale magnetic field concentrations. Such vertical magnetic flux tubes exhibit normally strong intensities as well as strong magnetic fields which can reach a strength of up to a kG. Such small-scale magnetic fields are observed in spectropolarimetric data or magnetic fields sensitive filtergrams like the well-known G-band ( $4305\text{ \AA}$ ; e.g., [Schüssler et al., 2003, Utz et al., 2014]).

## The Chromosphere

The chromosphere, or color sphere, is the second layer of the solar atmosphere (from surface to outside). Its name comes from the observation of solar eclipses in which the Sun seems

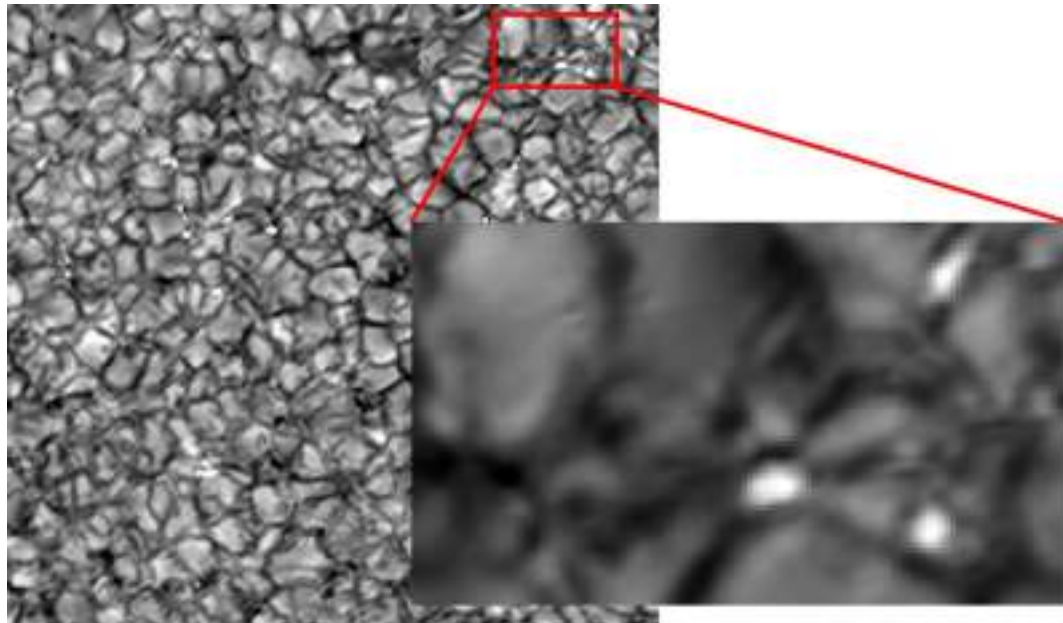


**Figure 1-5.:** Image of convective cells in the solar photosphere (granules). Intergranular bright regions are areas where magnetic flux tubes are located. They emerge out of a concentration of magnetic fields and open up in the higher atmosphere as well as they appear partially evacuated (having lower plasma densities) in their footpoints. Due to this evacuation, these regions allow us to look deeper into the solar interior, i.e., into regions where the Sun is hotter, and thus there is an enhancement in brightness as well as in contrast compared to their surroundings. The bright points are approximately 100 kilometers in diameter. The shown image was taken by the instrument IMaX during a flight of the balloon-born Sunrise mission. Taken from: <https://www.mpg.de/research/sunrise-reveals-suns-magnetic-building-blocks>

to form a bright colored edge around the solar disk. Whereas the photosphere shows mostly spectral features consisting of absorption lines, the chromosphere presents many emission lines. The strongest lines that can be detected in the chromosphere are emission lines of Hydrogen as  $H_{\alpha}$ ,  $H_{\beta}$ ,  $H_{\gamma}$  and  $H_{\delta}$  centered at wavelengths of 6563, 4861, 4340, and 4102 Å respectively. Several other interesting lines can be found centered at 5876 Å (Helium), as well as at 3968 and 3934 Å (ionized Calcium lines CaII h and k, respectively) [Mullan, 2010]. In the standard model of the solar atmosphere [Rutten, 2002], “the chromosphere spans from the minimum temperature of the photosphere to the lower part of the transition region”. The temperature increases monotonically through the chromosphere as shown in Fig.(1-6) and grows very abruptly within the transition region (a region between the chromosphere and the solar corona).

### The Chromospheric Network

Images taken in any chromospheric spectral lines reveal prominent spatial structures, mostly called chromospheric network. Although apparently this network seems to be similar to that observed in the upper photosphere, it consists of areas featuring a high brightness contrast along the edges of the supergranulation (in the wings of  $H\alpha$ ; e.g., [Bonet et al., 1982]), but it looks broader and the areas covered by this network are larger. These bright areas are related to magnetic flux concentrations. Several distinguishing features can be identified and related to the chromospheric network [Athay, 1976]. Other features that can be observed in the chromosphere are the so-called spicules (Fig.1-7). Spicules are thought to play an important role in the mass and energy balance of the chromosphere [De Pontieu, 2007a]. They have an upward mass flux 100 times larger than the necessary to support the solar wind. However, the creation of spicules remains still a mystery and it has not been answered satisfactorily yet. Unfortunately, the detailed mechanism responsible for their creation is still not fully understood. Anyhow, there is a strong evidence that this mechanism is related with magnetic fields in an intrinsic way. Spicules at the limb are related to on-disk fibrils as well as to bright and dark mottles [Simnett et al., 1997].

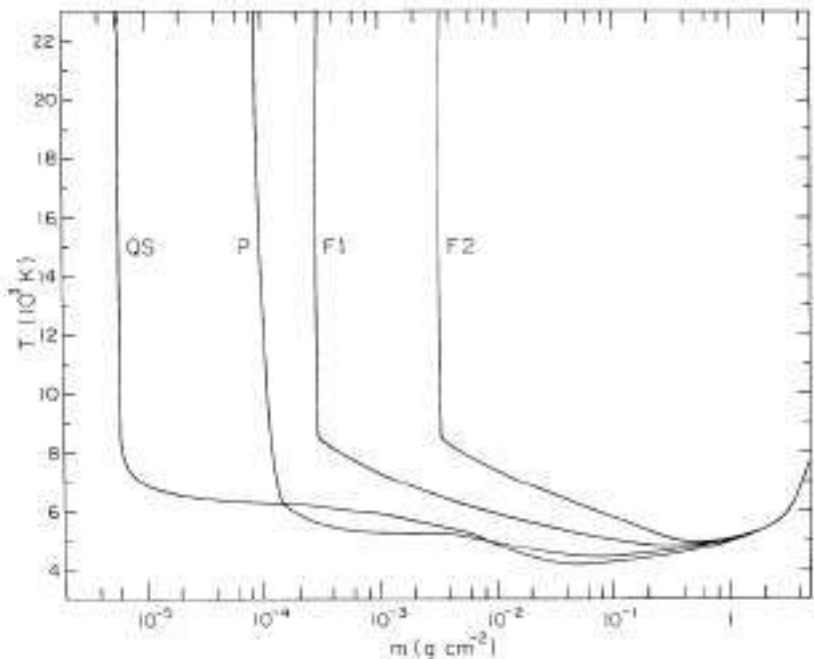


**Figure 1-6.**: Variation of temperature with the column mass. Qs represents quiet Sun atmospheric model; P represents Plage model and F1, F2 stand for two different flare models [Machado et al., 1980].

### The Magnetic Cover

Observations made at the solar limb using chromospheric lines show the presence of large areas of almost horizontal magnetic fields. It is believed that for quiet Sun regions, at a height of about 700-1000 km from the surface, the atmosphere starts to be completely filled up with magnetic fields due to the expansion of these fields with the decreasing gas pressure at higher atmospheric heights. The formed structure is known as the magnetic canopy. This is a layer of magnetic field which is parallel to the solar surface and is located at the lower chromosphere. The magnetic field strength in this region is about  $100\text{ G}$  and covers a large region of the “magnetic field free”<sup>6</sup> solar photosphere [Steiner, 2000].

Different structures can be observed in the chromosphere

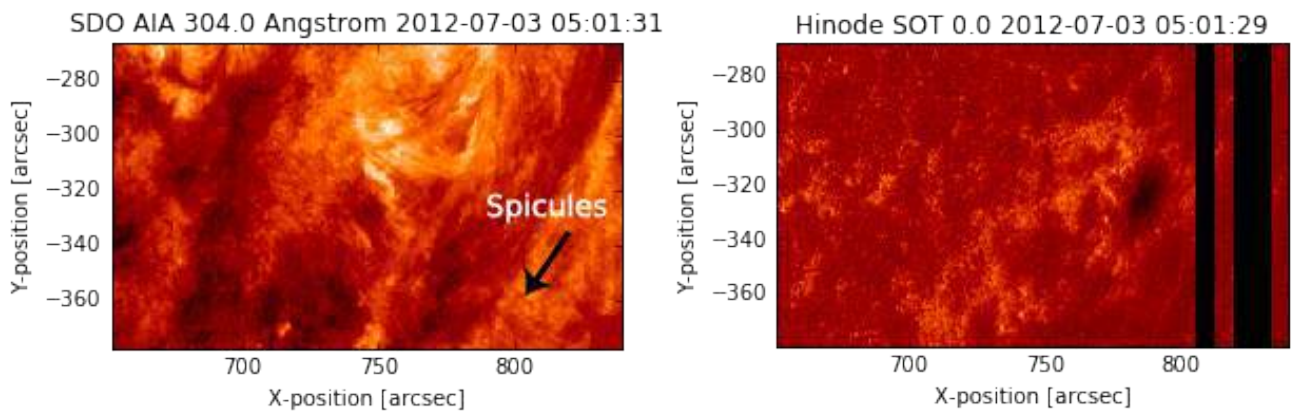


**Figure 1-7.:** On the left panel, an image of an active region taken with SDO/AIA in channel 304 Å is shown. The right panel displays, the same area, but observed by HINODE/SOT in Ca II H (3969.6 Å) line.

### Transition Region

The transition region is a thin and anomalous layer located between the upper chromosphere and the corona. This region is very relevant because it has a steep gradient in temperature, and the density falls rapidly from its lower region (about 20,000 K) to its upper one (around 1,000,000 K). The most prominent emission lines in the transition region emit in the ultraviolet segment of the solar spectrum and provide information concerning the structure and the displayed features in this layer. The spectral range of the AIA instrument on board

<sup>6</sup>In this context field free means that there are no extended active regions or large clusters of strong magnetic fields. In reality, there is most likely not a single real “field free” region in the solar atmosphere.

the SDO space telescope is able to acquire images in multiple bandpasses of UV and EUV. Three channels of AIA (171 Å, 304 Å and 1600 Å) observe parts of the transition region<sup>7</sup> (see Fig.1-8).

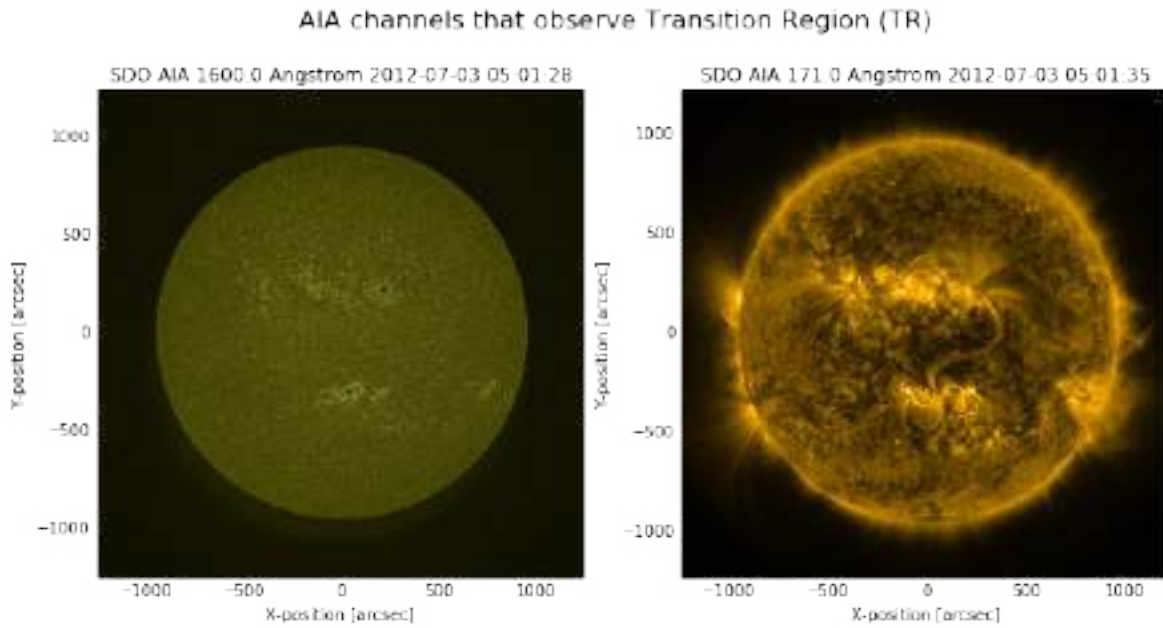


**Figure 1-8.:** Images of the solar transition region acquired with the NASA/Solar Dynamics Observatory (SDO); on the left: AIA channel 1600 Å imaging upper chromosphere and transition region; on the right: AIA channel 171 Å showing the quiet corona and upper transition region observed on July 3, 2012 at 05:01:35 UT.

The dynamics of the transition region is rapid and intense, causing energetic events occurring multiple times in the order of tenths of a second. Such energetic events are mainly triggered by magnetic reconnection, e.g. producing nanoflares within the quiet solar atmosphere [Moses et al., 1994] which seem to concentrate on regions of strong magnetic chromospheric network but avoiding the center of the cells in the network. Nevertheless, estimates of [Cook et al., 1987] suggest that these processes are not enough to heat the transition region to the measured elevated temperatures.

## The Corona

Likewise, as for the first observations of the chromosphere, the corona was observed and named due to its color and shape during a total solar eclipse (see Fig.1-9). Based on this astronomical event, the astronomers figured out a way to observe the corona by creating artificial solar eclipses, blocking the light coming from the Sun's disk, with an instrument

<sup>7</sup>for more information we refer to <http://aia.lmsal.com/public/instrument.htm>

called coronograph. The first observations of the visible spectrum of the corona showed emission lines in wavelengths corresponding to an element, which was unknown by the early observers of that epoch (second half of the 19th century). The observers hence suggested the existence of “coronium”, a new atomic element, as the main constituent of the solar corona. The corona is the last and outermost atmospheric layer of the Sun. With the help of the coronographs and special filters (usually UV and EUV), one can observe many structures in the corona, e.g. such as prominences or loops. The mystery of the coronium was solved when the astronomers determined the high temperatures in the corona observing the coronal spectral emission (i.e. during the 1929 eclipse; [Grotrian, 1931, Dollfus, 1953]). At such temperatures Hydrogen and Helium (the two most abundant elements) are completely peeled of their electrons, and less abundant elements such as C, N or O are also almost entirely ionised.



**Figure 1-9.:** Photography taken during a solar eclipse over the Marshall Islands in July 2009 in which the complexity of the solar coronal configuration can be recognized; Photo: Miloslav Druckmuller / SWNS

Only the heaviest elements, such as iron, retain traces of their electrons at these intense temperatures. The emissions of these highly ionized elements produce the spectrum that was once a mystery. Figure 1-10 shows a composite map of three channels of AIA/SDO enabling diagnostics of the plasma from temperatures starting at 600 thousand to 2 million Kelvin. It is worth mentioning a few of the significant features to be found in the corona: coronal holes, dominated by open magnetic field lines; complex magnetic loops of active regions and their small-scale counterparts, the bright points; and finally, quiet coronal regions consisting of more diffuse magnetic loops.

Coronal heating is still an open problem in the field of solar physics. It is clear that a physical process “must” exist that injects energy into the corona and thus increasing the temperature of the coronal plasma. This heating process should contribute much more than the radiation emitted by the photosphere. The debate has focused on the convective zone, which produces more than enough mechanical energy flux, but the question of how this energy is transported and converted into heat is still under debate. Several mechanisms have been proposed trying to solve this mystery, i.e. nanoflares [Parker, 1988], Alfvén waves [De Pontieu, 2007b, McIntosh, 2011] and spicules [De Pontieu, 2009, De Pontieu, 2011], among others.

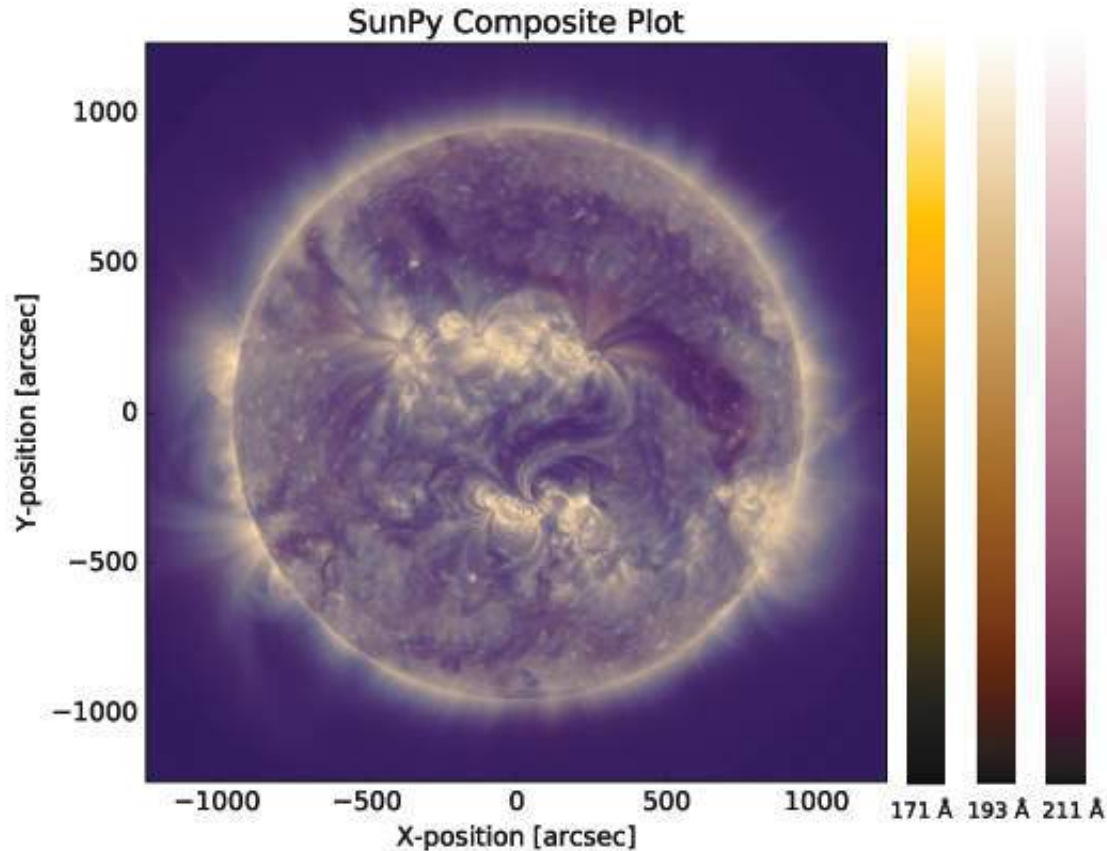


**Figure 1-10.:** Composite map of three channels of AIA/SDO, 171 Å, 193 Å and 211 Å. The solar images were acquired on July 3, 2012. Multiple channels or filters are used to register different solar features in simultaneously registered images. The different temperaturae associated to each channel can be verified in the instrument web-page <http://aia.lmsal.com/public/instrument.htm>. On the other hand, SunPy has developed different colormaps associated to different instruments and channels. The color maps associated with the channels in this plot are displayed in the color bars.

## 2. Solar Activity

### 2.1. Introduction

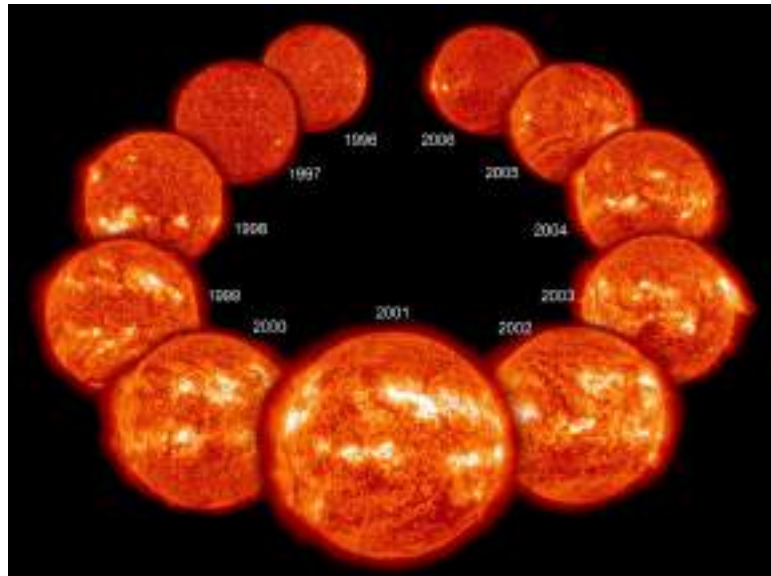


**Figure 2-1.:** The figure displays images of the solar disk covering solar cycle 23. Changes in solar activity, indicated by the varying bright areas on the solar disk, can be seen over a typical duration of 11 years. Image Credit: ESA&NASA/SOHO

Nowadays, it is well known that the Sun is not a passive sphere of gas. With the advances in solar instrumentation, observational techniques and modelling, it has been revealed that the Sun displays a large variety of dynamic processes that often result in eruptive events. All these different events are considered as part of the solar activity. The more general definition may include different features comprising explosive phenomena, coronal activity, interplanetary transients or geomagnetic variations. Over the years it has been revealed that the solar activity undergoes a cycle (which was initially associated to the number of sunspot on the solar disk), with a period of approximately 11 years, in which the Sun depicts more or less activity, i.e a higher or lower number of the above mentioned events.

## 2.2. Explosive Phenomena

Solar activity is strongly related to explosive phenomena at different spatial and temporal scales. The most energetic explosive events taking place in the Sun are solar flares and Coronal Mass Ejections (CMEs). Both phenomena are very complex processes associated directly with different magnetic features.

### Flares

Solar flares are considered the most energetic phenomena in the Solar System, releasing energies of the order of  $10^{33}$  ergs in just a few minutes and they are believed to be triggered by magnetic field lines reconnection [Shibata and Magara, 2011] (see Fig. 2-2).

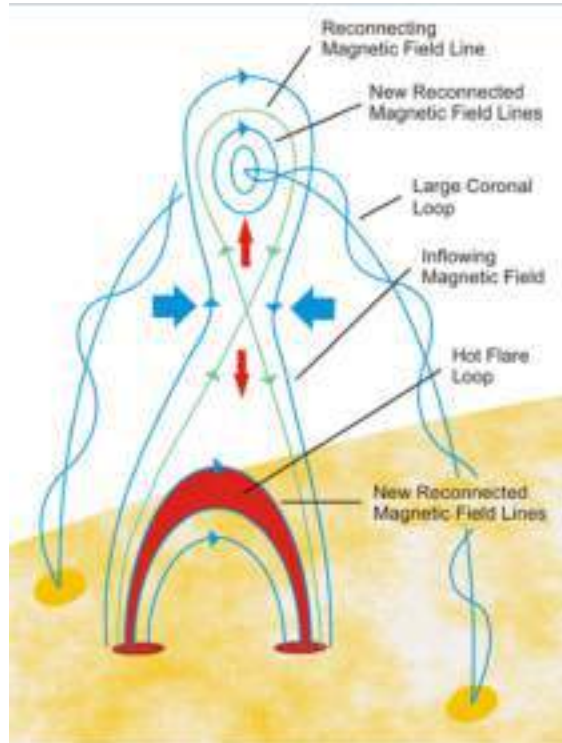


**Figure 2-2.:** An illustrated model of magnetic reconnection and solar flare diagram. Image Credit: Gordon Holman and NASA, all rights reserved.

At such reconnection sites particles are strongly accelerated and start to travel downwards along the newly reconnected magnetic field loops with speeds of up to  $150,000 \text{ km s}^{-1}$  [Harra, 2000]. Another possible trigger leading to flares [Vargas Domínguez et al., 2012], and references there in, may be related to the emergence of magnetic flux in the lower atmosphere, interacting with pre-existing ambient magnetic fields, hence reconfiguring the topology of the field lines and eventually leading to reconnection and the subsequent energy

release (see Fig.2-4). Understanding different stages in the evolution of a flare such as impulsive and decay phases has been possible by ever improving observations in different wavelengths.

## Coronal Mass Ejections

Solar activity associated to Coronal Mass Ejections (CMEs) is also very captivating to investigate as CMEs triggering sources can vary, as well as the eruptive candidate structure. Among the studied possibilities are large structures of “trapped” plasma known as prominences. These phenomena are usually observed using coronagraphs (see Fig.2-3). The detected light is generated by scattering of photons from plasma ejected from the Sun and traveling at speeds of hundreds of kilometers per second [Hundhausen, 1999]. While it became clearer in recent years that flares and CMEs are not directly related, they are still linked phenomena and both associated to changes in the magnetic field topology. It means that pre-existence of a flare, before a CME takes place, is not the only precursor associated as the CME triggering mechanism. Different descriptions have been proposed to understand the physics and processes of different kinds of prominences. A summary of the most important schemes explaining how prominences are related to CMEs is given in [Gilbert et al., 2000].

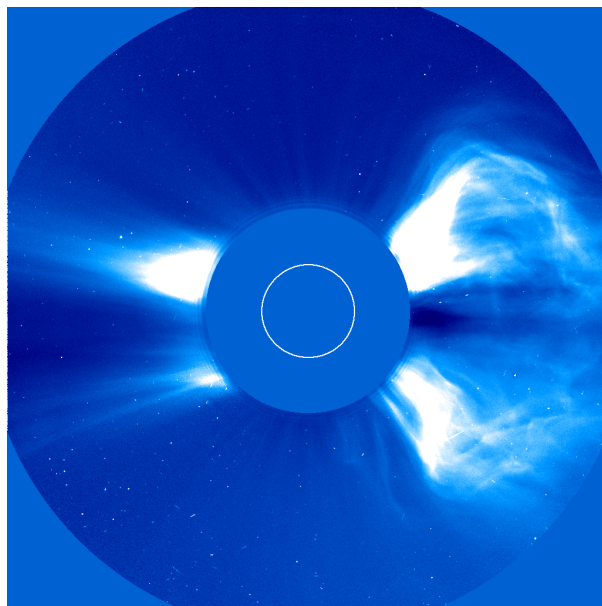


**Figure 2-3.:** Image of a CME from SOHO/LASCO C2 (a coronagraph imaging in white light from 2 to 6 solar radii) at April 7, 1997. Image taken from: <http://helios.gsfc.nasa.gov/cme.html>

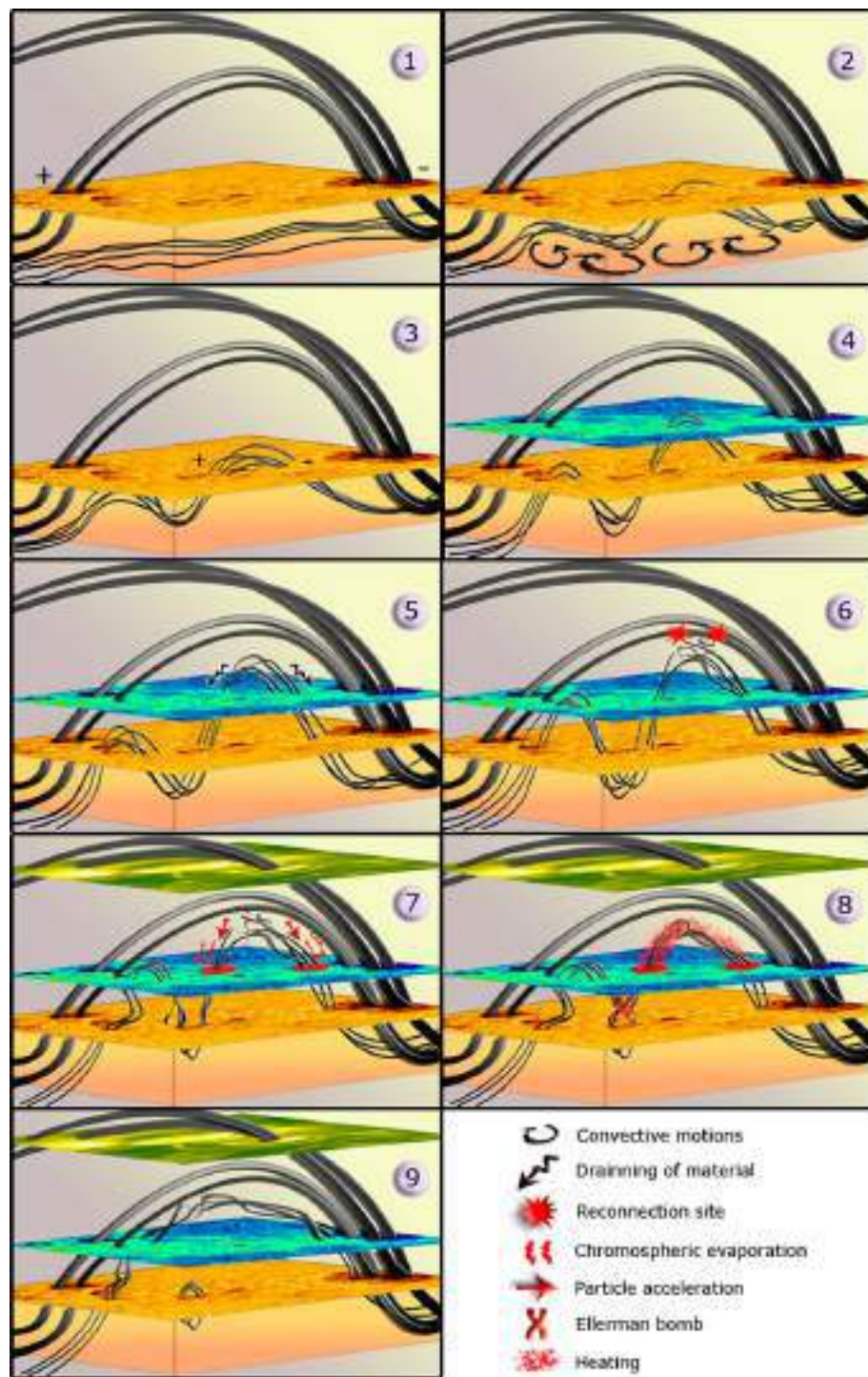


**Figure 2-4.**: Sketch representing the multiple scales of magnetic flux emergence in the solar atmosphere. The cartoon shows the action of an emerging magnetic flux through the solar atmosphere leading to reconnection reconfiguring the topology of the magnetic field lines and generating energy release [Vargas Domínguez et al., 2012].

## 2.3. Solar Cycle

As mentioned before, the presence of sunspots, or the associated Active Region (AR), is a sign of the solar activity. The first mentioning of the existence of a possible periodic behavior of sunspots was made by Christian Horrebow in 1776. But it was [Schwabe, 1844], who observed the change in the sunspot activity and found a periodic cycle. With observations made by Wolf, he published in 1861 an easier way to count the number of sunspots as well as keep a track record of the sunspots, not by handling spots individually but as groups of sunspots, which incorporates both isolated sunspots as well as group of sunspots:

$$R = \kappa(10g + n) \quad (2-1)$$

where  $\kappa$  is a correction factor that depends on the observation (telescope and/or observatory),  $g$  is the identified number of sunspot groups and  $n$  is the number of individual spots. The temporal evolution of  $R$  can be seen in Fig.2-5.

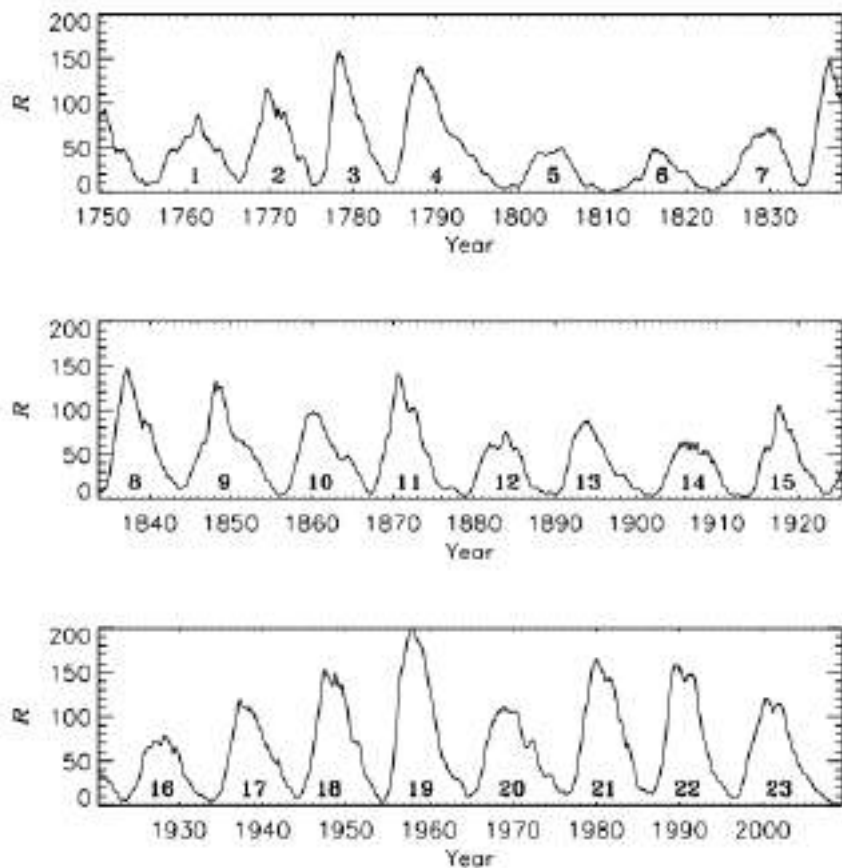


**Figure 2-5.:** The whole time series of the monthly relative sunspot numbers monitored during the period 1749-2009 is plotted with the conventional sunspot cycle numbering [Petrovay, 2010].

Walter E. Maunder noticed that taking into account the measures of the area of sunspots and active regions, and their position on the solar disk, an apparent movement from mid-latitudes to the Equator occurs in a period of 11 years. Maunder plotted the distribution of the sunspots areas and latitudes (Fig. 2-6) and created, by doing so, the famous “Butterfly Diagram” [Maunder, 1904].

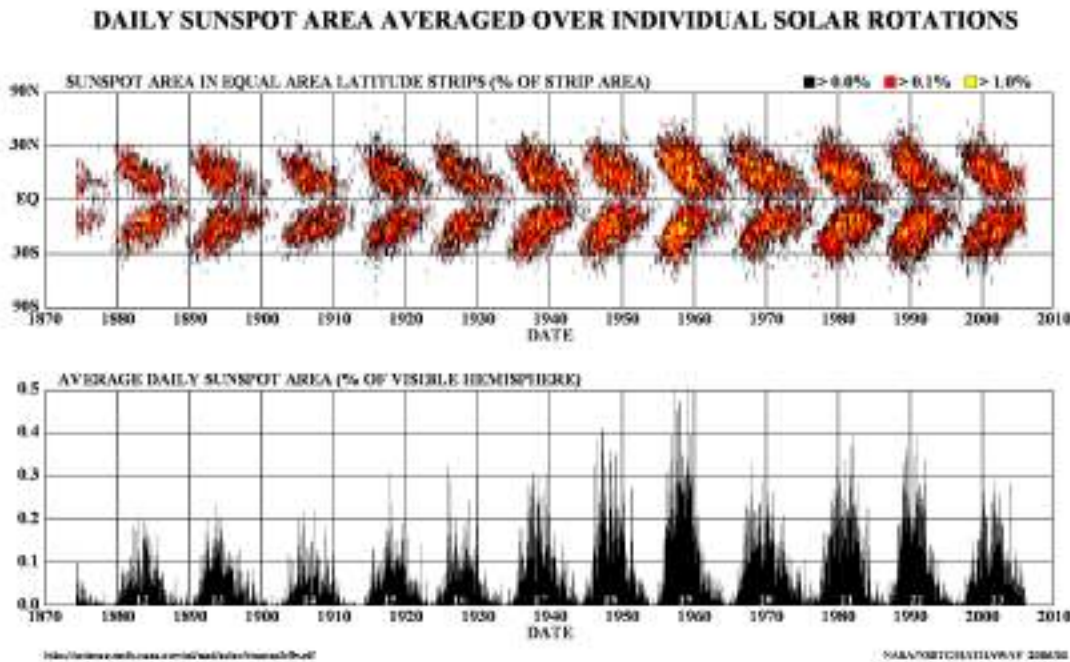


**Figure 2-6.**: Top: Latitude vs time of the surface area occupied at a certain time and latitude with sunspots. Bottom: average daily sunspot area over the visible hemisphere. Taken from: [http://www.nasa.gov/vision/universe/solarsystem/solar\\_cycle\\_graphics\\_prt.htm](http://www.nasa.gov/vision/universe/solarsystem/solar_cycle_graphics_prt.htm)

Furthermore, [Hale, 1908] made the first measurements of magnetic fields in sunspots, and by plotting different measures over several years [Hale et al., 1919] found a strong relationship between the solar cycle and the solar magnetic field. When one employs a tracking routine similar to the one for the sunspots, but applied instead to the change of the magnetic fields, one can create a “Magnetic Butterfly Diagram” (see Fig. 2-7).

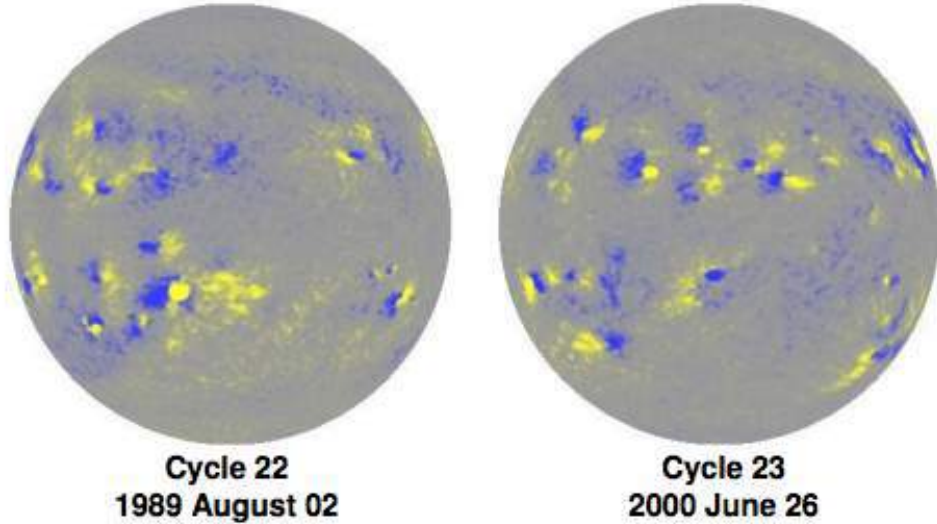


**Figure 2-7.:** Comparison between two full-disk magnetograms obtained from the SoHO/MDI (Michelson Doppler Imager). On the left panel, a magnetogram of cycle 22 (August 2, 1989) is depicted and on the right panel, an image of cycle 23 (June 23, 2000). In the map the yellow color indicates positive polarity regions and blue denotes regions of negative polarity. One can also notice that the polarities between the two hemispheres have changed between a cycle and the subsequent one [Hathaway, 2015].

## 2.4. Active Regions

Many authors (e.g. [Parker, 1970]) believe that the origin of the solar magnetic fields resides in the solar interior below the convective zone. Some others, e.g. [Brandenburg, 2011], propose the Negative Effective Magnetic Pressure Instability (NEMPI) as one alternative candidate. In this work, the first idea on the origin of the magnetic field will be followed without losing sight of the other alternatives. It is widely accepted that steadily large amounts of magnetic field are emerging from the solar interior to the surface and that they appear in different forms and scales, such as large-scale active regions (AR) or, on smaller scales, intra-network fields (INF), Magnetic Bright Points (MPBs) among others. It is believed by some authors (e.g. [Babcock, 1961, Leighton, 1964, Leighton, 1969, Guerrero and Käpylä, 2011]) that these magnetic fields are generated in a subsurface layer beneath the convective zone, the so-called tachocline. Based on observations and theoretical considerations, it is accepted by several theories that AR are the result of the emergence of magnetic flux tubes rising upwards through the solar interior due to magnetic buoyancy and the action of the convective transport.

Most of the observable magnetic activity (activity caused by magnetic fields) takes place

within AR. During the evolution of such regions a whole range of different kinds of phenomena can occur. For example, when new magnetic flux emerges within an older pre-existing magnetic configuration, the additional flux forces the magnetic field to re-configure on small, as well as on large, scales (Fig. 2-4).

## Formation, evolution and decay of sunspots

Solar magnetic activity is largely responsible for the majority of phenomena occurring in the solar atmosphere, of which sunspots are the most prominent manifestation. Magnetic activity provides us with several clues about the solar behavior in the near surface as well as on upper atmospheric layers. Solar active regions (sunspots and plages) are regularly classified and labeled by numbers in the order of their appearance on the solar disk. The commonly used identifier for AR is assigned by NOAA (National Oceanic and Atmospheric Administration) and can be found in a corresponding catalog. Nowadays it is known [Solanki, 2003] that sunspots are complex magnetic structures with sufficiently strong magnetic fields to suppress convective processes in the photosphere and thus reduce the efficiency of the convective energy transport beneath the solar surface. Due to this reduction in incoming energy, the temperature decays to about 3500 K and the apparent brightness is lower in comparison with the surrounding photosphere, which makes sunspots appear dark. To understand the formation of such magnetic features it is necessary to study the fundamental processes of convection and the emergence of magnetic flux tubes. The general idea behind the formation of sunspots is that a flux tube with a sufficiently strong magnetic field becomes buoyant in the subsurface convection zone and starts to rise up to the surface. At the location and moment it breaks through the surface, the magnetic flux will start to form first pores which already will feature some first decrease in surface brightness [Cheung and Isobe, 2014]. The evolution of sunspots can be summarized in three stages. Some theories (models), which are followed by the author, propose that formation of AR and their conforming sunspots are produced by the emergence or concentrations of magnetic flux tubes (e.g. [Zwaan, 1978], [Cheung and Isobe, 2014]). Within the second part of this work, some results of emergence of explosive mesogranular-sized granules and its relationship with magnetic field observations will be presented. (1) When the formation of the first concentrations of magnetic flux (pores), they begin to join each other leading to the formation and appearance of large magnetic structures (sunspots; see Fig. 2-8). Some authors such as [Hurlburt and Rucklidge, 2000] found from 2-D simulations that sunspots are surrounded by convective cells, which could help to stabilize the created sunspot. (2) Once the sunspot reaches stability, its life-time spans between a few hours up to several days, even several weeks, depending on the amount of magnetic flux, its size (surface area) and morphology. (3) The last stage is the decaying of the sunspot or active region once the magnetic flux and its area begin to shrink. A study made by [Deng et al., 2007] shows that the decaying of sunspots could be caused by three main process, fragmentation of the umbra, flux cancelation of moving magnetic features

(MMFs), and flux transport by MMFs to the outer parts of sunspot.

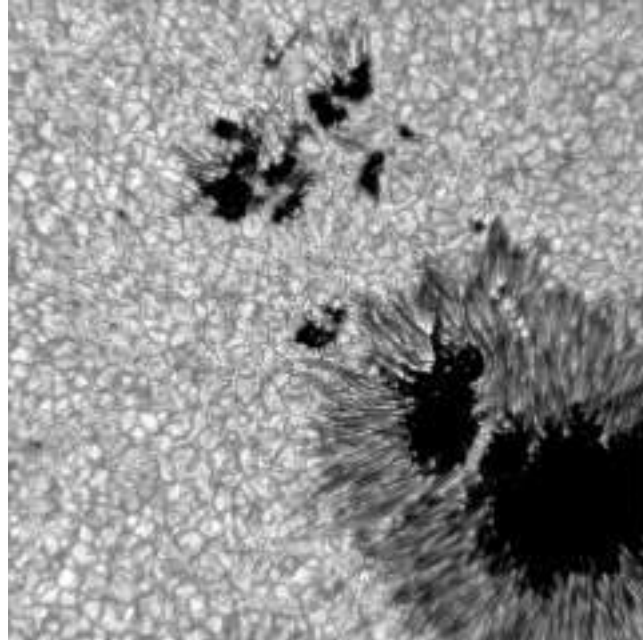


**Figure 2-8.:** High-resolution image taken with the New Solar Telescope (NST) using the TiO (7057 Å, 10-Å bandpass) filter with a field of view of 70 arcsec with a pixel sampling of 0.034 arcsec/pixel. In this example we can see a complex structured penumbra, bright points in the intergranular regions, and granules in high resolution. Date: 2010-09-27 17:25:39. Courtesy of NJIT/Big Bear Solar Observatory.

## Sunspot structure

Sunspots are structured in two main parts, a dark inner core with strong mostly vertical (normal to the surface) magnetic fields (the umbra) and a brighter, filamentary region around the dark part showing weaker magnetic fields which start to be more and more inclined farther away from the umbra (the penumbra).

### Umbra

The umbra is the central dark region of a sunspot. It is cooler than the surroundings, with temperatures in the range ( $\sim 3500 - 5000$  K). These temperature values are due to the presence of strong energy transport inhibition caused by the magnetic fields; the relative velocity of the plasma within the umbra decreases and therefore convective plasma movements are significantly reduced beneath these regions [Biermann, 1941].

Big sunspots, with larger umbral regions show strong magnetic field intensities, which can range between 2000 – 3700 Gauss [Solanki, 2003].

High-resolution observations revealed that even the umbral region inside sunspots is not totally dark but that indeed a large number of fine bright features populate it, among them, the so-called umbral dots.

### Penumbra

The penumbra is the outer ring-shaped region surrounding the umbra, which is not featured by all sunspots<sup>1</sup>. It shows a radial filamentary structure alternating bright and dark areas, being less dark than the umbra but still darker than the photospheric environment (see reviews by [del Toro Iniesta, 2001]; [Solanki, 2003]). It carries a large part of the total sunspot magnetic flux ([Schmidt, 1991]; [Thomas and Weiss, 1992]). Figure (2-8) displays a high-resolution image from the ground-based New Solar Telescope (NST) situated at Big Bear Solar Observatory (BBSO) in the United States. In this figure one can clearly observe the complex structure of the penumbra.

Nowadays it is generally accepted that the magnetic field inclination in sunspots (e.g. [Thomas, 2010]) is split in at least two different inclination domains. While it is nearly vertical in the core of the umbra, it can become almost horizontal in the penumbral region (see Fig. (2-9)).

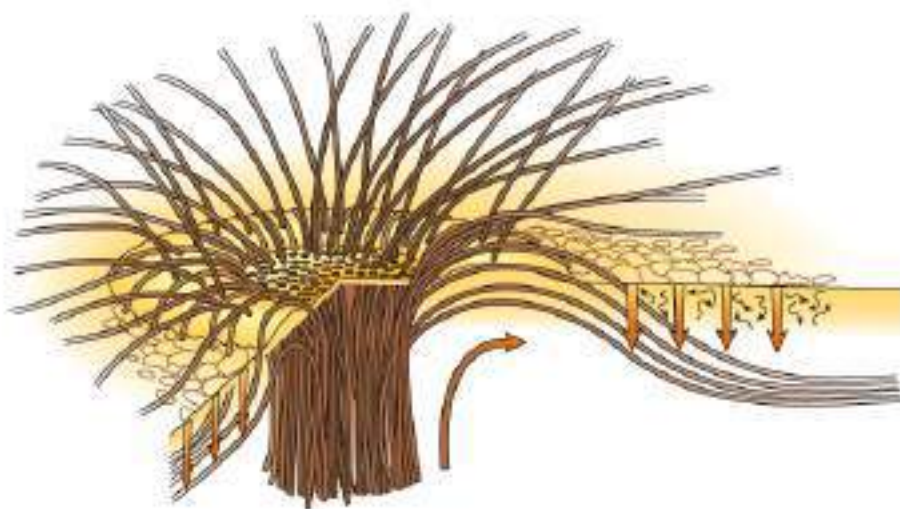


**Figure 2-9.:** Artistic visualization of the magnetic structure in a sunspot as figured out from observations and simulations [Thomas, 2010]. The sketch represents the different inclinations and configuration of the magnetic flux lines inside the umbra and penumbra.

---

<sup>1</sup>Actually, not only sunspots might exist without presence of penumbra, but also the opposite can occur – penumbrae without a hosting sunspot; these features are typically called orphan penumbrae (see, e.g., [Jurčák, 2014]).

## **Part II.**

# **Computational Tools, Algorithms, and the Investigation of Photospheric Proper Motions**

### 3. Python for Solar Physics



**Figure 3-1.:** Python Logo

Python is a “multi-paradigm programming language”, meaning that the programmer has different options on how to implement an algorithm as computer code. One can choose between object-oriented or classical structured programming with both ways entirely supported by Python. Besides these two main paradigms, the user may use additional functional programming paradigms via extension packages. Python is ideal to develop codes and applications quickly and easily in many scientific and technical areas and for most of the computing platforms.

Python is therefore a programming language which offers via its packages a suitable solution to nearly every problem a user might be confronted with. All these together constitute a computing environment. As the aim of the current work is mainly focused on data analysis and scientific computing using a Graphical User Interface (GUI), and particularly for astronomical data analysis, the following packages are used:

- Scipy: Scientific computing in Python[Jones et al., 01 ].

- Numpy: Tools for N-dimensional arrays, integration tools, and linear algebra [van der Walt et al., 2011].
- Pandas: Library for easy use of database structures and data analysis.
- Matplotlib: Library for 2-D visualization[Hunter, 2007].
- Astropy: The Astropy project to develop libraries for astronomy [Astropy Collaboration, 2013].
- PyQt: Python bindings for Qt application framework [Mark Summerfield, 2007].

## 3.1. SunPy

Sunpy is a Python library for developing routines as an open-source alternative to SolarSoftware (SSW), which is mounted on the Interactive Data Language (IDL) platform.

Sunpy has been designed to read, identify, and work efficiently with three of the basic solar physics data: images, time series, and spectra. These functionalities are divided in three Sunpy classes: Map (for images), Lightcurve ( for 1-D time series), spectra and spectrograms ( for 1D and 2D spectra). All basic types of data structures are supported by Sunpy to facilitate easy handling and displaying of the data [SunPy Community et al., 2015].

### Map

Map class lets us easily handle and access 2D image data, apply different operations, e.g., such as rotation, resampling and display functions (see Fig. 3-2) on these data. Map class has also an interface to load data from different sources, including FITS files. The latest version of Sunpy is able to open specific files for the following instruments: Yohkoh / Solar X-ray Telescope (SXT), Solar and Heliospheric Observatory (SOHO)/ Extreme-ultraviolet Imaging Telescope (EIT) and Large Angle Spectroscopic COronagraph (LASCO), Reuven Ramaty High Energy Solar Spectroscopic Imager (RHESSI), Solar TERrestrial RElations Observatory (STEREO) / Extreme Ultraviolet Imager (EUVI) and CORonograph 1/2 (COR), Hinode / X-Ray Telescope (XRT), Hinode / Solar Optical Telescope (SOT), PProjects for On Board Autonomy 2 (PROBA2) / Sun Watcher Active Pixel (SWAP), SDO/AIA and Helioseismic Magnetic Imager (HMI), and Interface Region Imaging Spectrograph (IRIS) slit-jaw imager (SJI) structures.

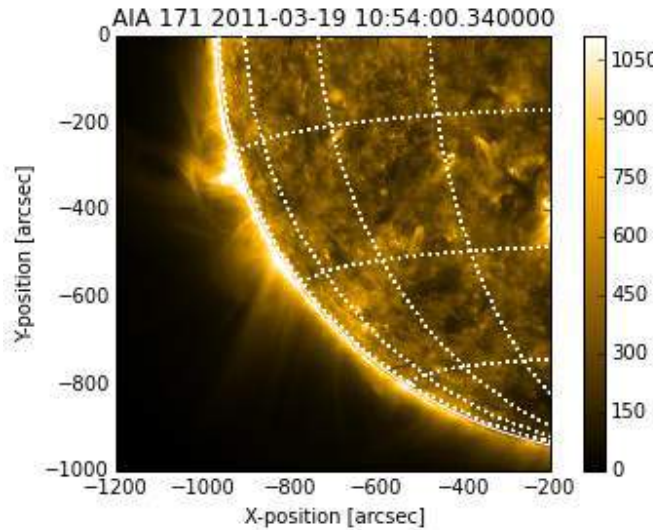


**Figure 3-2.:** Sample map created from SDO/AIA 171Å data created by the GenericMap routine in Sunpy. The basic plot functions show the axis in HelioProjective Coordinates (HPC) from the World Coordinate System (WCS), which are implemented very well into Sunpy libraries.

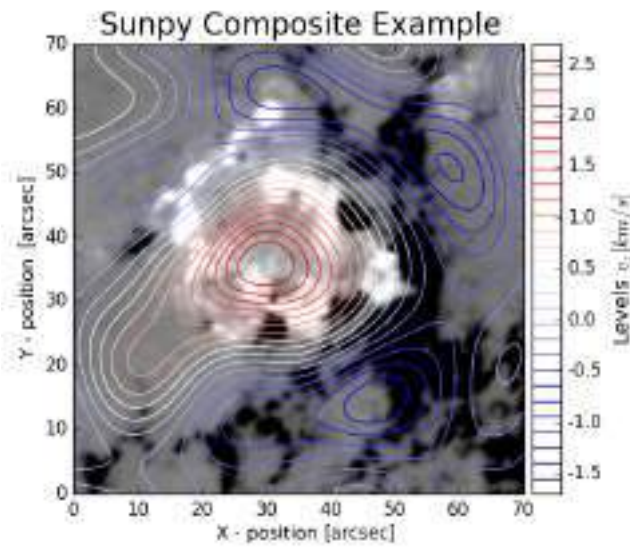


**Figure 3-3.:** Example of a composition image between a line-of-sight magnetogram from HMI/SDO (background) and an up- and downflows velocity map obtained using a Local Correlation Tracking algorithm. The color-coded bar displays the contours with different vertical velocities.

In addition, the Map class can compose images with the CompositeMap class (see Fig.3-3), which includes methods for overlaying images spatially aligned with displaying support and overplotted contour lines. Additionally the Map class features the MapCube tool (see Fig.3-4), which supports the creation of an animation of a time series of maps.

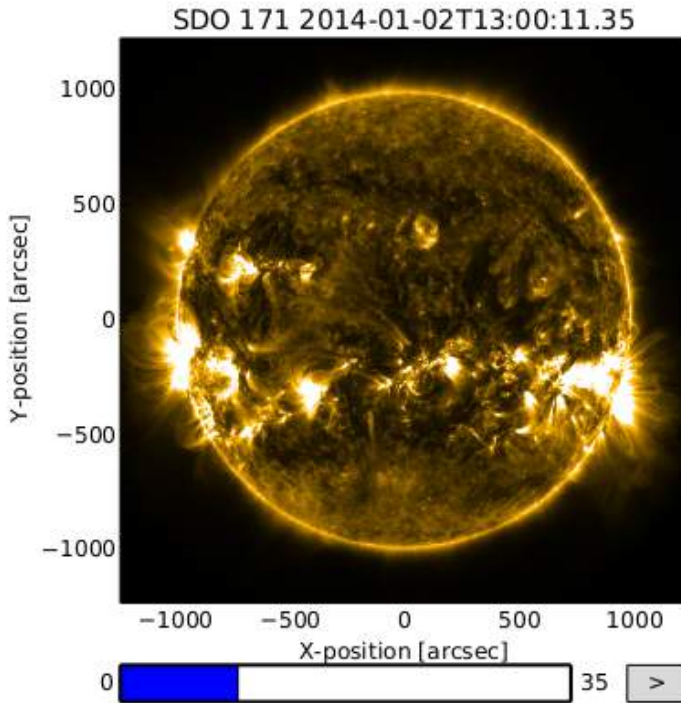


**Figure 3-4.:** The figure shows the matplotlib environment to manipulate data cubes. The bar below is a slider element, so one can select images for different time steps within the data set. MapCube routine helps to create a “data cube” from a file list.

## LightCurves

Analysis of single images or full time series of images are an essential part of solar physics research. Sunpy provides a class called LightCurve, which features a consistent interface for data manipulation as well as displaying of solar time series (see Fig.3-5). The machinery behind LightCurves is based on the Pandas library for data analysis and time series. Currently, the lightcurve class supports data sources for the following missions: the X-ray sensor GOES (XRS), PROBA2/LYRA, and SDO/EVE<sup>1</sup>. For each of these instruments a dedicated subclass (e. g., GOESLightCurve) is available; These subclasses inherit all the LightCurve properties, but own special functions for each instrument.

---

<sup>1</sup>Geostationary Operational Environmental Satellite system (GOES) and its X-rays Sensor (XRS); PROBA2 / Large Yield Radiometer (LYRA); SDO/Extreme UltraViolet Variability Experiment (EVE).

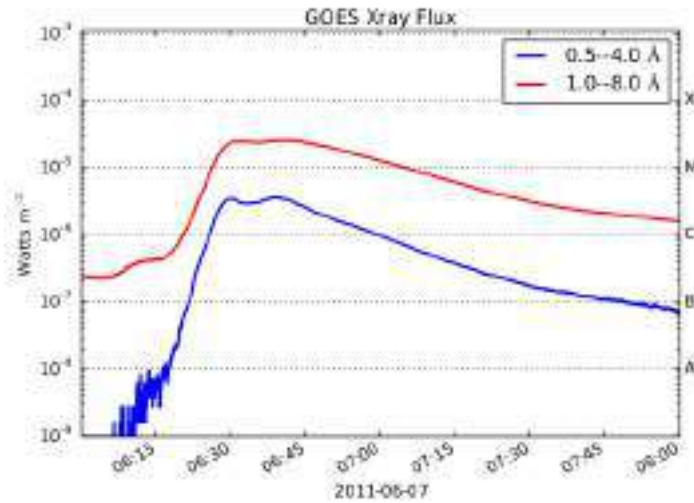


**Figure 3-5.:** LightCurve example displaying a GOES (XRS) curve during a solar event. The blue and the red lines give the evolution of the X-ray flux in two different spectral bands.

## Spectra

One of the objectives of Sunpy data handling, is to provide support to access such data obtained from various instruments and telescopes. Spectra module, includes Spectrum and Spectrogram class, which support 1-D and 2-D data structures (see Fig.3-6). As previously mentioned (Section 3.1), the Spectrogram class has been constructed in such a way that for each instrument a subclass, containing specific functions for each instrument, is available. Common functionalities in the Spectrogram class include functions such as the union of different time ranges and frequencies, background subtraction functions and displaying functions. At this time, the Spectrogram class supports network data radio telescope e-Callisto and spectrograms STEREO/SWAVES<sup>2</sup>.

---

<sup>2</sup>Solar TERrestrial RElations Observatory (STEREO) and S/WAVES is an interplanetary radio burst tracker

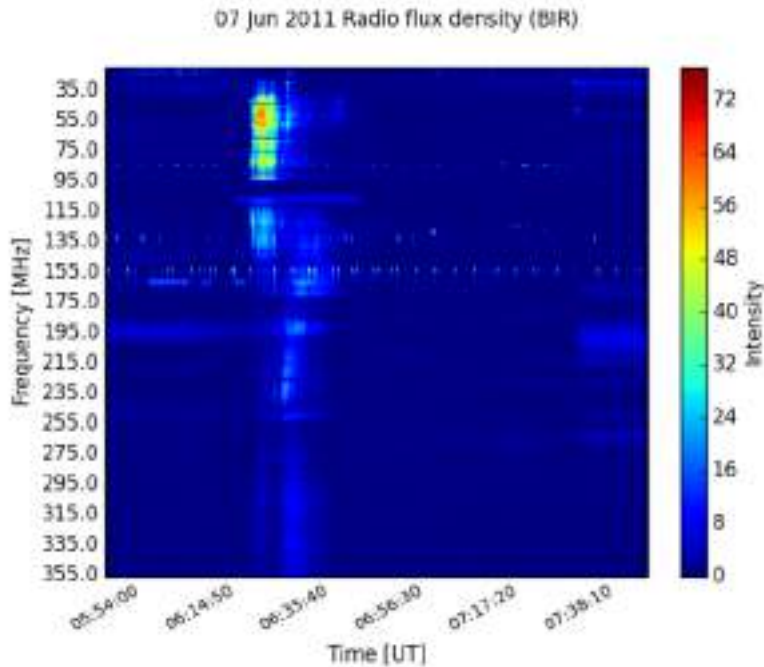


**Figure 3-6.:** Example of the spectral image using *Spectra* functions in Sunpy. Data was obtained from Callisto Spectrometer Radio array.

## 3.2. Algorithms and Computational Tools

In the present work the author created and implemented different scripts to facilitate the analysis and the study of proper motions in the solar photosphere. Data processing took in general three stages before the Local Correlation Tracking (LCT) technique was eventually applied to the final data cube.

### Rotation

Due to the changing orientation and alignment of SDO/HMI with respect to the Sun, the images obtained from HMI need to be oriented for rotational and translational compensation. The image header includes the keyword “CROTA2”, which gives the precise value of the HMI turning angle with respect to the solar north pole at the moment the filtergram was taken. The maps have been rotated using the `rotate` and `interpolation` function from `scipy.ndimage` library. The `rotate` function uses spline interpolation to calculate the rotation and the new array (map). Figure 3-7 shows an example of an image rotated using this procedure.

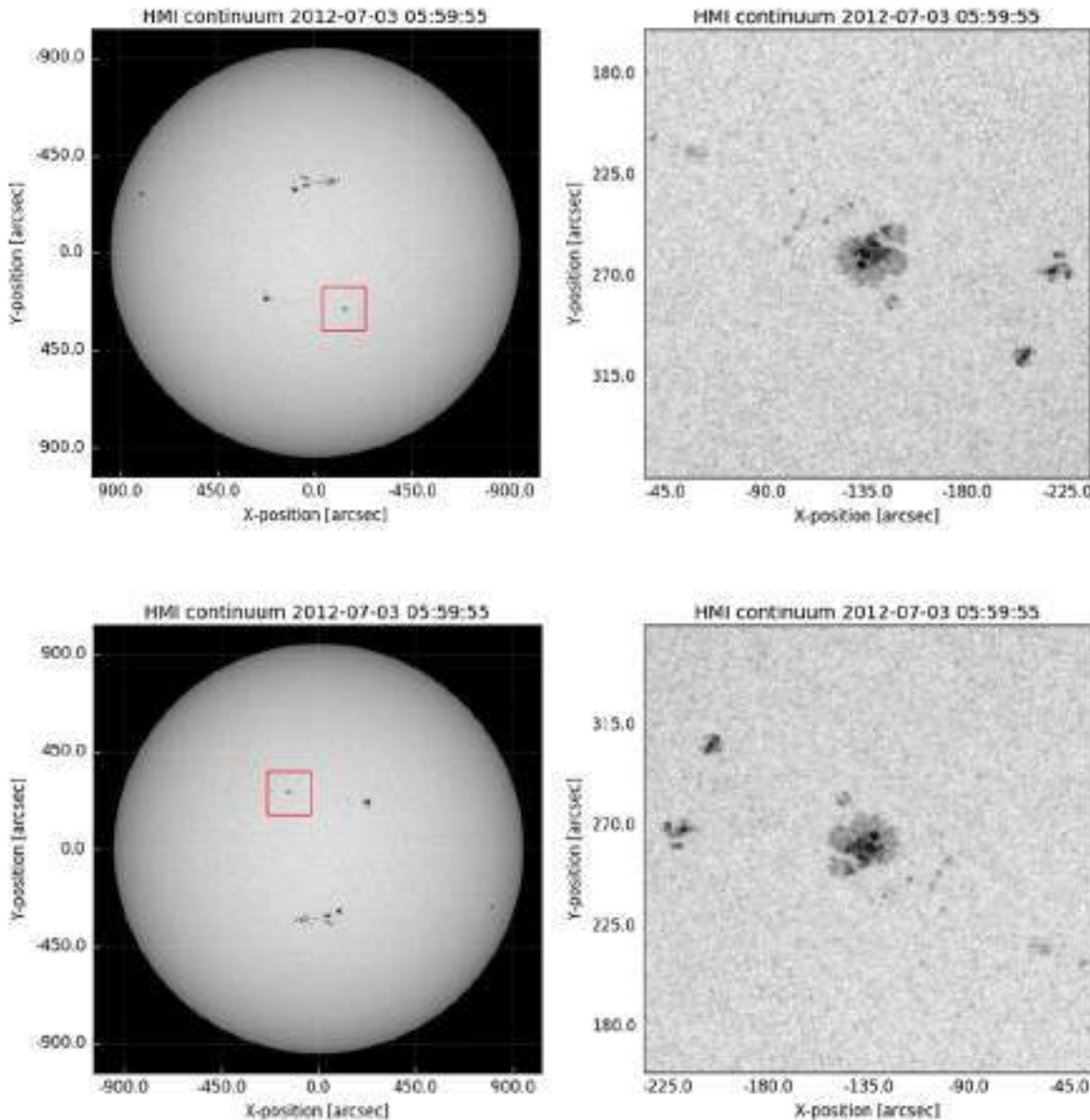


**Figure 3-7.:** The plot illustrates an example of the resulting image after application of the `rotate` function.  
All HMI filtergrams must be rotated to obtain co-aligned and correct image data series.

## Alignment

As previously stated, the Sun does not rotate like a rigid body. The Sun rotates differentially, i. e. for different latitudes the rotational velocity changes (see Fig. 3-8). Considering that we want to calculate the plasma motions properly within active regions, i.e. a fraction of the full solar disk coverage, it is necessary to align the images bearing in mind the differential rotation by applying the alignment procedure in the active region under analysis. The proper motions to be studied are small-scale movements, in the range of granular sizes.

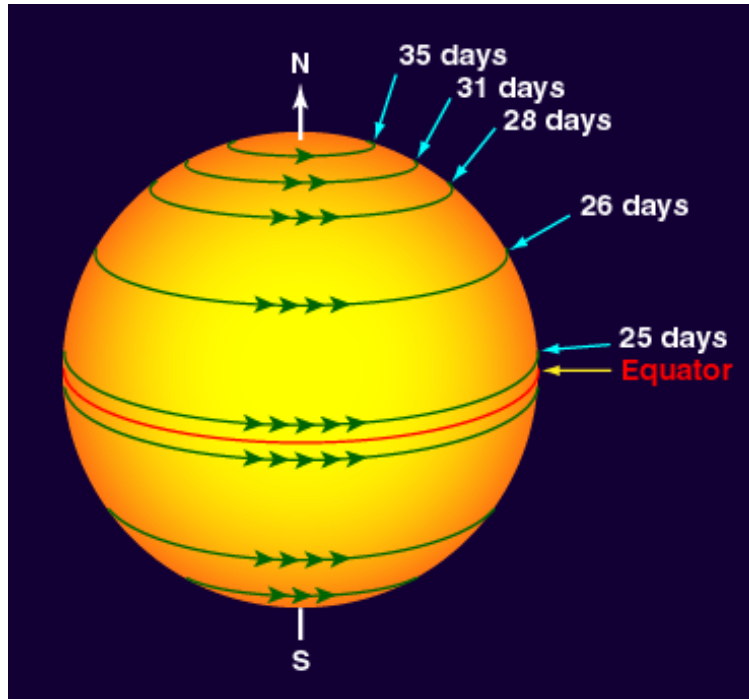


**Figure 3-8.:** Figure representing the solar differential rotation. Each latitude has a different angular velocity being higher on the equator than on the poles of the Sun. Taken from: <http://www.star.bris.ac.uk/bjm/solar/solarrot.html>

The differential rotation velocity is higher than these motions and therefore it is necessary to align the images to a specific reference point. The alignment algorithm applies the Sunpy function `diff_rot`. This function calculates the change in longitude for a particular time on a given latitude. In our case we applied the so-called Howard rotation, which uses values for small-scale magnetic features [Howard et al., 1990].

### Subsonic filtering

Subsonic filtering is the last stage in the pre-treatment before applying LCT. It is used to eliminate high frequency oscillations, associated to the natural frequency of p-mode oscillations of 5 minutes and residual “vibrations” from previously aligned data. Subsonic filtering is applied in the frequency domain [Title et al., 1986]. The algorithm uses a phase-velocity threshold of  $4 \text{ km s}^{-1}$ . An apodization in the temporal dimension (roughly 5% of the total length of the time series at both ends of the data cube) was applied to minimize the boundary effects in the filtering process. The final product is composed by steady evolutionary movies, day by day in each time series, where each full day consist of 1920 images with a FOV of  $250'' \times 150''$  and a cadence of 45 seconds.

After the pre-treatment previously explained, the observations are properly calibrated to

calculate the motions of the plasma in the selected region of interest (ROI).

## Velocity Field Maps

On the surface of the Sun, LCT has been applied in several observational studies on sunspots and for granular tracking to measure solar rotation rates. The LCT method was applied for the first time by [November and Simon, 1988] for determining velocity fields for the solar granulation. Nowadays, LCT techniques are used to calculate at many different spatial and temporal scales the flow fields, for instance, to study the solar dynamics, such as flows within super granular cells (see Fig. 3-9). The algorithm is based on a basic but powerful idea of “maximizing and finding the best local congruence between two images”. We define a proper motion as the most appropriately displacement, which maximizes the spatially localized cross-correlation between two consecutive images with a temporal separation  $\tau$ . It should be small relative to the lifetime of the tracked structure. The two-dimensional cross-correlation function is defined for each location in the data set multiplying the product of intensities by an apodization window  $W(\mathbf{x})$ .

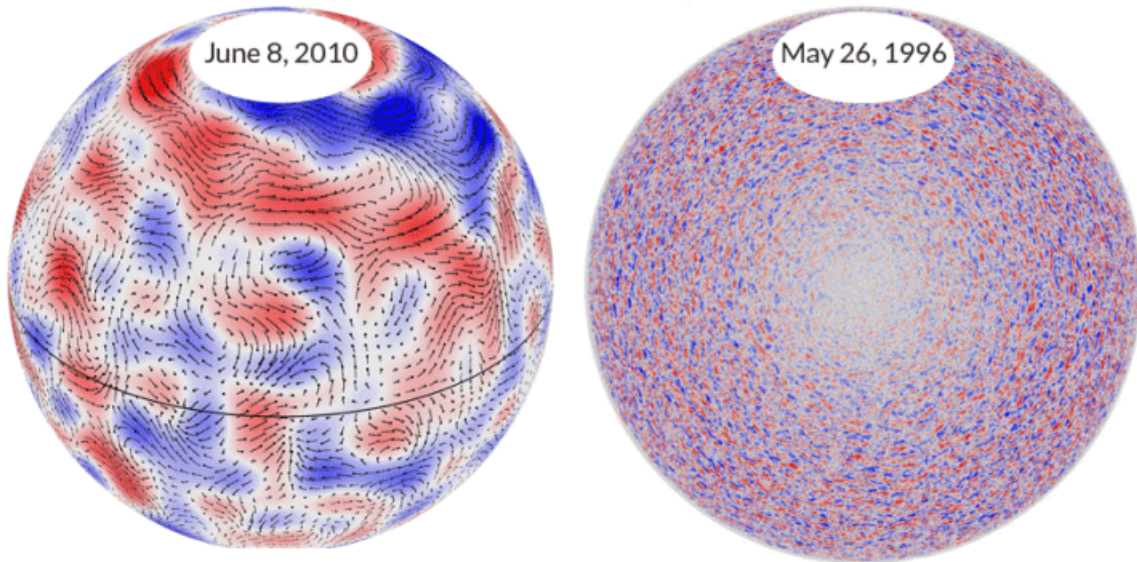


**Figure 3-9.**: Images showing the long-term evolution of giant convective cells moving plasma on the solar surface [Hathaway et al., 2013]. Image taken from: <https://wattsupwiththat.com/2013/12/05/giant-convection-cells-found-on-the-sun/>. (Last accessed: November 3, 2016).

According with [November and Simon, 1988], the spatially localized cross correlation  $C(\delta, \mathbf{x})$  is a 4-dimensional function: two dimensions are formed by the displacement vector  $\delta$  and two dimensions are given by the central position of the window function  $\mathbf{x}$ . The cross correlation

function  $C(\delta, \mathbf{x})$  is defined in terms of the image intensity  $J_t(\mathbf{x})$  and  $J_{t+\tau}(\mathbf{x})$ , which are two consecutive images of the data cube in consecutive time steps  $t$  and  $t+\tau$ , and an apodization function  $W(\mathbf{x})$ :

$$C(\delta, \mathbf{x}) = \int J_t\left(\zeta - \frac{\delta}{2}\right) J_{t+\tau}\left(\zeta + \frac{\delta}{2}\right) W(x - \zeta) d\zeta. \quad (3-1)$$

In our case we used a Gaussian window for the apodization function with a Full-Width at Half-Maximum (FWHM) criterion adapted to sub-areas sizes for the correlation.

### **Shrinking-Sun effect and other systematic errors**

It is well documented that the LCT technique produces in general some systematic errors (e.g. [Roudier, 1999, Potts, 2003]) in the determination of displacements, for instance, those which result in an effective flow converging towards the center of the solar disk. This effect is also known as the Shrinking-Sun [Lisle et al., 2004]. This apparent flow is superimposed on the real solar flows measured by LCT and it can reach values of  $1 \text{ km s}^{-1}$  [Loptien, 2016]. Besides, the LCT-method tends to underestimate the velocity fields. This is due to the nature of the interpolation algorithm for fixing the position of the maximum correlation where a lower pixel accuracy (of the order of  $< 1 \text{ arcsec}$ ) can play an important role in the results.

Tests conducted by the authors of the LCT-code, used in the current study, have shown that in the worst case this underestimation may amount up to 20-30% ([Yi et al., 1992]; [Molowny-Horas, 1994]). For some aims of science, this artifact can be removed by subtracting a temporally averaged LCT map. However, this correction is not enough if the selected solar flows are stationary over time.

Following the idea of [Loptien, 2016], one can see that it is not necessary to apply the shrinking-Sun effect correction. The correction, using a time average over the velocities, is enough to correct the systematic LCT-code errors.

Figure (3-10) shows that the mean value for the distribution of  $v_x$  velocities is 0. The  $b_0$  represents the angle defined as the tilt of the rotational axis toward the observer in HelioGraphic (HG) coordinates in the World Coordinate System (WCS) usually given as Carrington latitude of the observer in the header.

This mean value is zero as the proper motions studied are on granular scales and, on average, the sum of the velocities in  $x$ - and  $y$ -directions are zero for such convective cells. Figure (3-11) shows the magnitud map ( $v = \sqrt{v_x^2 + v_y^2}$ ). According to theory, a magnitude distribution created via two Gaussian components  $v_x/v_y$ , which have equal variance and mean  $\sim 0.78 \pm 0.51 \text{ km s}^{-1}$  values, will form a Rayleigh distribution.

The Rayleigh distribution is given by

$$f(v; \sigma_*) = \frac{v}{\sigma_*^2} \exp^{-v^2/(2\sigma_*^2)}, v > 0 \quad (3-2)$$

where  $\sigma_*$  is the scalar parameter of the distribution [Papoulis and Pillai, 2002]. The *mean* ( $\mu$ ) and the *standard deviation* ( $\sigma$ ) in terms of the *scalar factor* ( $\sigma_*$ ) are:

$$\mu = \sigma_* \sqrt{\frac{\pi}{2}}, \quad \sigma = \sqrt{\frac{4 - \pi}{2}} \sigma_*. \quad (3-3)$$

To find the scalar factor  $\sigma_*$  using the velocities obtained from the LCT algorithm, we employed the *least-squares* method included in the package of Scipy `scipy.optimize`. This function solves a nonlinear least-squares problem where `least_squares` finds a local minimum of the cost function<sup>3</sup>.  $F(x)$ :

$$F(x) = \frac{1}{2} \cdot \sum_0^{m-1} \rho(f_i(x)^2) \quad (3-4)$$

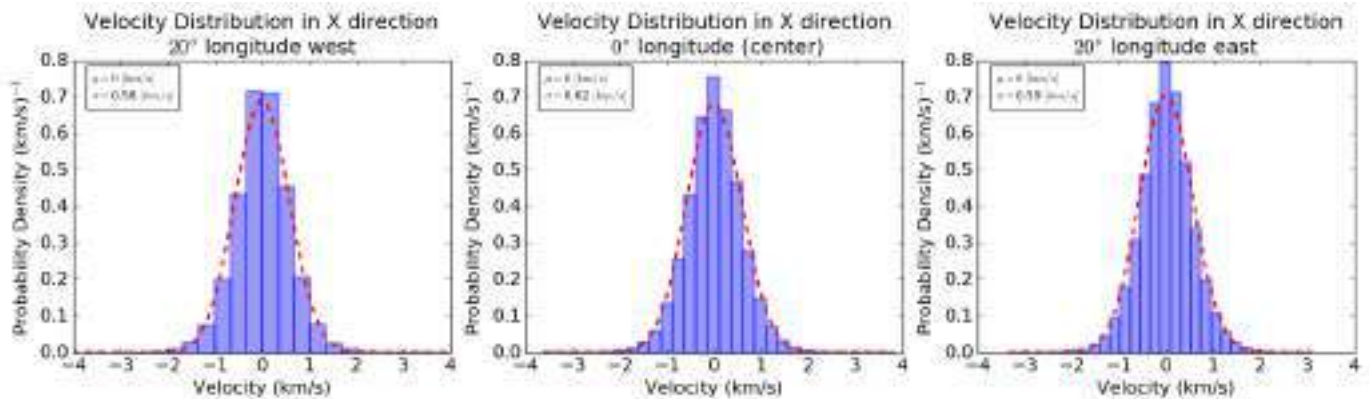


**Figure 3-10.**: Figure shows the velocity flow maps distribution in x-direction for longitudes  $-20^\circ$ ,  $0^\circ$  and  $+20^\circ$ . The normalization statistics result with an expected mean value of  $\sim 0 \text{ km s}^{-1}$  and a standard deviation of  $\pm 0.51 \text{ km s}^{-1}$ .

<sup>3</sup>For more information visit the web-page [http://docs.scipy.org/doc/scipy/reference/generated/scipy.optimize.least\\_squares.html](http://docs.scipy.org/doc/scipy/reference/generated/scipy.optimize.least_squares.html)

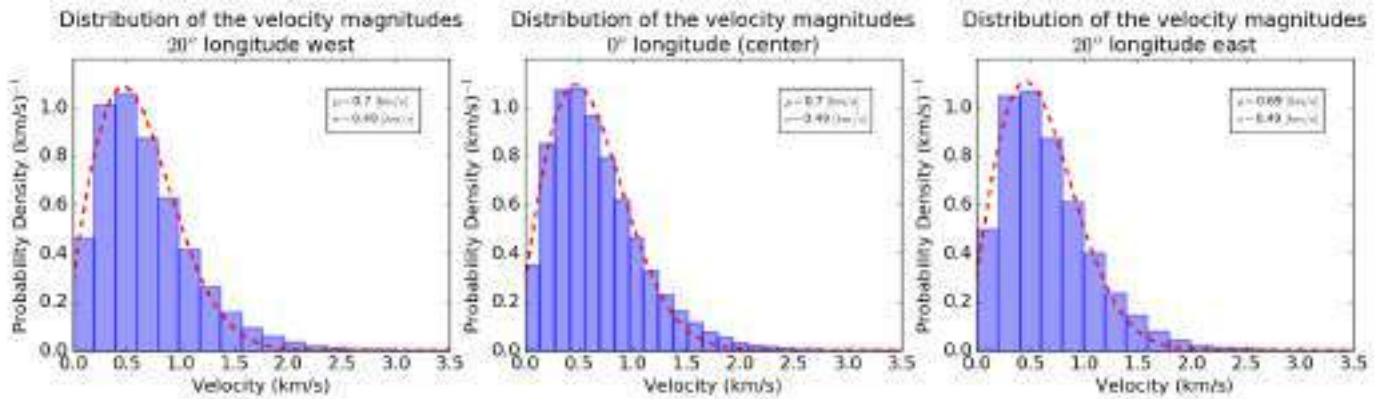


**Figure 3-11.**: Same as in Fig. (3-10), but for the velocity  $v = \sqrt{v_x^2 + v_y^2}$ . The figure shows a velocity magnitude of  $\sim 0.7 \pm 0.49 \text{ km s}^{-1}$ .

### 3.3. GUI for LCT Analysis

A Graphical User Interface (GUI) has been developed in this work to help other users to carry out an interactive process for the analysis of flow maps. Furthermore, it enables the user to easily change a few simple parameters as well as permits to modify the displaying and plotting options. This GUI can load data cubes, which should be properly aligned before hand (SunPy provides functions to coalign a list of maps) as well as pre-treated properly<sup>4</sup>. In general, the input should be a data cube stored in the Flexible Image Transport System (FITS) file specifications or IDL native data files. The widget incorporates six different tools or workspaces. The main workspace is the so-called *Flows Tools*, which is based on the LCT algorithm. This workspace is divided in two sections (see Fig. 3-12). The first one (red box in the figure) is responsible for setting the four more relevant parameters to compute the velocity maps.

The first parameter is the size of the Gaussian or apodization window (*FWHM*), which depends on the size of the structure aimed to study, i.e, if one wants to study granular-sized features, the value for the *FWHM* should be chosen somewhere between half of their characteristic size up to the full size of the granular features. The second input value is the *Pixel size*, which can be taken from the images header information (typically appears like *cdelti*, where *i* specifies the dimension and thus is 1 or 2 for a normal image). This value is measured in arcsec too. The third parameter is *Cadence*, which is the time passing between two consecutive images taken by the instrument. For each data set the two values (*Pixel size* as well as *Cadence*) are depending on the used instrument/data set itself. The last variable, which can be modified by the user, is the time range for which one wishes to apply the LCT.

<sup>4</sup>As an example in the current work we need to do a pre-filtering using the subsonic method mentioned above

The importance of this parameter comes from the fact that if one is interested in the average dynamics of structures one should temporally average over their corresponding lifetime. For instance, if one has data with a time cadence of 45 seconds, and wishes to study structures with life-times of 5 minutes, one should use 6 images to obtain the average velocity map. The second block of parameters (blue box in Fig. 3-12) contains the parameters necessary for creating the flow velocity vectors. Among them there are the following settings: Number of pixels between vectors, desired colors, width and scale of the vectors as well as an intensity and/or velocity magnitude threshold for the creation of masked images.

The widget also features other tools. With these additional tools the program can generate and visualise statistical appliances, i.e. histograms of intensity as well as velocity distributions for quick comparisons and analysis. One can generate saturated images and overlays to emphasize specific regions. It is possible to obtain contours plots as well as up and downflows maps, save images and explore regions of interest by masking. The GUI has been created using QtDesigner, a tool of Qt company and converted and finished with PyQt [Mark Summerfield, 2007].

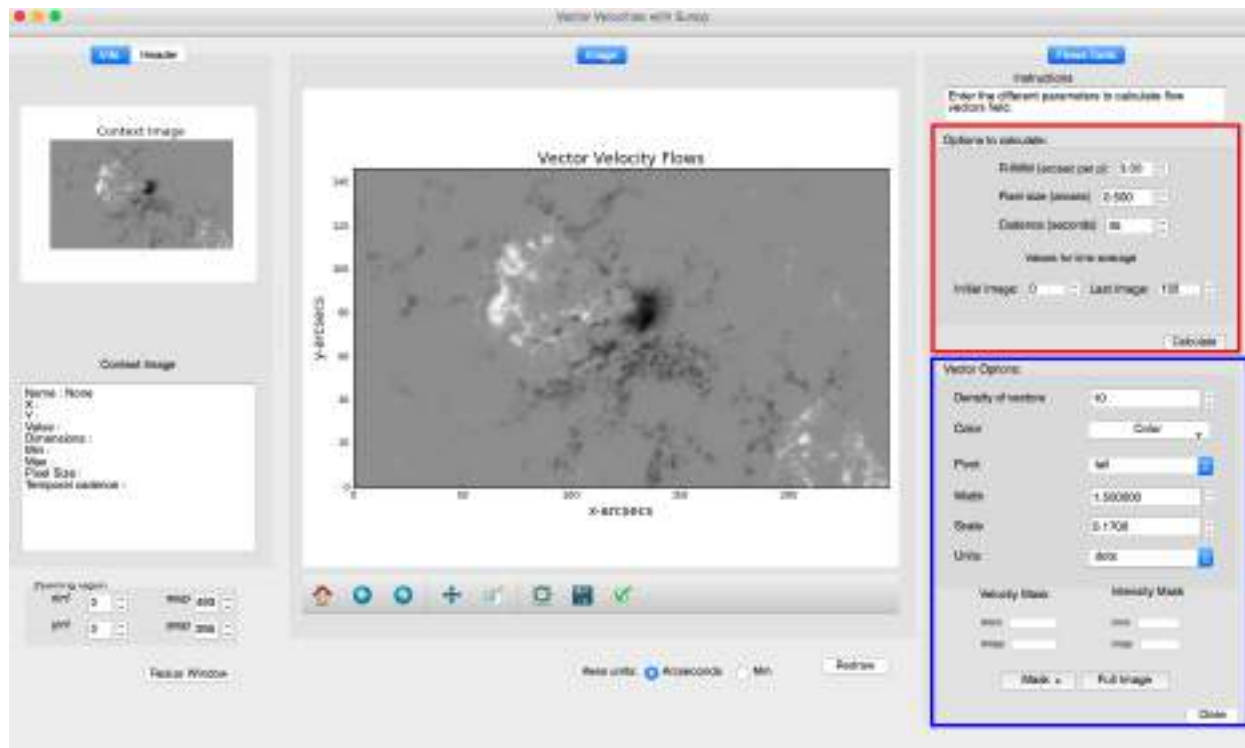


**Figure 3-12.:** Main GUI developed for applying LCT analysis over a time series of filtergrams . Framed in the red box are the most important parameters that can be changed to calculate the flow maps. The blue box frames the variables responsible for the visualization of the flow field.

# **4. Study of Sunspots and Pores by means of Local Correlation Tracking Techniques**

This chapter will focus on the LCT analysis applied over the appropriate data set and the first results showing the evolution of active regions through the proper motion of structures yielding velocity fields that describe the plasma dynamics in the Field-of-View (FOV). Prior to it, there is a description of the observations and the preparation of the data, i.e. alignment, “noise” filtering, and selection of the time series.

## **4.1. Observations**

We obtained four time series of images, each one consisting of five days of observations comprising continuum intensity maps and LOS magnetograms.

The continuum filtergrams are taken in the spectral band of the Fe I absorption line centered at 6173 Å. These data are available in series of 45 seconds or 12 minutes cadence (necessary time to obtain two consecutive images depending on the requirements). The data used in this analysis are continuum filtergrams with a cadence of 45 seconds.

A search was made in a temporal range of four years within the archived SDO data, from 01-Jan-2011 (00:00:00 UT) to 31-Dec-2014 (23:59:59 UT) using the JHelioviewer software [ESA, 2016], which allows one to create movies for each year and check them using their GUI daily images of the Sun.

## **4.2. Data**

As we aim at analyzing sunspots that can be observed during their formation, evolution and decay, we have restricted the search to the spatial range  $\sim (-750, 750)$  S-N and  $\sim (-750, 750)$  W-E as displayed in Fig.4-1. This is due to the Sun being a sphere and hence the problems arising when features of interest come too close to the solar limb (projection effects, limb darkening, among the most prominent ones).

The selected data meet approximately the necessary pre-requisites for the study. These conditions are the full coverage of the three phases of evolution, namely the formation,

stable phase, and decay of an active region, within the time series, while the active region is located all the time on the solar disk and does not rotate reaching the backside of the Sun. Table (4-1) lists some basic information for the selected active regions.

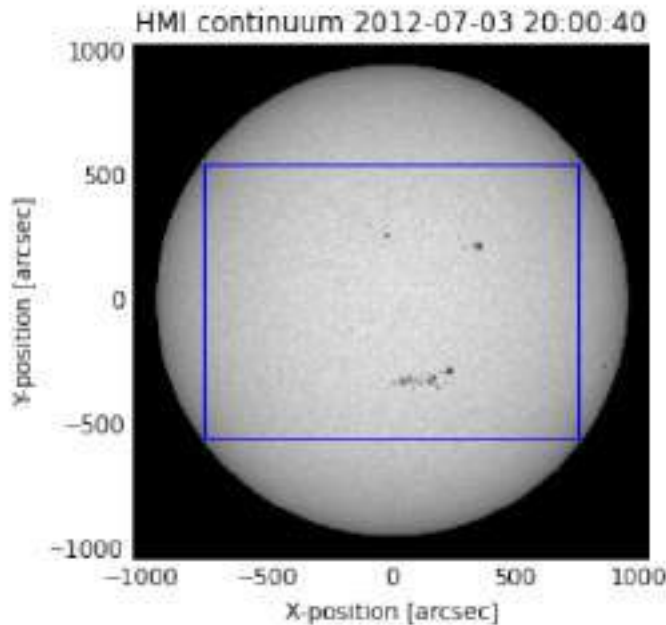


**Figure 4-1.:** Image of the Sun in the continuum taken with the instrument HMI onboard the satellite SDO. The restriction area (blue box) shows the spatial range of the FOV in which we searched and selected active regions and subsequently followed their evolution. This condition is due to the requirement of eliminating flow vector projections on the solar limb.

Data selection	
Time-Range UT	Active Region
From 2011-04-10 23:00:00 to 2011-04-13 18:13:30	1190
From 2012-06-30 10:00:00 to 2012-07-05 23:59:15	1517
From 2013-06-01 02:00:00 to 2013-06-01 18:00:30	1762

**Table 4-1.:** Active regions observed during almost their entire evolution cycle across the solar disk.

## First Results

For the study of proper motions of different structures situated within the solar photosphere, intensity continuum images obtained from the HMI instrument onboard the SDO spacecraft were employed. These motions were analyzed using a LCT algorithm implemented by [Molowny-Horas, 1994; Yi et al., 1992]. For this particular study, the Gaussian tracking window size was adjusted to the size of the structures to be tracked. We will show first results applying this algorithm to the AR 1517 during its stable stage. Besides that, when tracking granular-sized structures, the used window size is 1.5 arcsec, corresponding to the typical granular size [Keenan, 1938]. The LCT algorithm returns two horizontal displacement maps, corresponding to the velocity components  $v_x$  and  $v_y$ , and a vertical velocity component,  $v_z$ . All of these values were obtained according to Eq. (3-1). In a next step, before applying the analysis systematically to various active regions, we tested the LCT algorithm with different temporal averaging time spans, namely: temporal averages of 3.75, 7.5, and 15.0 minutes corresponding to 5, 10 and 20 image intervals, respectively. For the following results, the flow maps were calculated using temporal averages of 5 images.

Figure (4-3) *bottom* illustrates the velocity field map calculated via a Gaussian window with  $FWHM = 1.5$  arcsec and averaged over a time of 3.75 minutes (5 images with cadence of 45 seconds). Exploding granular structures can be identified in the velocity field and correspond to flow divergences. In some areas of the FOV penumbral outflows so-called moat flows are observed, which will be described in Chapter 5. Structures formed within the velocity divergence region indicate that plasma is moving towards intergranular lanes where it starts to sink back into the Sun's interior. Divergent velocities are related to the expansion and fracture of mesogranular-sized granules ([Rast, 1995]; [Roudier et al., 2003]; [Roudier and Muller, 2004]; [Palacios, 2012]). The white line in Fig. (4-3) *bottom* traces the magnetic neutral line which is deducted from SDO/HMI magnetogram (see Fig. (4-3) *top*). Clipping the magnetograms in a narrow positive/negative range of, e.g.,  $\pm 100$  G, yields a clearly visible boundary between the positive and negative polarity of the magnetic fields, which we refer to henceforth as the neutral line and depict with a solid white line in the magnetograms. We calculated the angle, formed by the components  $v_x$  and  $v_y$  as  $\tan^{-1}(v_y/v_x)$ , and compared it with the magnitude of the velocity in a 2-D histogram, as shown in Fig. (4-6), proving that there is a preferential flow direction. The strongest displacements are towards the southward direction, specially within the range of  $\sim [225^\circ - 315^\circ]$ . In section 4.7 it will be evident for the reader that the plasma is expanding and pushing out the surrounding material to the right side. There are some smaller displacements to the left-upwards side in the pathway of the evolving spot following the same direction.

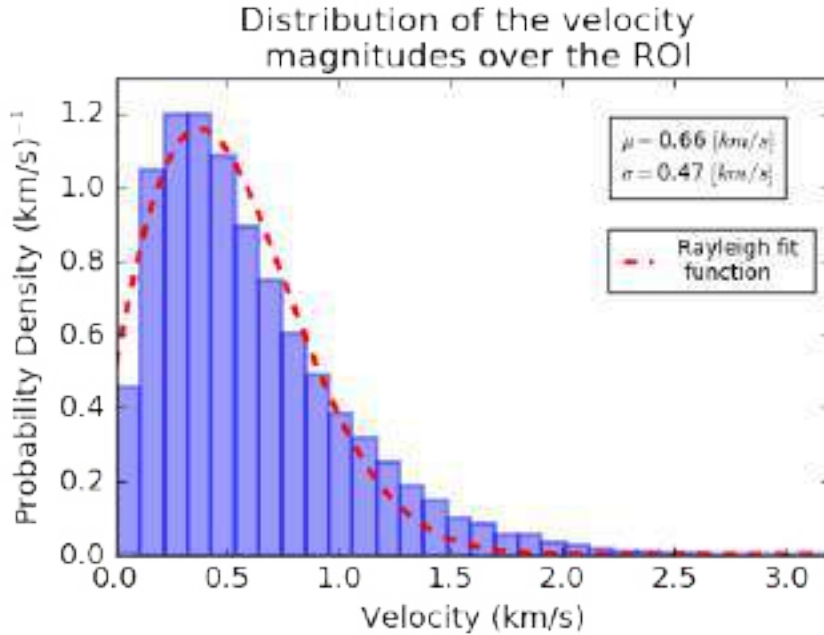


**Figure 4-2.:** Histogram of the calculated velocity magnitudes of the FOV given in Fig. (4-3). The red line shows the fitted Rayleigh distribution through the probability distribution.

It is possible to observe perpendicular fields to the neutral line in the regions where the white line is crossing. Figure (4-3) shows three sunspots, with the presence of tiny pores. In a following step we focus on the velocity magnitudes in the FOV. Figure 4-2 displays the velocity magnitude  $\sqrt{v_x^2 + v_y^2}$  and a Rayleigh Probability Distribution Function in the FOV given in Fig. (4-3) fitted through the histogram in a dashed red line. The resulting mean velocity from the fit has a value of  $0.66 \pm 0.47 \text{ km s}^{-1}$ . For this figure we have used: the whole FOV/only the non sunspot regions/only the sunspot regions.

Figure (4-4) shows the velocity field masking the sunspots regions. In this case, the fit values of the velocity distribution for the plasma outside the sunspot is given by  $0.69 \pm 0.49 \text{ km s}^{-1}$ . Thus we can conclude that there is no strong presence of magnetic fields between the spots like plages or magnetized-granulation. The presence of magnetic fields can hamper the plasma velocity, as evidenced when displaying velocities inside the sunspot in Fig. (4-3, bottom).

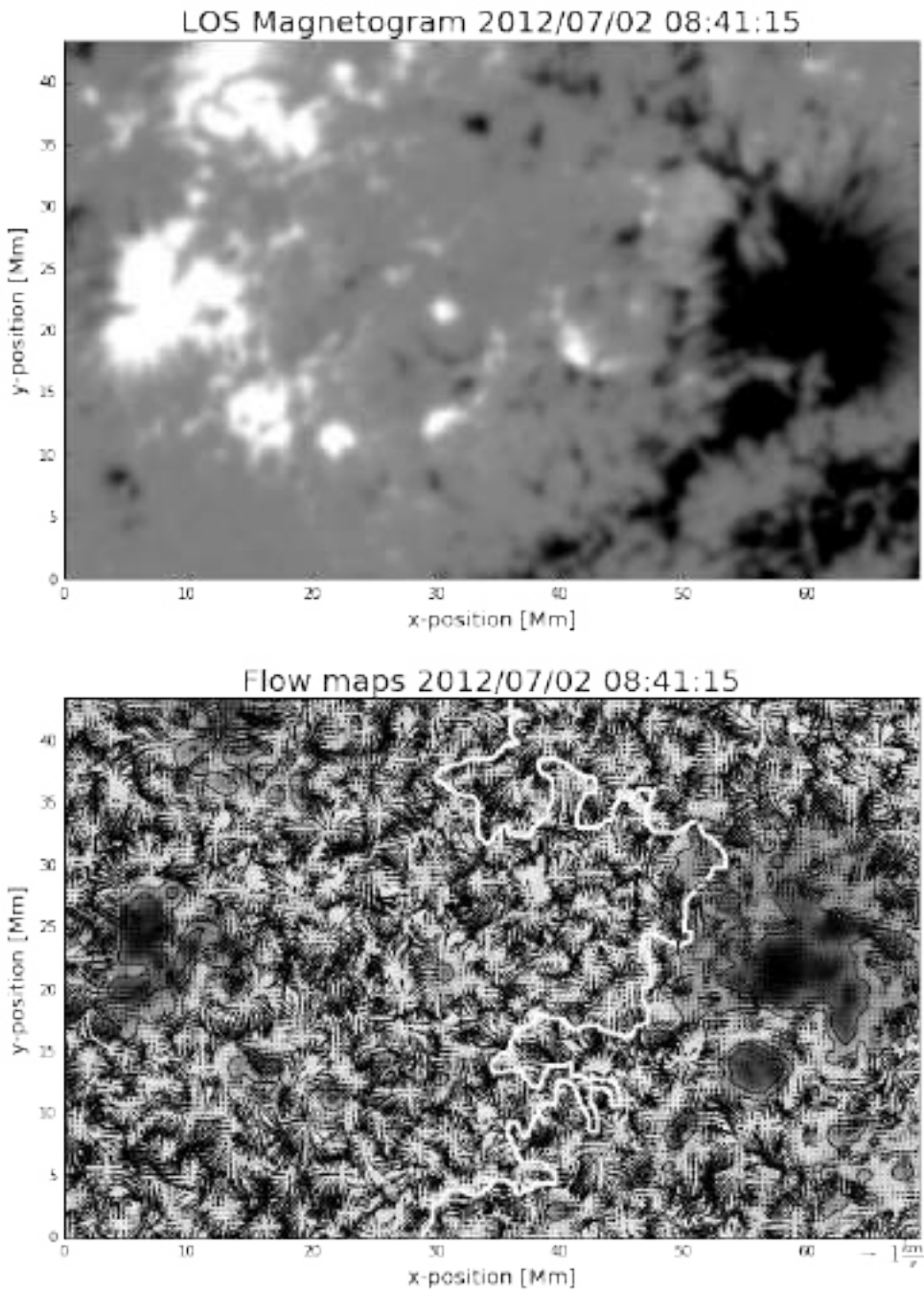


**Figure 4-3.:** [Top]: Magnetogram corresponding to the region under study. [Bottom]: Flow map of horizontal velocities in the FOV, resulting from applying a FWHM of 1.5 arcsec; the chosen region is centered on (long=  $-20.03^\circ$ , lat=  $18.36^\circ$ ) in Heliographic Coordinates (HGC). The white line show the neutral line, obtained from the magnetogram on top, and the black lines represent the boundaries of the umbral and penumbral regions.

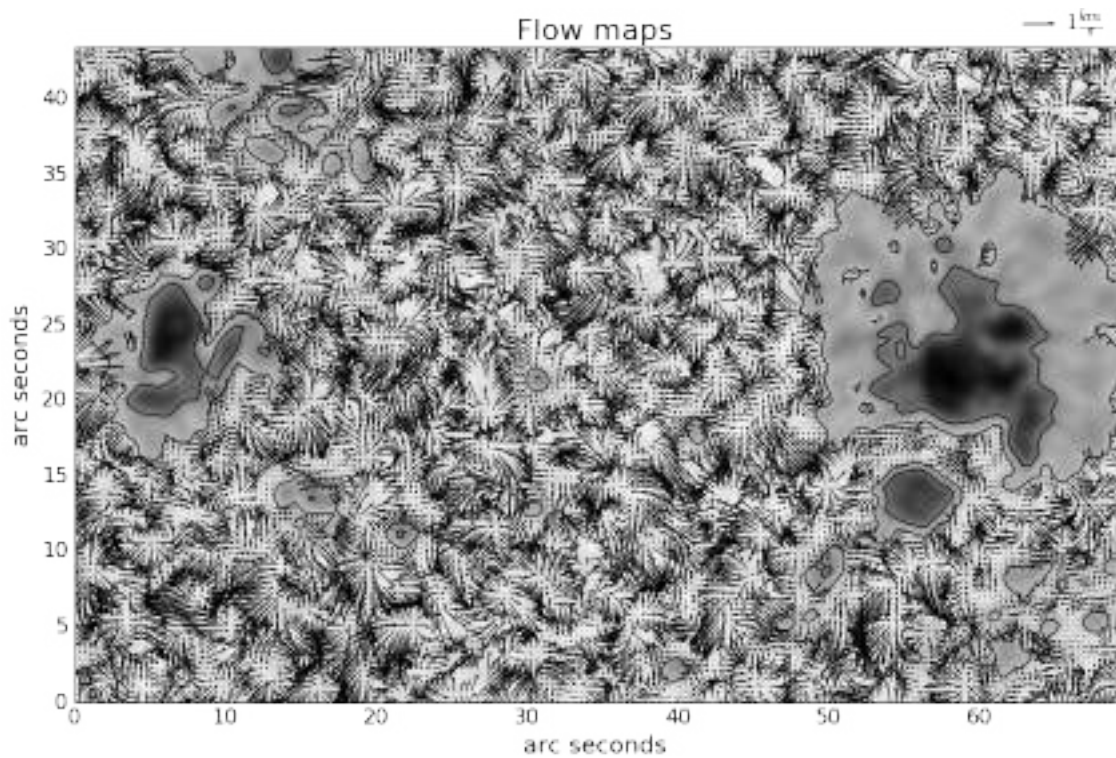


**Figure 4-4.:** Flow map showing the velocity field outside the sunspots and pores. The contours have been obtained using differences of intensities to separate the umbra, penumbra and granular regions.

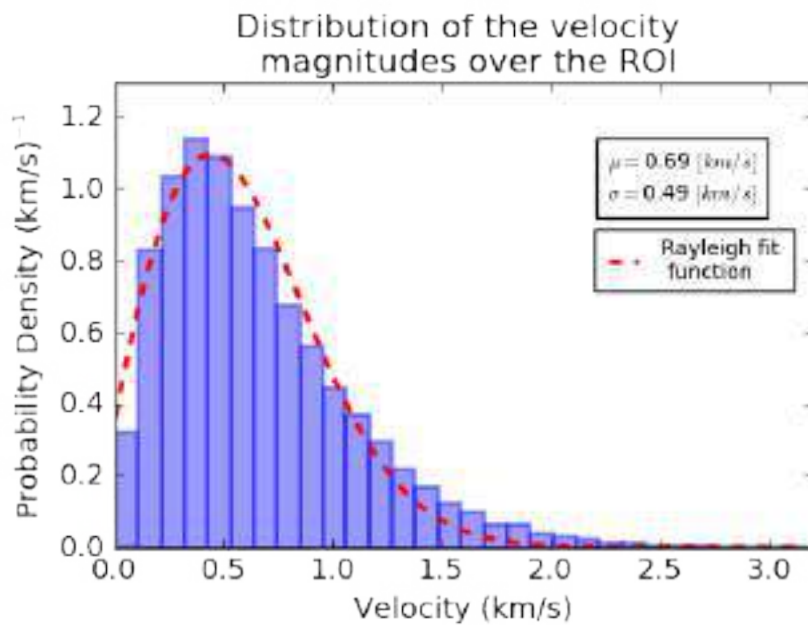


**Figure 4-5.:** Similar to Fig. (4-2) but only for selected sunspot and pore regions.

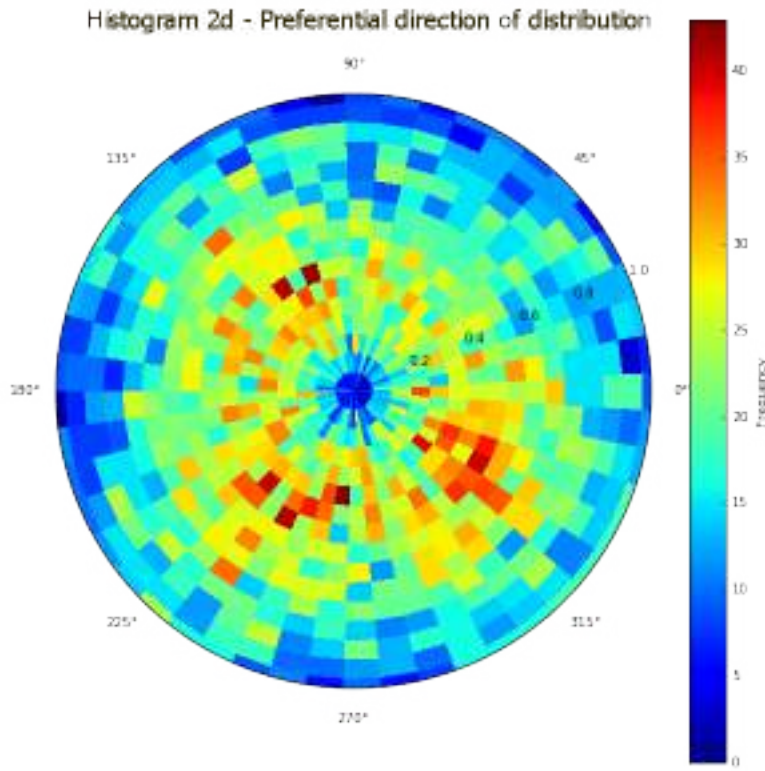


**Figure 4-6.**: 2-D histogram giving the angle as well as the magnitude of the measured velocities. The color code gives the number (frequency) of the measurements.

### 4.3. Emergence of Magnetic Fields in Exploding Granules

The evolution of the photospheric granulation is dominated by the expansion and fragmentation of granules. Mesogranules were discovered by [November, 1981] from dopplergrams and were confirmed using horizontal granular flows observed by the Solar Optical Universal Polarimeter (SOUP). Observations revealed that the distribution of fragmenting granules is responsible for the set on and creation of the mesogranular structures [Oda, 1984]. Moreover, it is known that exploding granules can occur with certain preferences within divergent flows inside such regions [Title et al., 1989]. This suggests that mesogranular-sized granules somehow trigger the expansion and explosion ([Simon et al., 1991]; [Simon and Weiss, 1991]). The relationship between exploding granules and vertical magnetic fields has been previously analyzed by different authors. In this section we will show a preliminary analysis of the formation of the active region AR 1517 as well as an analysis of the exploding granule within the location of the active region formation. In the next sections we will show only a few sample images to compare and analyse the plasma dynamics. We encourage the reader to visit the author's GitHub repository to inspect the complete time series of flow fields and

their analysis obtained in this work<sup>1</sup>.

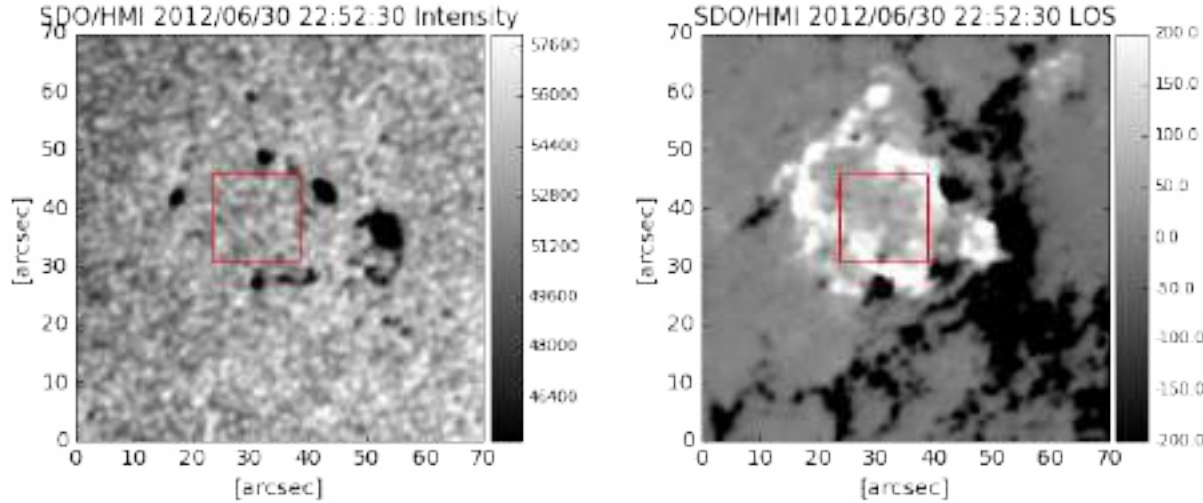


**Figure 4-7.:** SDO/HMI continuum image (*left*) and magnetogram (*right*) of AR1517. The red box demarcates the exploding granule inside of the region of interest (ROI).

The map on the left in Fig. (4-7) shows the mesogranular-sized exploding granule highlighted by a red box in the intensity image. The side length of the box is 15 arcsec. The first emergence (formation of firsts pores) occurred roughly 4 hours earlier than the formation of the first large pore. Figure (4-7) depicts on its right the LOS magnetogram corresponding to the same FOV and time. The black and white structures in the magnetogram highlights the different magnetic polarities.

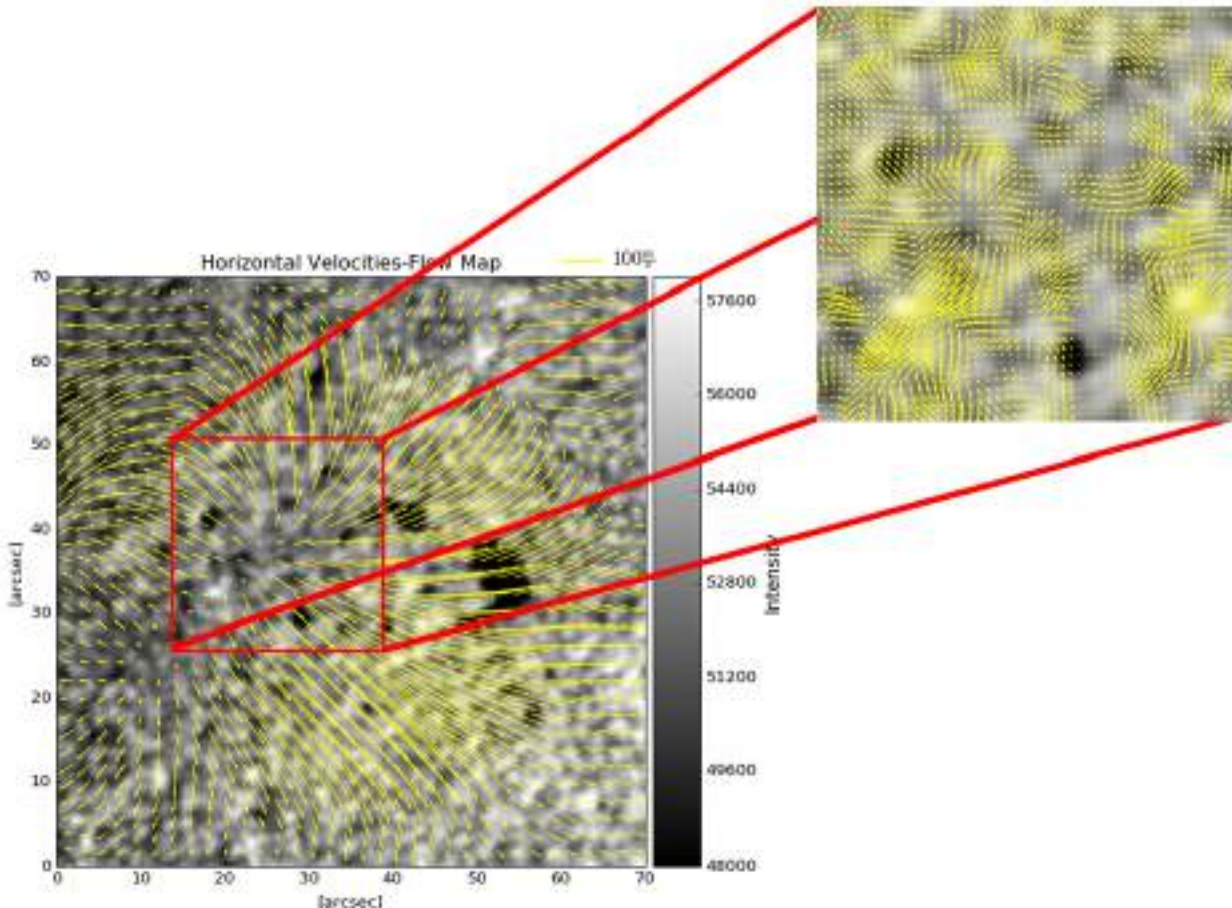
## Emergence and pore formation AR 1517

### Formation stage

We investigate the formation and emergence of a pore that becomes later AR 1517. We reveal the evolution and behavior of the plasma and magnetic field dynamics inferred from horizontal and vertical velocities within a time span of roughly 10 hours. We remind the reader that the size of the cross-correlation window is very important in the study of the different structures.

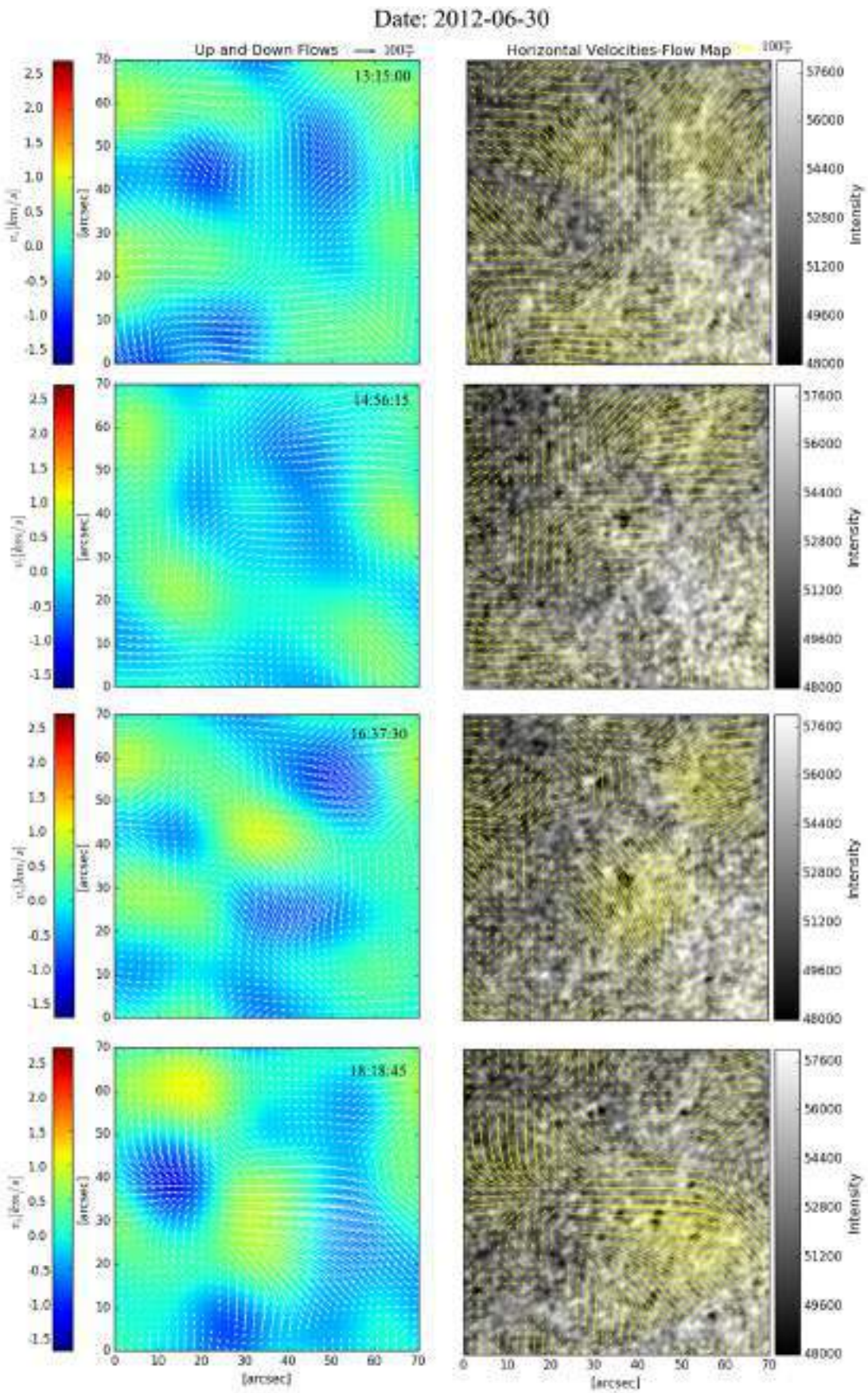
Figure (4-8) shows an example of the difference in the velocity flows when applying different FWHM values. The ROI on the left contains the area of interest that will be studied using a window width  $FWHM = 20$  arcsec (mesogranular sizes) whereas the zoomed region shows results obtained using a  $FWHM = 2.5$  arcsec.

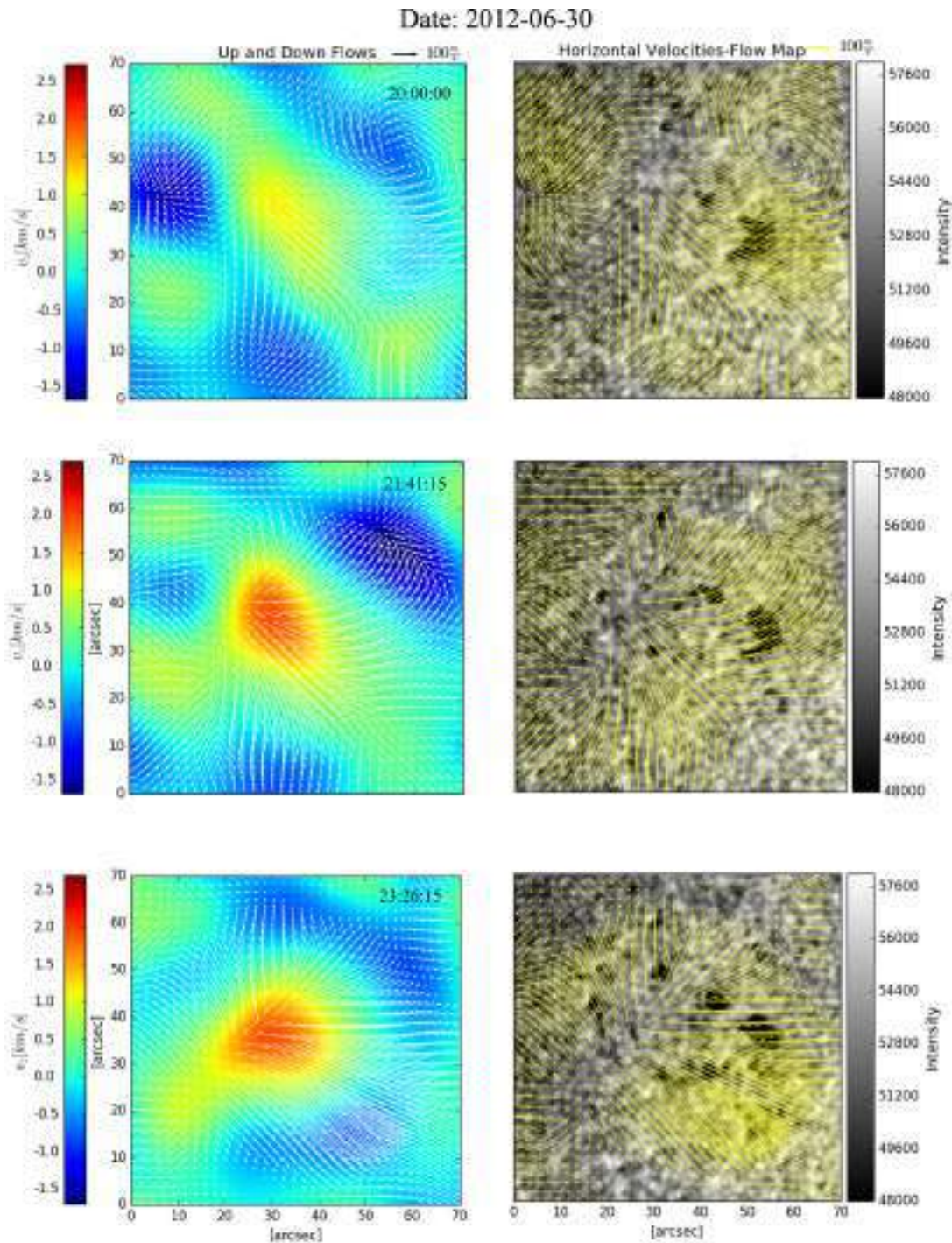
<sup>1</sup>My GitHub profile is: <https://www.github.com/Hypnus1803>



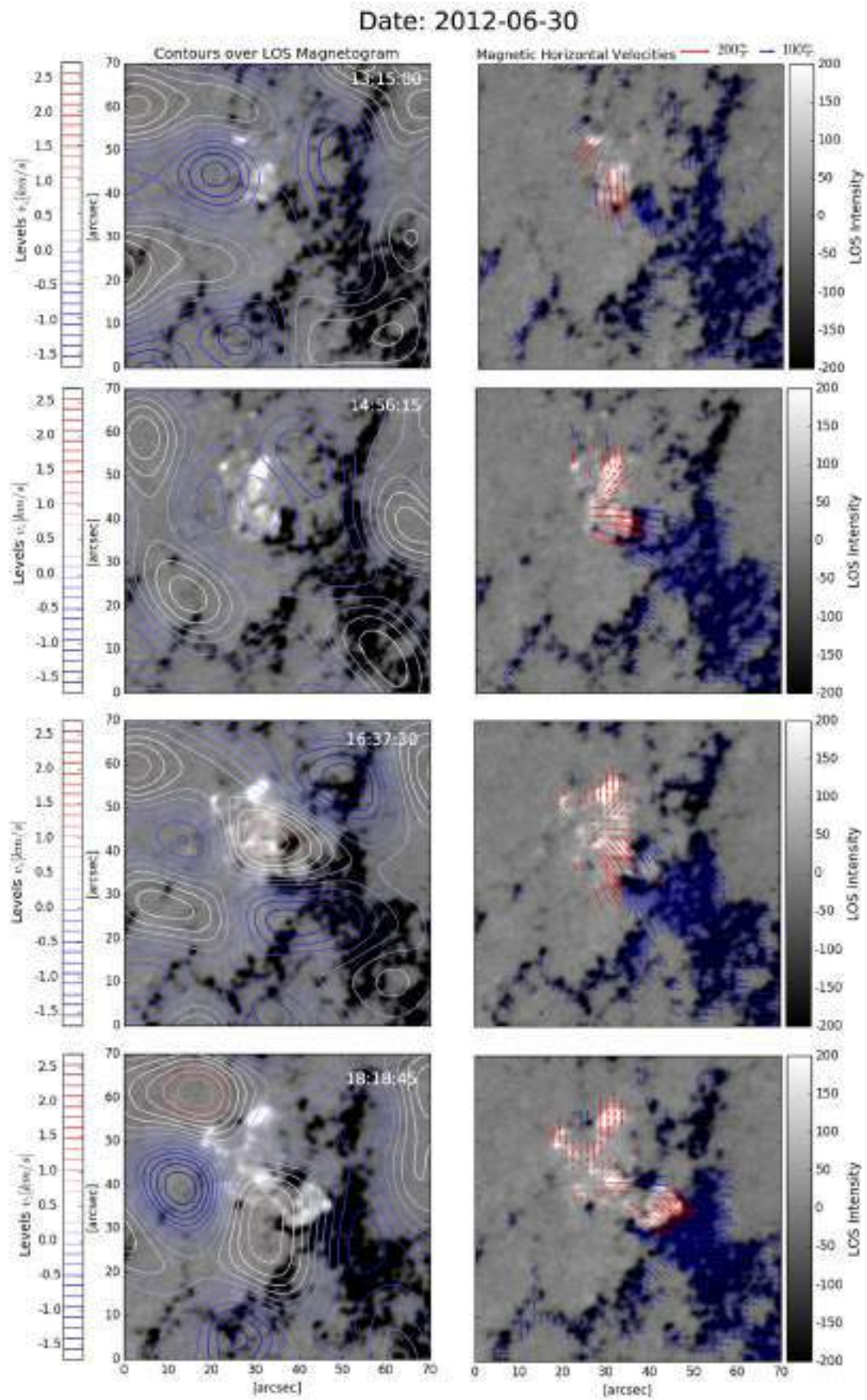
**Figure 4-8.**: Horizontal velocity flow map for an active region with solar pores, resulting from applying a cross-correlation window with FWHM of 20 arcsec (left) and 2.5 arcsec (zoomed region on the top right).

The left plot displays the behavior of mesogranular-sized granules and the brightness displacements calculated using a large correlation window, while the zoomed plot presents the proper motions of granules using a smaller window. Fig. (4-9) illustrates the evolution of a solar pore during the formation and emergence of AR 1517. The *left* images show the vertical velocity map, color-coded in  $\text{km s}^{-1}$ ; the white arrows represent the horizontal velocity field, calculated from intensity maps over 15 minutes and a FWHM of 20 arcsec. Images on the *right* display the intensity map obtained from SDO/HMI with the arrows displaying the same horizontal velocity field. The vertical velocity map is also obtained using the LCT code.





**Figure 4-9.**: Horizontal and vertical velocities during the formation of AR 1517. Left: color-coded vertical (up- and down-flows) velocity map; the arrows display the horizontal velocity field. Right: intensity map with the same horizontal velocities indicated by the arrows. Time evolution shows the emergence of plasma in vertical directions becoming very intense in the region where the mesogranular emergence was identified. Time: 2012-06-30 13:15:00 - 23:26:15 UT.



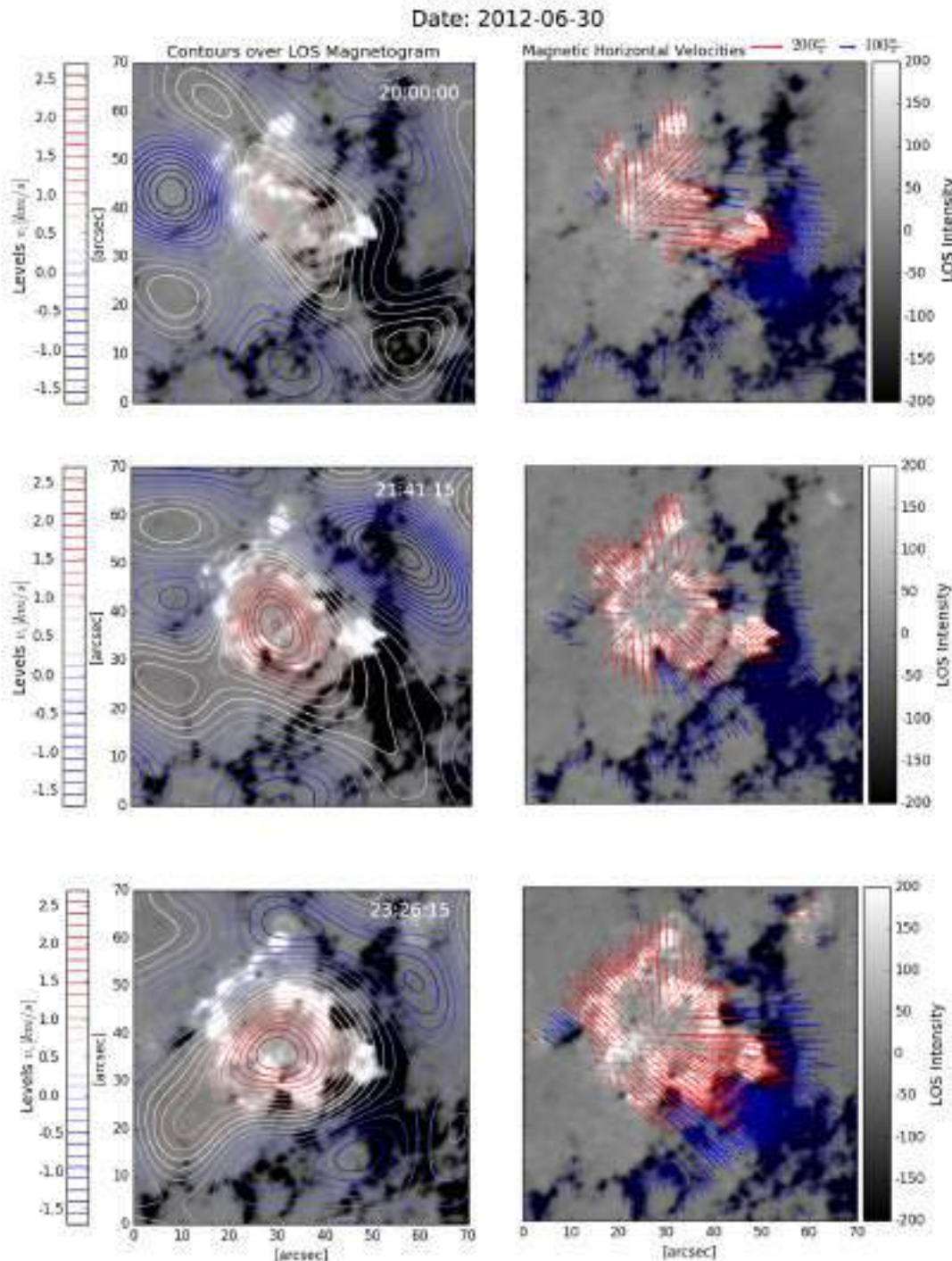


**Figure 4-10.:** Horizontal and vertical velocities (contours) during the formation of AR 1517. left: LOS magnetogram; the color-coded contours represent the vertical velocities obtained from the vertical velocity map. right: same LOS magnetogram with the velocity field estimated from the magnetogram and masked according to the polarity using the parameters mentioned above. Time: 2012-06-30 13:15:00 - 23:26:15 UT.

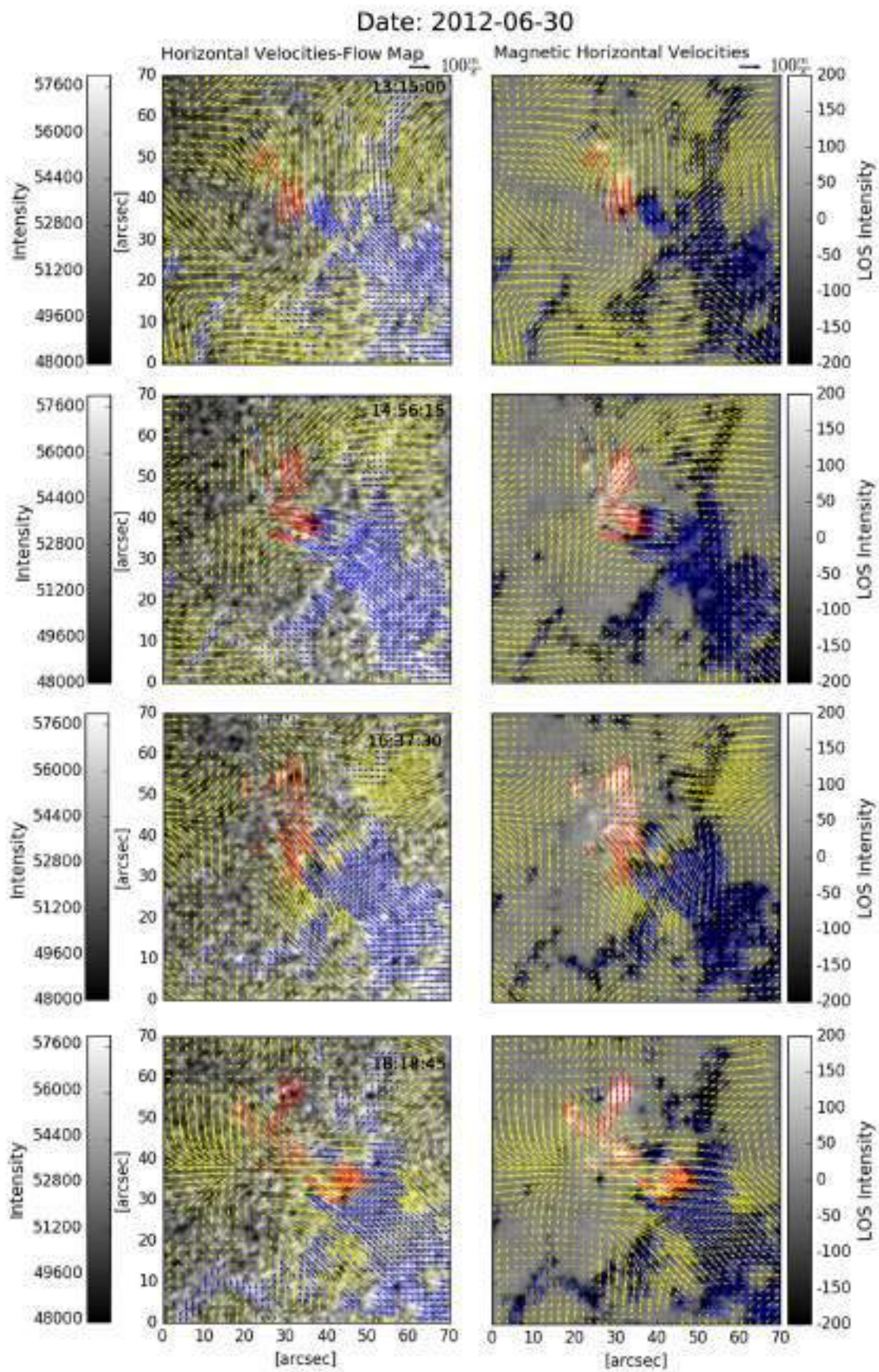
The velocity field obtained from the LOS magnetic field data cube is plotted showing the positive vector magnetic field in red and the negative, in blue. The image saturation procedure has been defined within a magnetic field threshold of  $[-50, 50]$  Gauss.

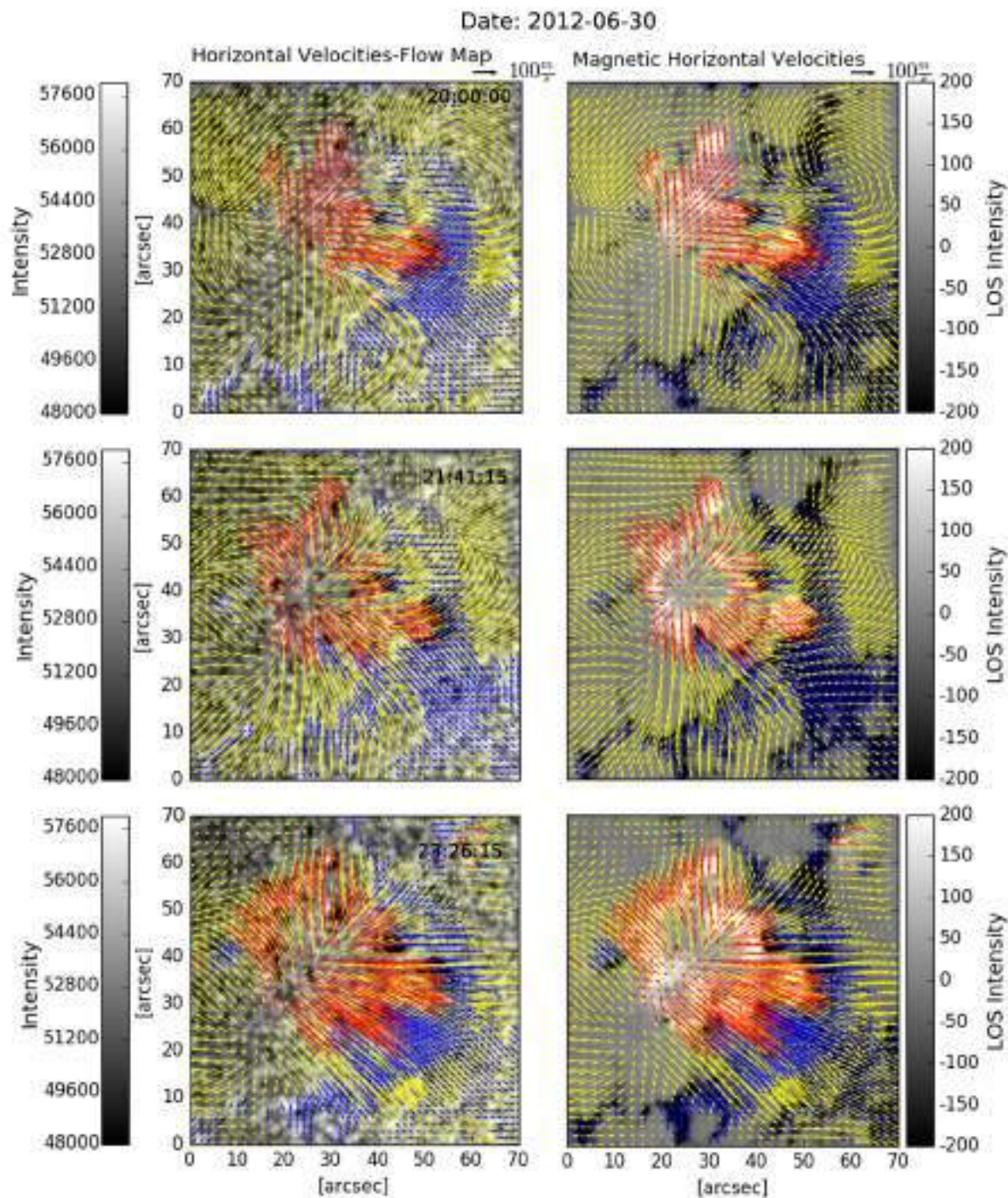
It can be clearly seen that during the evolution of the AR in the ROI marked in Fig. (4-7), a strong plasma emergence occurs (vertical velocity maps in Fig. 4-9 at the last two panels). A strong expansion of positive magnetic flux associated with this emergent plasma occurs over the last 5 hours of this time series (LOS magnetograms of Fig (4-10)). During the emergence of positive magnetic flux on the photosphere, one can follow in detail how the upstreaming plasma carries new positive magnetic fields to the surface, increasing the magnetic flux. We can also see a clear stand off between the photospheric plasma and the emergent magnetic field about the question which one of it should govern the evolution of the atmosphere.

Figure (4-11) displays a composite velocity map obtained from intensity filtergrams and LOS magnetograms. The flow map was plotted after increasing the contrast to provide an easy visual detection and analysis of the continuum intensity maps on the left, i.e. each image was clipped between 75% and 95% of its intensity maximum. The LOS magnetic field maps on the right, taken at the same time, have their values clipped to be greater than 200 Gauss and lower than  $-200$  Gauss through the entire time series. Composition of the velocity vector fields calculated over the intensity data cube (yellow arrows) and the LOS magnetograms (red arrows for the positive magnetic polarity employing a threshold of  $> 50$  Gauss and blue arrows displaying the negative magnetic polarity according to a threshold of  $< -50$  Gauss) with the cross correlation window set to a  $FWHM$  of 20 arcsec and a temporal averaging period of 3m 45s. Figure (4-11) covers around seven hours of evolution of the developing active region with a temporal separation between each snapshot of 1h 30m. During the initial magnetic field emergence, the plasma flows determine the displacement direction (see Fig. 4-11, first two rows) where the strong motions of plasma stand out, dominating the interaction processes between the plasma and the magnetic field.

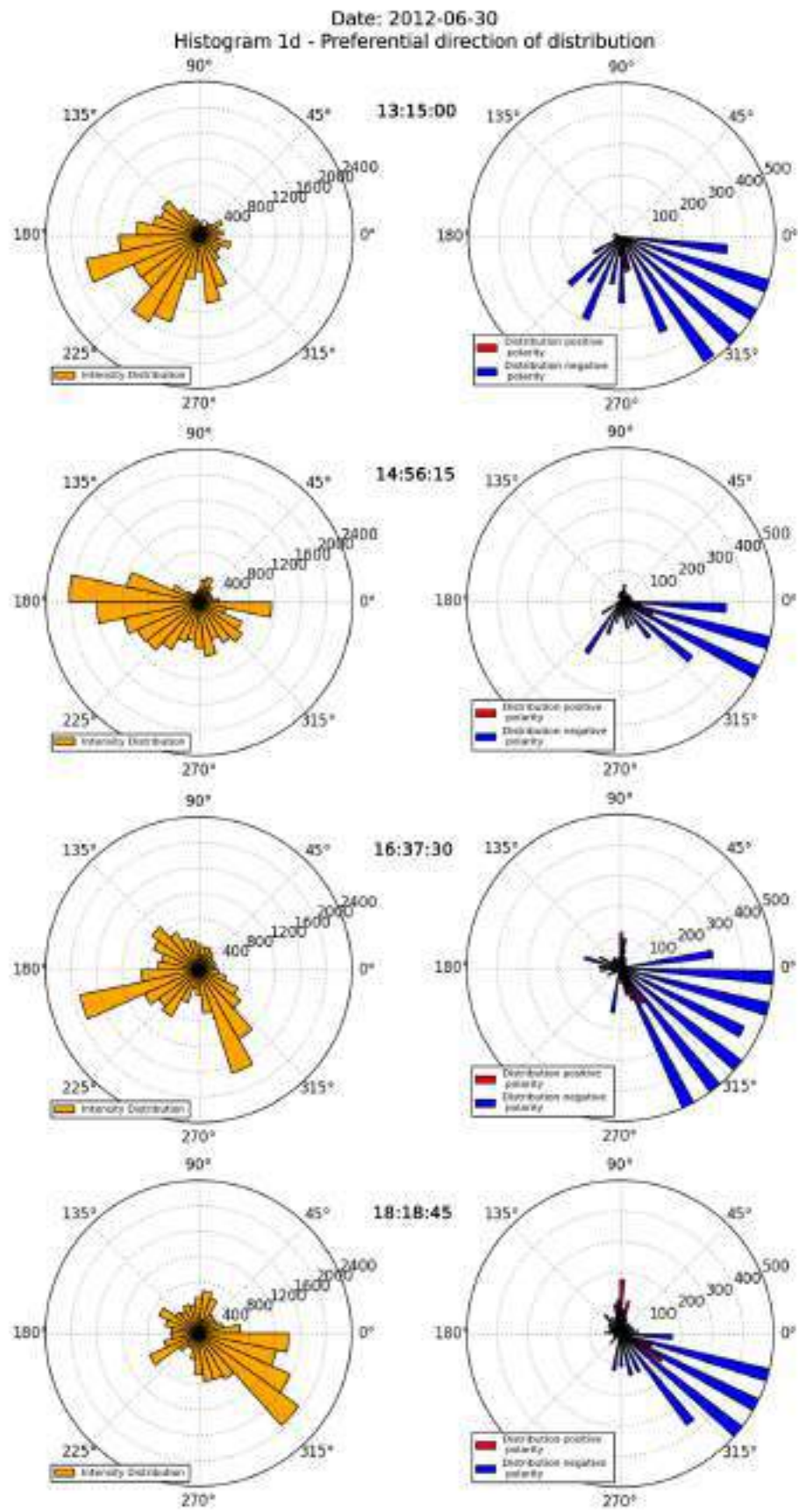
Figure (4-11) shows at the fifth row a disturbance close the coordinates  $(60, 50)$  arcsec, that has the appearance of a vortex. The vortex displayed by the flows map obtained from the intensity data cube (yellow vectors) could be due to the increasing of outward velocity of positive magnetic field changing abruptly the direction of plasma motions.

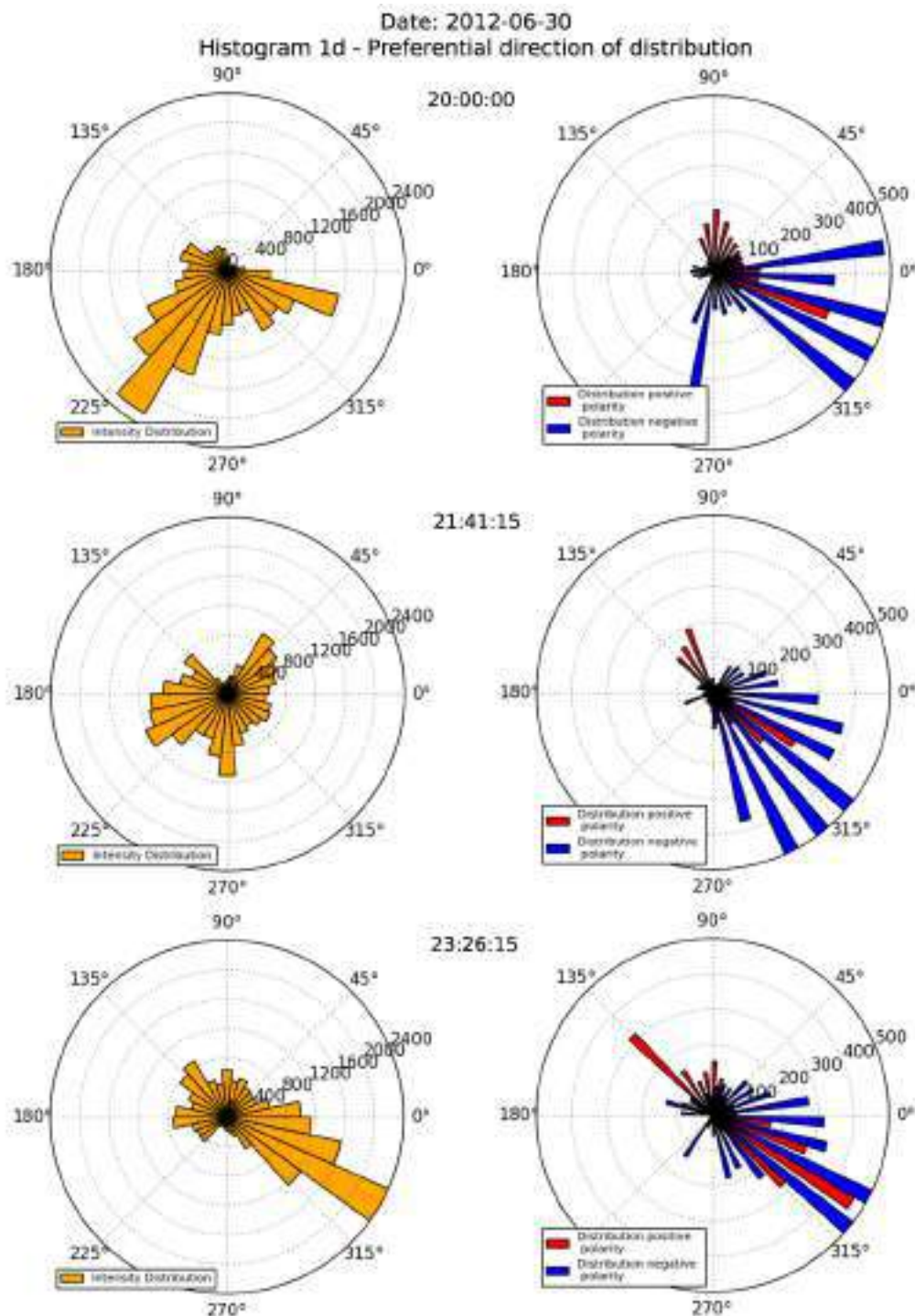
When the positive magnetic field begins to increase its strength, as well as its surface fraction (size) – last three rows –, one can clearly observe that the plasma dynamics are governed by magnetic field motions (expansion). The magnetic field expansion forces the plasma to follow new paths imposed by the magnetic field. At the end of the time-sequence it becomes clear that the plasma moves along the direction of displacement imprinted by the magnetic field, and in the center of the positive magnetic element, the length of the yellow arrows (plasma velocity magnitude) is lower than those for the magnetic horizontal velocity.



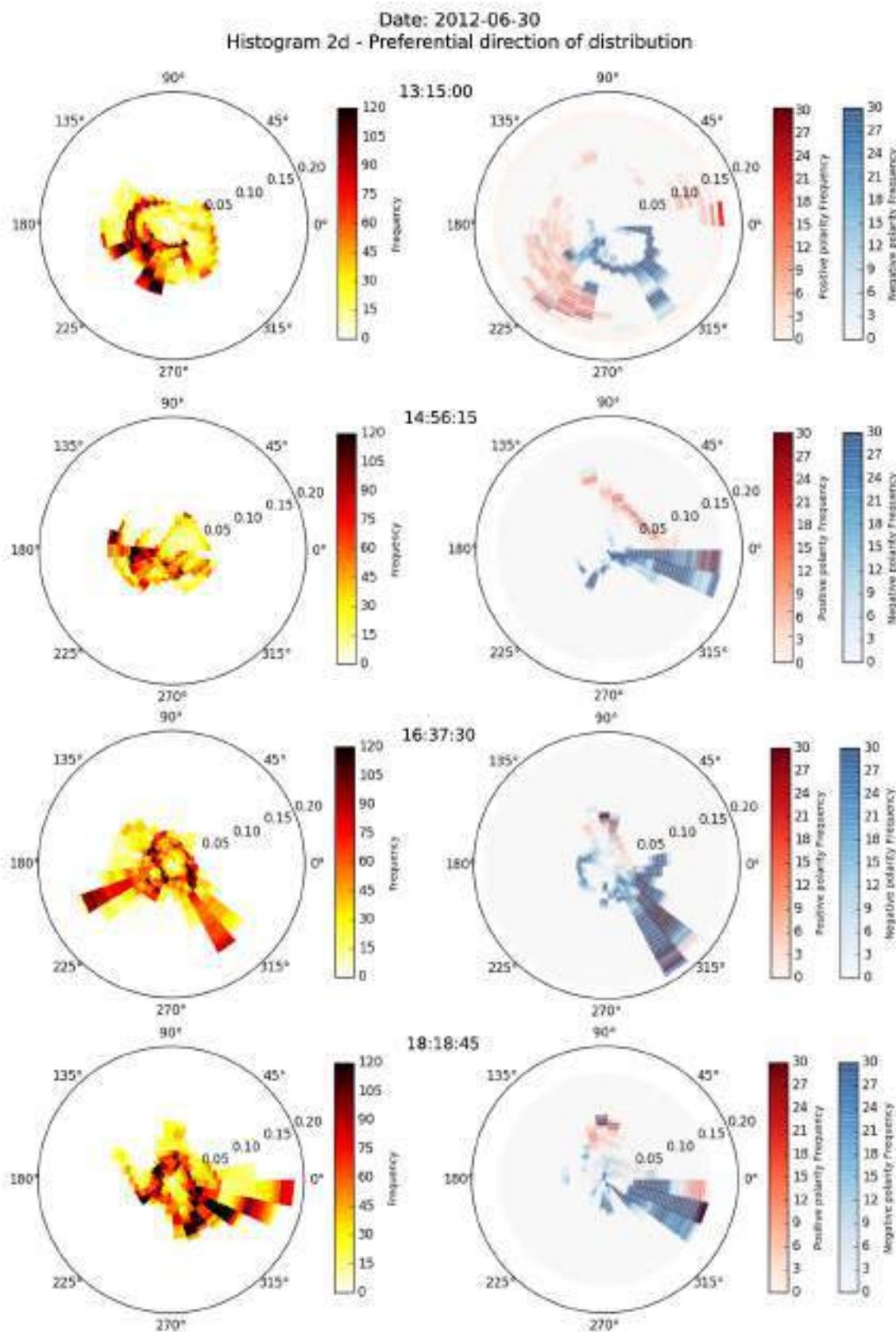


**Figure 4-11.**: Figures showing a composition of vector field velocities for the plasma displacements (yellow arrows) and magnetic polarities proper motions (red arrows: positive polarity; blue arrows: negative polarity). Left panels show in the background the evolution in time of intensity images, meanwhile the right images display the corresponding evolution of the LOS magnetic field with the overplotted velocities field. Time: 2012-06-30 13:15:00 - 23:26:15 UT.





**Figure 4-12.**: These figures illustrate the time evolution of 1d-histograms of velocity distributions for the preferential direction of the plasma motion on the left, meanwhile the right side displays the 1d-histogram displacement distributions for the magnetic elements. The leftmost plots show the direction and magnitude distribution of the proper motions calculated over intensity data (plasma) and the right ones display distributions for the LOS magnetograms (magnetic field). Time: 2012-06-30 13:15:00 - 23:26:15 UT.



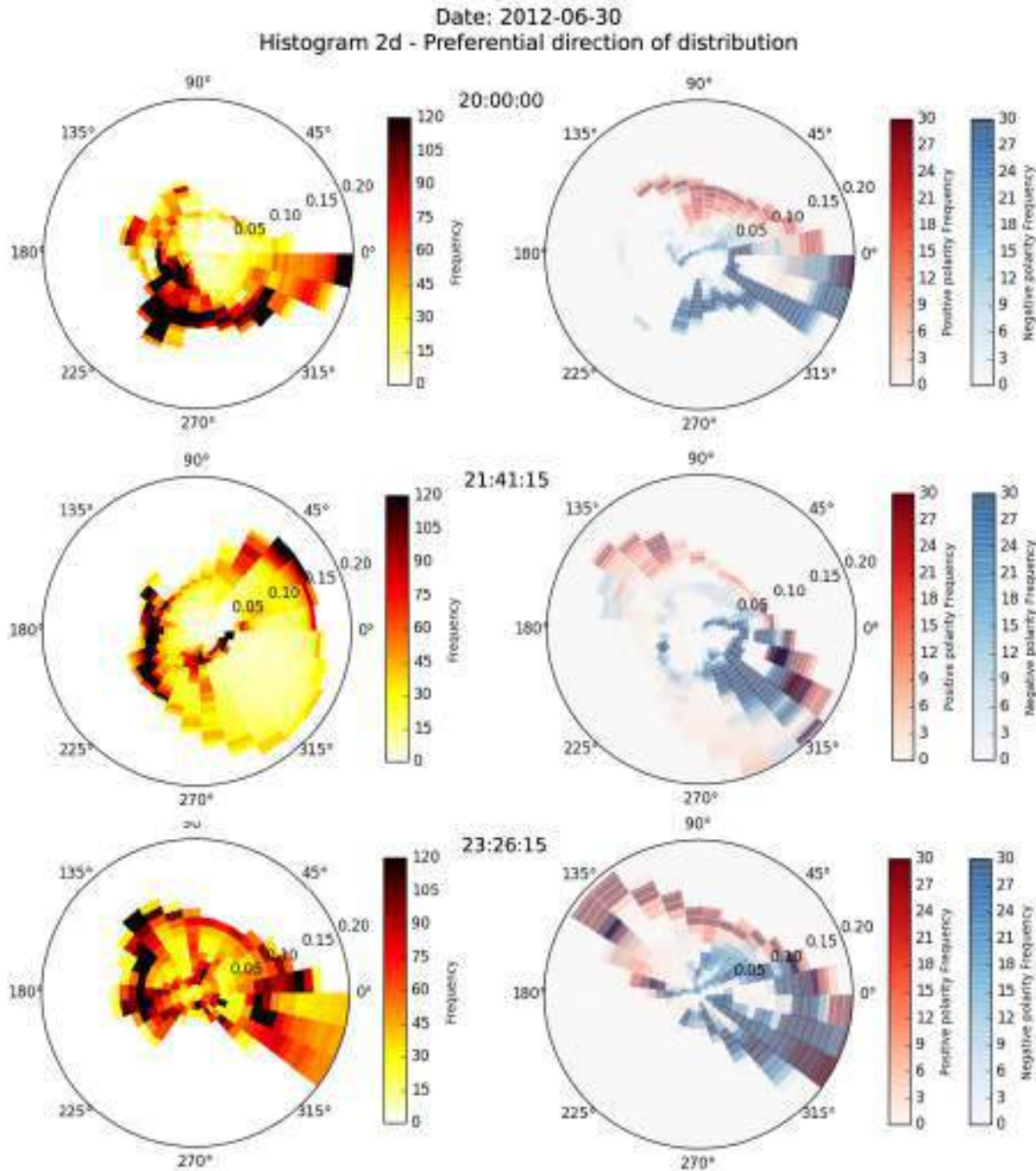


**Figure 4-13.:** These figures show the time evolution of 2d-histograms of velocity distributions for the preferential direction of the plasma motion on the left, meanwhile the right side displays the 2d-histogram displacement distributions for the magnetic elements. In these figures, the radial axis expresses the magnitude values for a given velocity in a fixed angle and the colorbar represents the frequency at which the indicated vector can be found with a given angle and magnitude. Time: 2012-06-30 13:15:00 - 23:26:15 UT.

The histograms are divided into eight sectors (I:  $0^\circ - 45^\circ$ , II:  $45^\circ - 90^\circ$ , III:  $90^\circ - 135^\circ$ , IV:  $135^\circ - 180^\circ$ , V:  $180^\circ - 225^\circ$ , VI:  $225^\circ - 270^\circ$ , VII :  $270^\circ - 315^\circ$ , VIII:  $315^\circ - 360^\circ$ ). It is clear that there is a strong preference of motions towards quadrants VII and VIII for the negative component of the magnetic field while the positive component of the magnetic field moves both, towards the quadrants VII and VIII, and in the direction of quadrants III and IV. From Fig. (4-9) it can be seen that while the mesogranular-sized granule is emerging, positive magnetic field begins to expand and to push out the pre-existing magnetic field. The change in behaviour of the surface flows can be clearly seen. At the beginning the flow structure displays smaller patches, which are highly dynamic and variable with short lifetimes. Afterwards, they become larger, with larger amplitudes and less dynamic, meaning staying longer on the same spot. The contours show that the change in the upflowing emergence regions is highly dynamic. Figure (4-14) shows various contour levels obtained from upward  $v_z$  velocities derived via the LCT technique. Taking into account only those regions contained inside closed contours closest to the center (we will refer to them from here onwards as "cells"), we estimate the evolution in time of the area and the magnetic flux at four different lower limits for vertical velocities ( $0.4 \text{ km s}^{-1}$ ,  $1.0 \text{ km s}^{-1}$ ,  $1.5 \text{ km s}^{-1}$  and  $2.0 \text{ km s}^{-1}$ ). The starting point for our analysis was determined to be 16:00 UT. This was done by visually inspecting the data set from the first occurrence of a cell (closed strong upflow contour line) to the center of the FOV. Previous to the starting time the found cells are neither stable nor close enough to the center of our ROI. The values given at each contour line are measured in  $\text{km s}^{-1}$ .

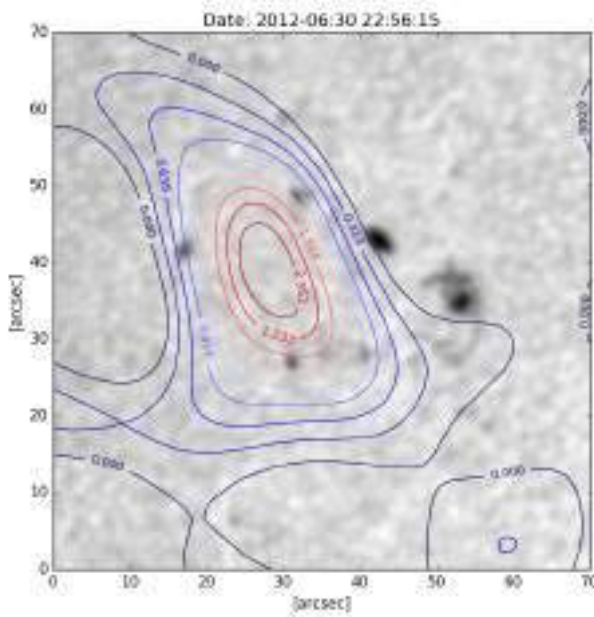


**Figure 4-14.**: Contour levels for upflow velocities ( $v_z > 0 \text{ km s}^{-1}$ ).

Time (2012-06-30)	Mean ( $\mu$ ) [km s $^{-1}$ ]	Standard Deviation ( $\sigma$ ) [km s $^{-1}$ ]
13:15:00	0.047	0.127
13:30:00	0.05	0.131
13:45:00	0.041	0.118
14:00:00	0.042	0.12
14:15:00	0.036	0.111
14:30:00	0.053	0.135
14:45:00	0.048	0.129
15:00:00	0.037	0.113
15:15:00	0.047	0.126
15:30:00	0.045	0.124
15:45:00	0.048	0.129
16:00:00	0.047	0.127
16:15:00	0.042	0.12
16:30:00	0.037	0.112
16:45:00	0.046	0.125
17:00:00	0.049	0.13
17:15:00	0.036	0.11
17:30:00	0.043	0.122
17:45:00	0.051	0.133
18:00:00	0.052	0.133
18:15:00	0.059	0.142
18:30:00	0.072	0.157
18:45:00	0.056	0.138
19:00:00	0.061	0.144
19:15:00	0.054	0.136
19:30:00	0.068	0.152
19:45:00	0.046	0.126
20:00:00	0.068	0.152
20:15:00	0.069	0.154
20:30:00	0.043	0.121
20:45:00	0.082	0.168
21:00:00	0.069	0.153
21:15:00	0.077	0.162
21:30:00	0.053	0.135

**Table 4-2.**: Time evolution of the mean effective velocity (magnitude) for the whole FOV derived via the Rayleigh distribution fits as specified in Eq. (3-2) and Eq. (3-3). Last column tabulates the standard deviation from the statistical computation. It becomes clear that at mesogranular level the plasma velocity is lower compared to normal granular speeds.

Figure (4-15) shows an example of the mask used to calculate the area and magnetic flux inside the contour level. The plot shows the LOS magnetic field contained within the contour. Figures (4-16, 4-17, 4-18 and 4-19) show the time evolution of the variation in areas and the magnetic flux (positive, negative and net flux). We defined the net magnetic flux as the sum of the magnetic field strengths while the positive and negative flux only contains the one or other polarity. For the positive elements we used a threshold  $> 50$  Gauss and for the negative flux we used the threshold  $< -50$  Gauss. The net flux was defined as the addition of the positive and negative fluxes. In order to have the ROI within the demarcated red square of Fig. (4-7), the selected temporal evolution is different compared to the previous analysis. This criterion is fulfilled differently for the different chosen velocity thresholds; e.g. cells with speeds larger than  $0.4 \text{ km s}^{-1}$  appear at  $\approx 16\text{h UT}$ , cells with speeds larger than  $1.0 \text{ km s}^{-1}$  appear at around  $\approx 17\text{h UT}$ , the upward flows with speeds of up to  $1.5 \text{ km s}^{-1}$ , near  $20\text{h UT}$ , while cells with upflows greater than  $2.0 \text{ km s}^{-1}$  appear just before  $23\text{h UT}$ . There is a strong correlation between the areas and the flux, concluding that the variations in the magnetic field flux are related with the size of cells displaying upflowing vertical velocities.

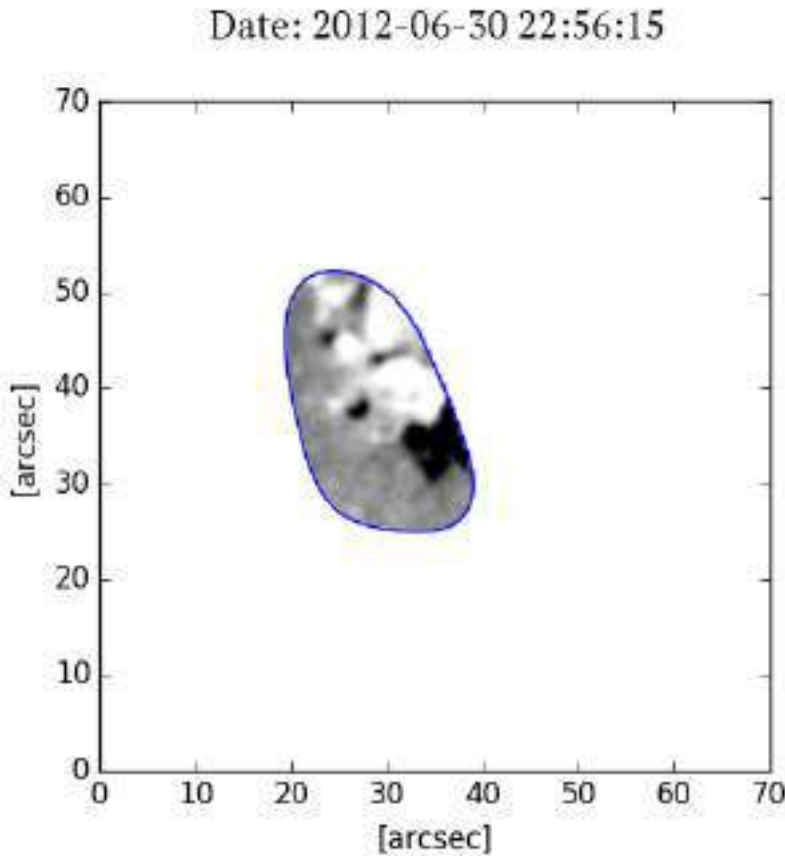


**Figure 4-15.:** Contour level for upflow velocity ( $v_z > 1.5 \text{ km s}^{-1}$ ) at time: 22:56:15.

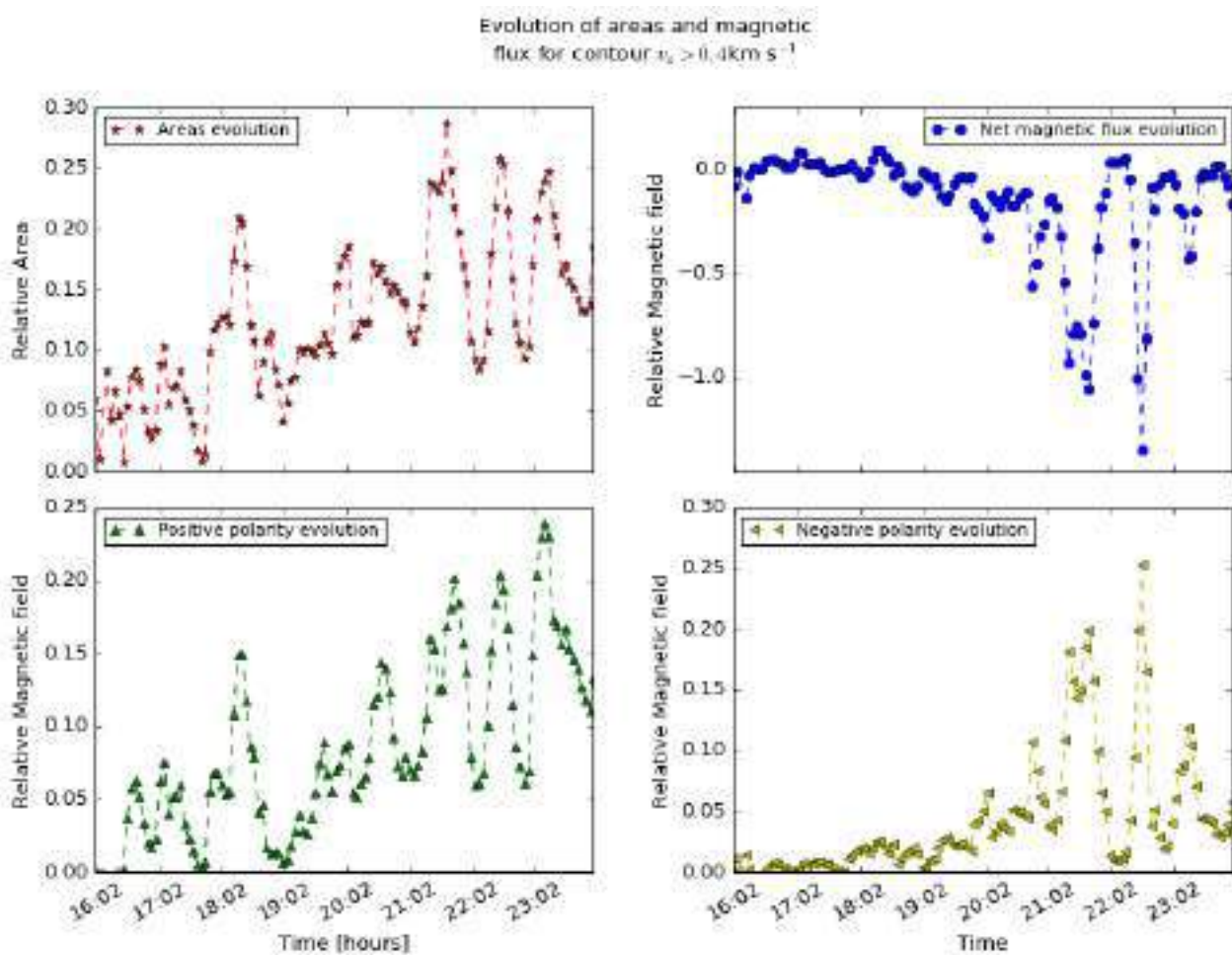


**Figure 4-16.:** Time evolution of the area and fluxes enclosed within the contours generated by upward velocities  $v_z > 0.4 \text{ km s}^{-1}$  starting at 2012-06-30 16:00:00 UT.

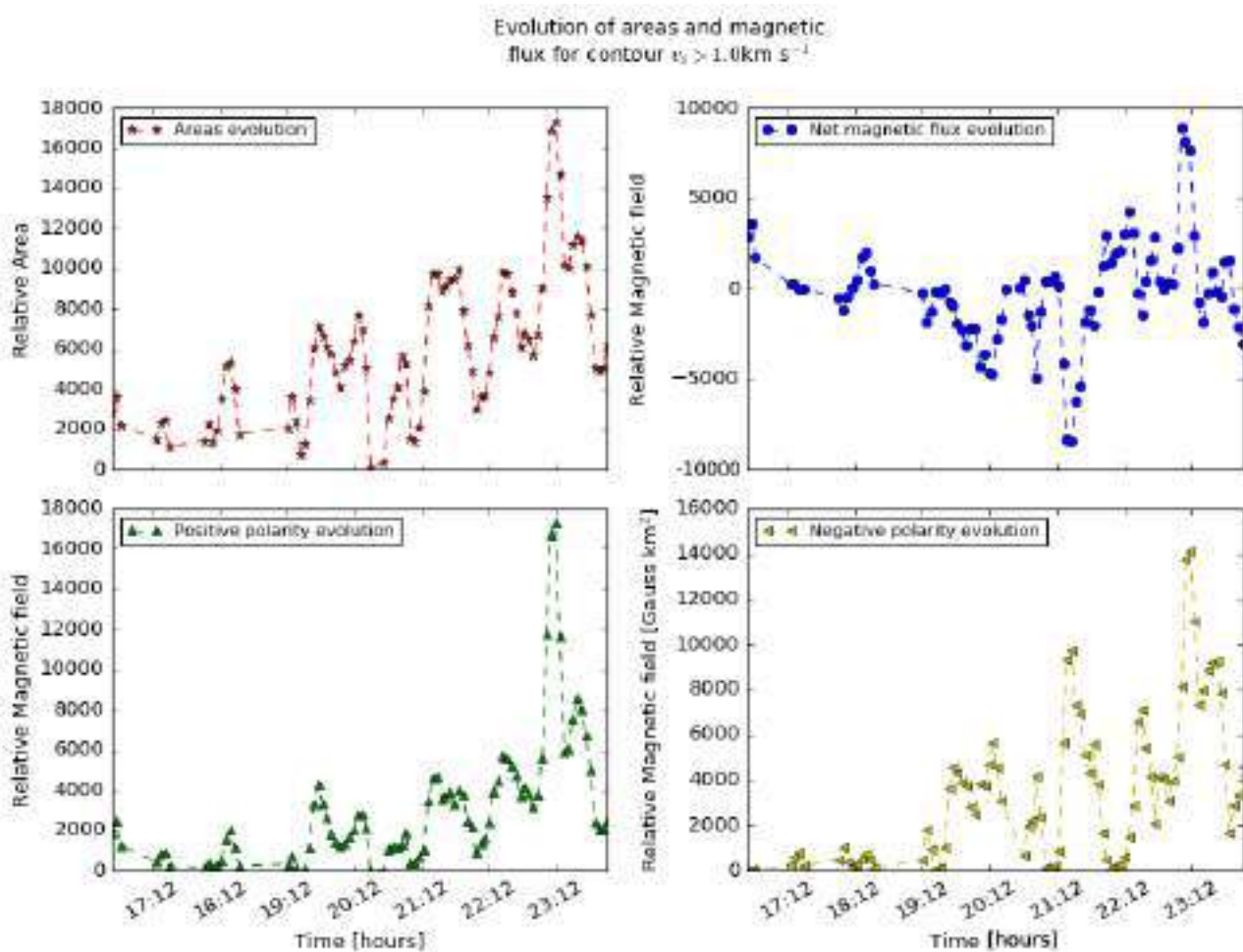


**Figure 4-17.:** Same as Fig. (4-16), but for velocities  $v_z > 1.0 \text{ km s}^{-1}$  and 17:00:00 UT.

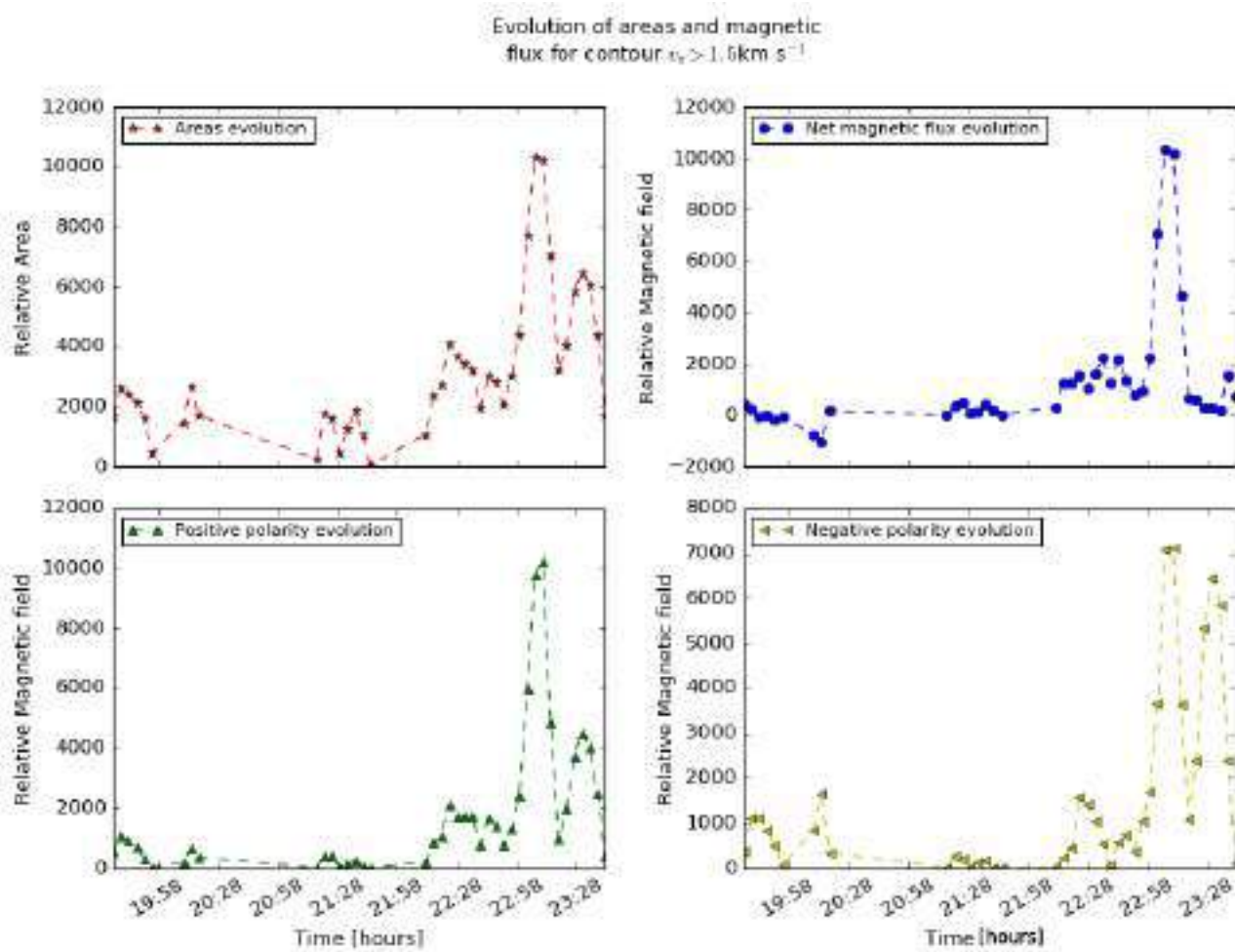


**Figure 4-18.:** Same as Fig. (4-16), but for velocities  $v_z > 1.5 \text{ km s}^{-1}$  and 19:30:00 UT.

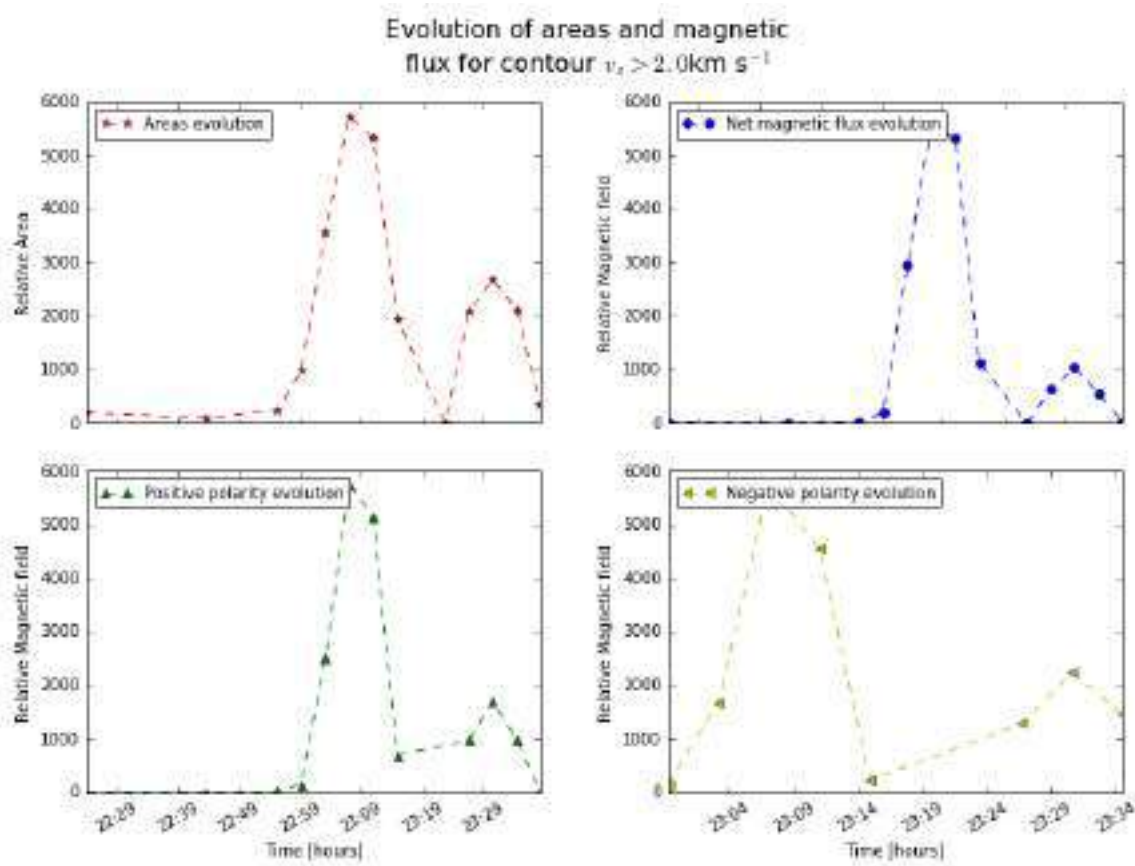


**Figure 4-19.**: Same as Fig. (4-16), but for velocities  $v_z > 2.0 \text{ km s}^{-1}$  and 23:00:00 UT.

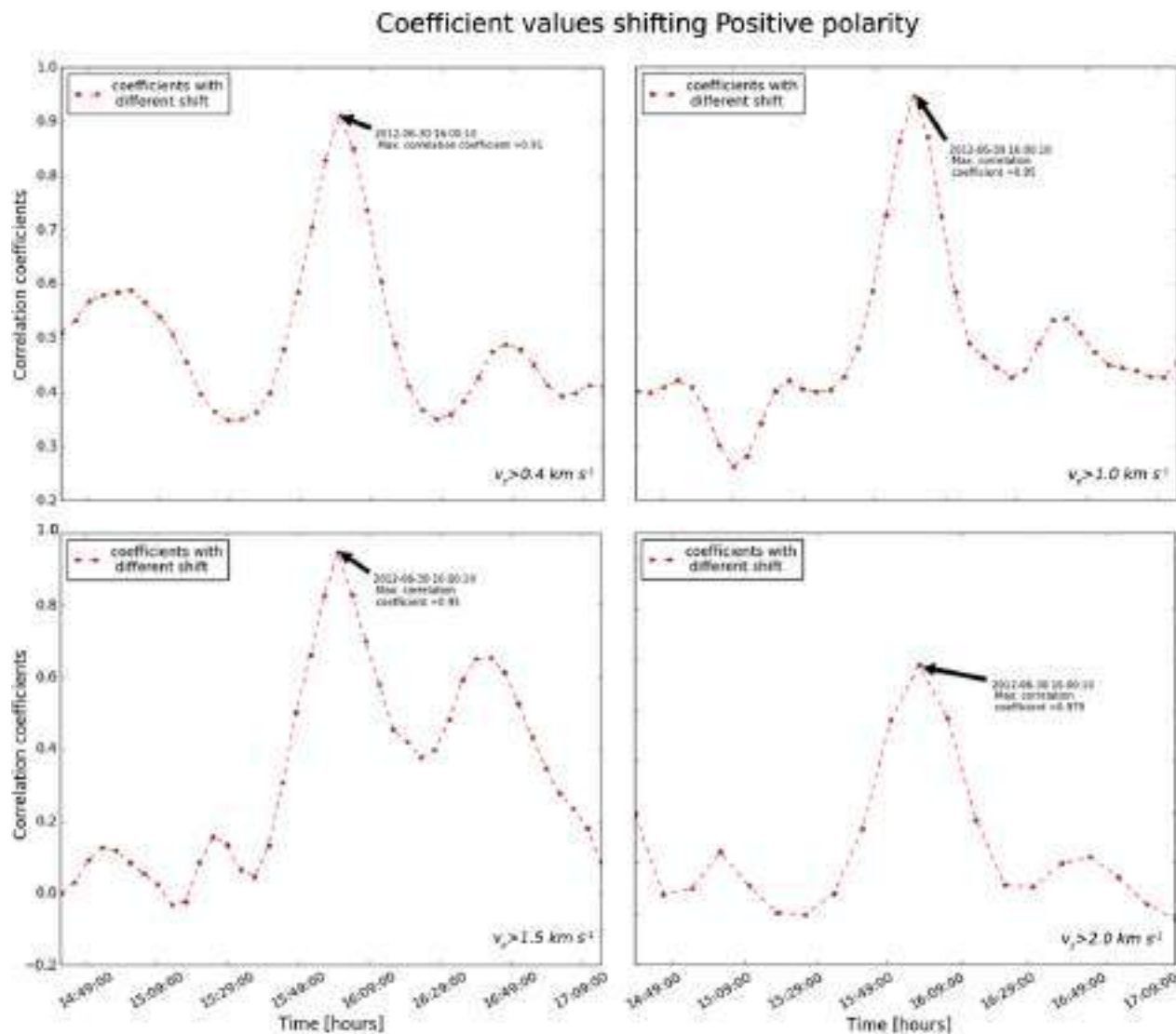


**Figure 4-20.:** Correlation coefficients shifting the positive flux with respect of the areas for  $v_z > 0.4 \text{ km s}^{-1}$ ,  $v_z > 1.0 \text{ km s}^{-1}$ ,  $v_z > 1.5 \text{ km s}^{-1}$ , and  $v_z > 2.0 \text{ km s}^{-1}$ .

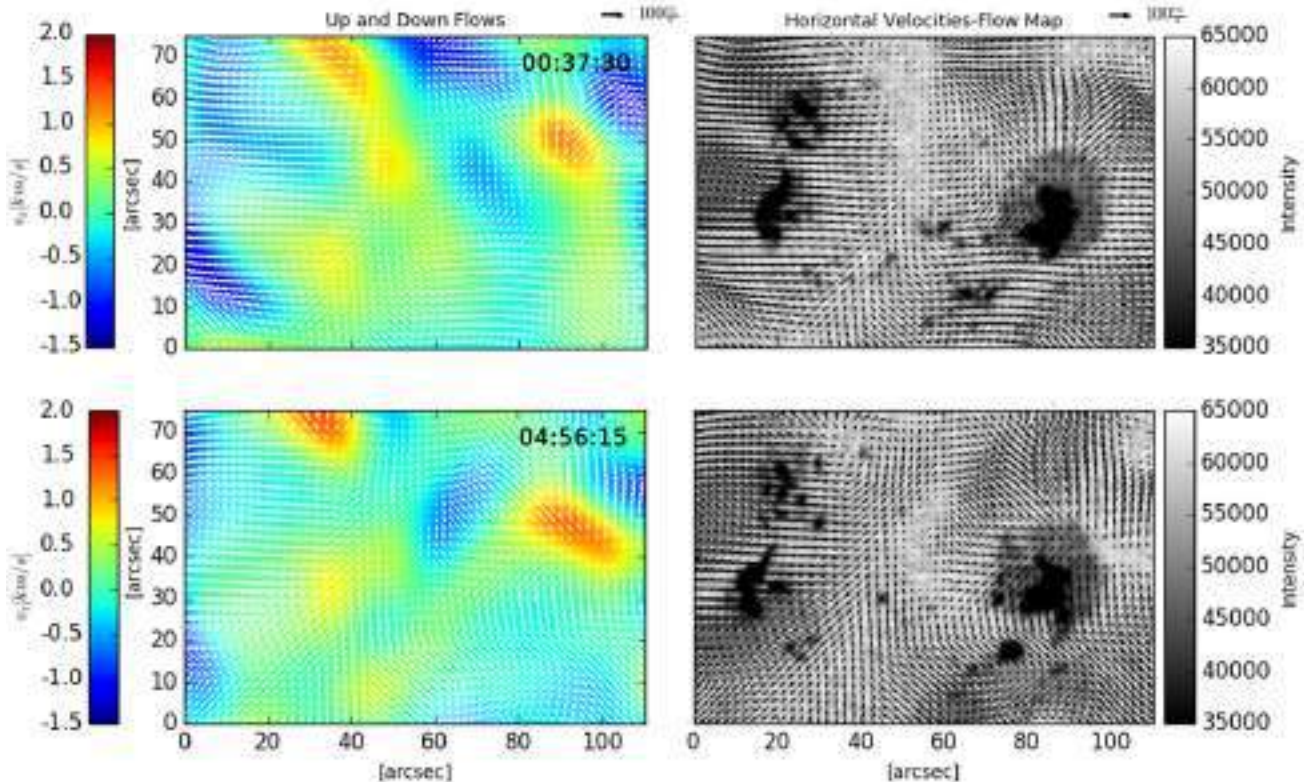
Figure (4-20) shows the cross-correlations between the variations of areas and positive magnetic flux via time to find the best correlation that leads to a maximum agreement between both evolutions. The calculation of errors is difficult because it is a combined error from the magnetic field estimation of HMI with the area determination via the contour plot, which can not be estimated at all in an easy way. This analysis indicates that there is indeed no temporal shift between these two tested quantities, proving that the processes occur co-temporally. Thus one cannot use for instance the size of the upflows to obtain an indication for the upcoming behavior of the magnetic flux within the region.

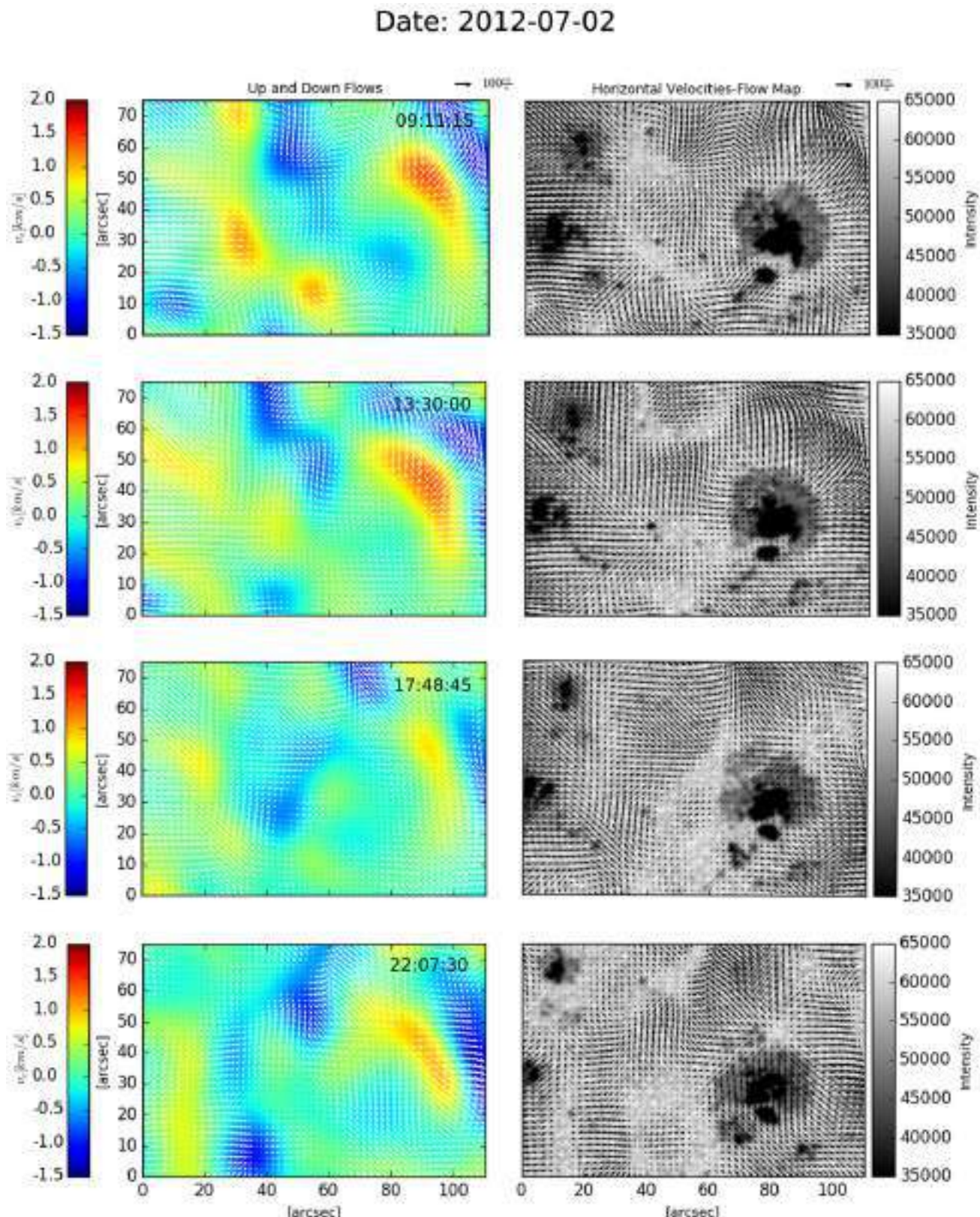
### Stable stage

A study of the active region and behavior of the plasma and the magnetic field, after it has already been formed and reached stability in the FOV, has been made for day 02-07-2012. Figure (4.3) shows the horizontal and vertical displacements resulting from the velocities estimated using the LCT algorithm, similarly as in Fig. (4-9).

The background intensity images have been clipped in the range [35000, 65000], whereas the LOS magnetograms were clipped in the range [-300, 300] Gauss. The contour levels show 15 different levels between [-1.5, 2.0] km s<sup>-1</sup>.

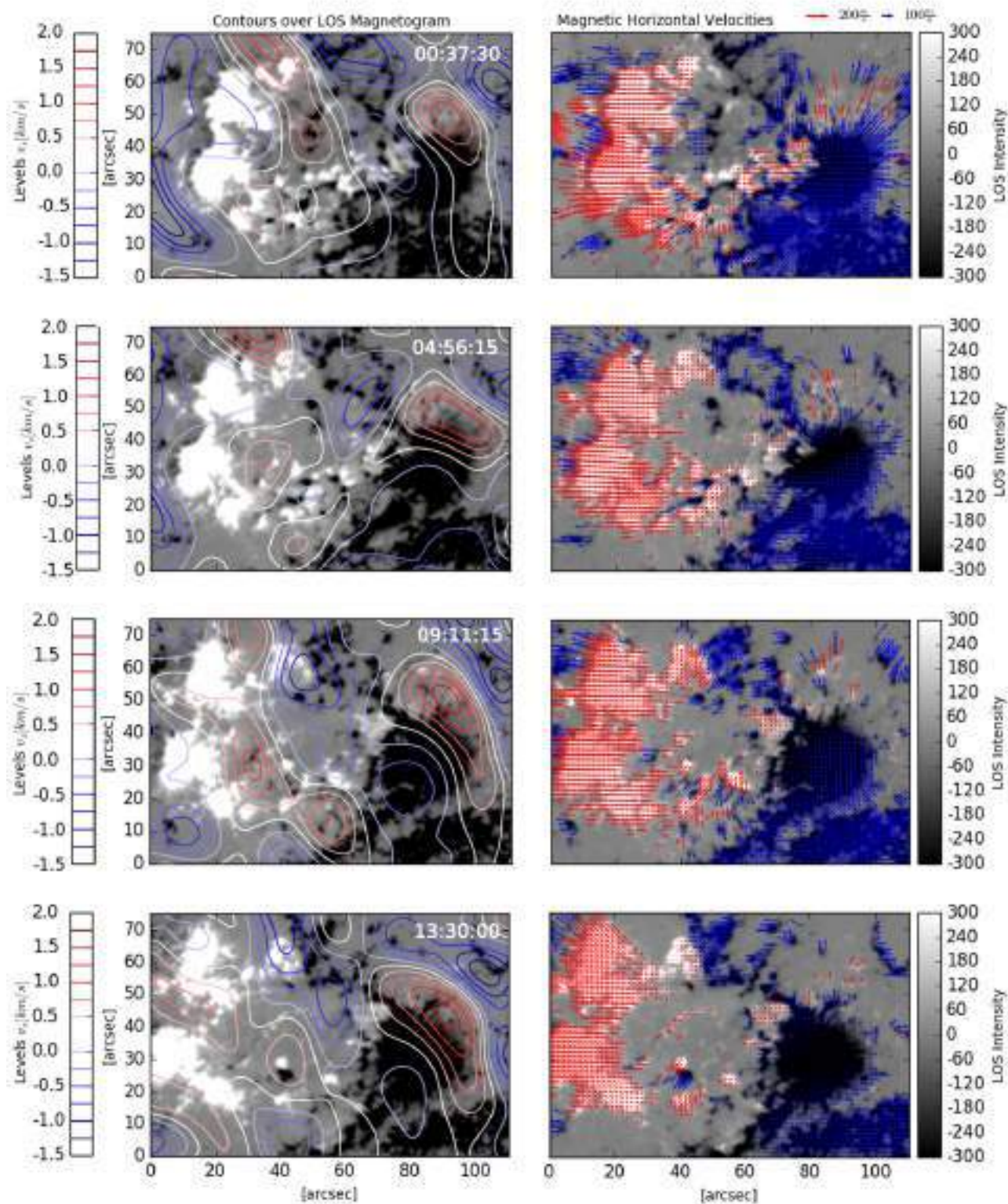
Date: 2012-07-02

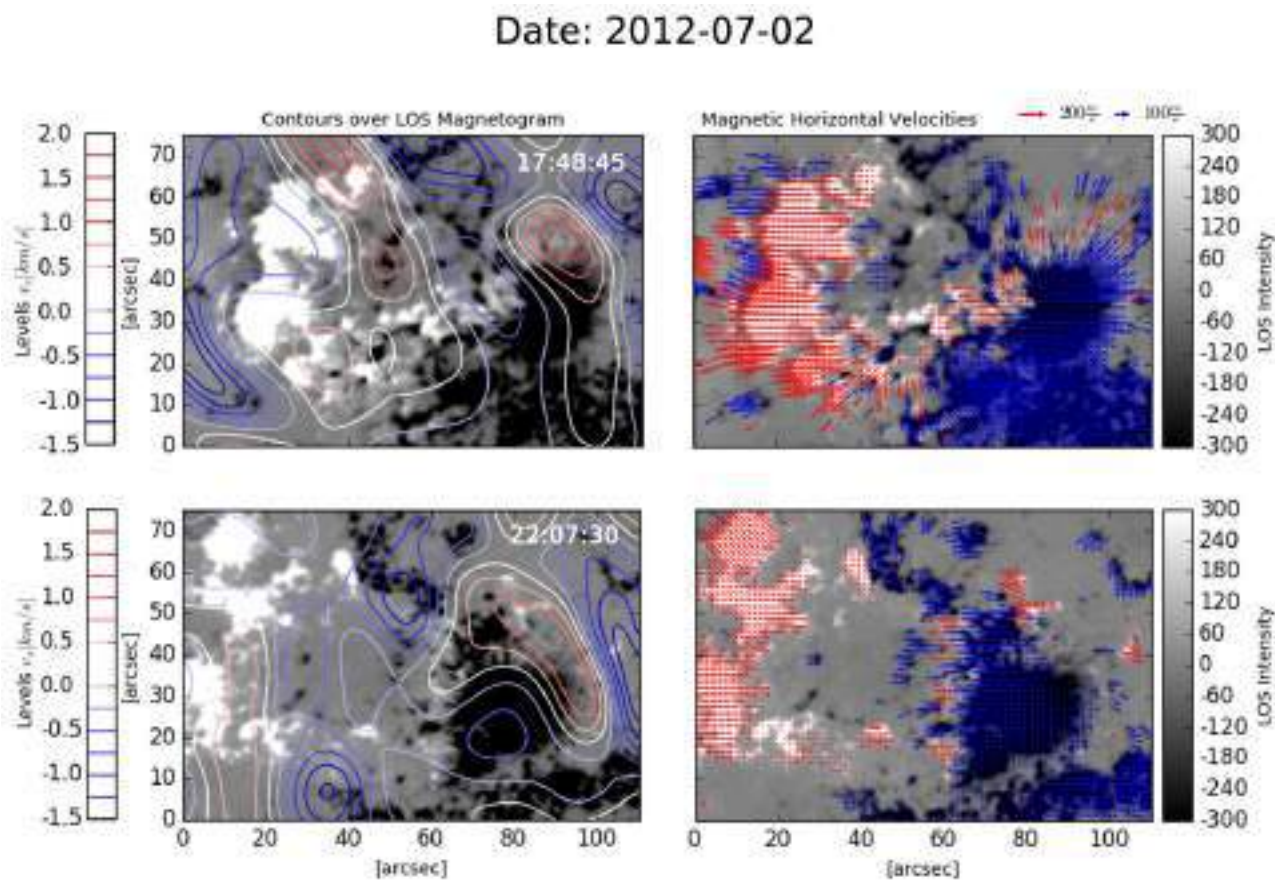




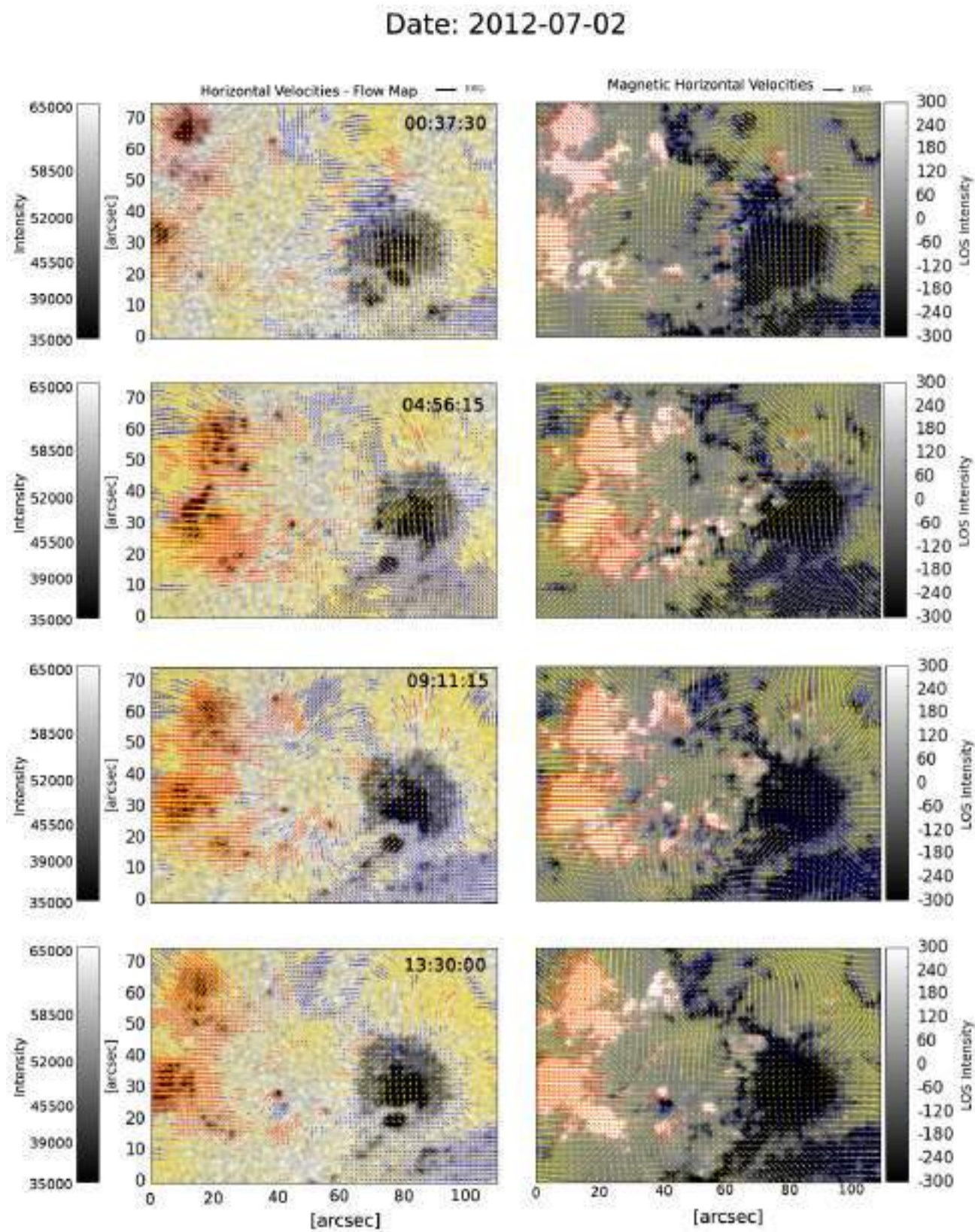
**Figure 4-21.**: Similar to Fig. (4-9), the horizontal and vertical velocities of AR 1517 in the stability phase are given, but for 2012-07-02 from 00:37:30 to 22:07:30 UT.

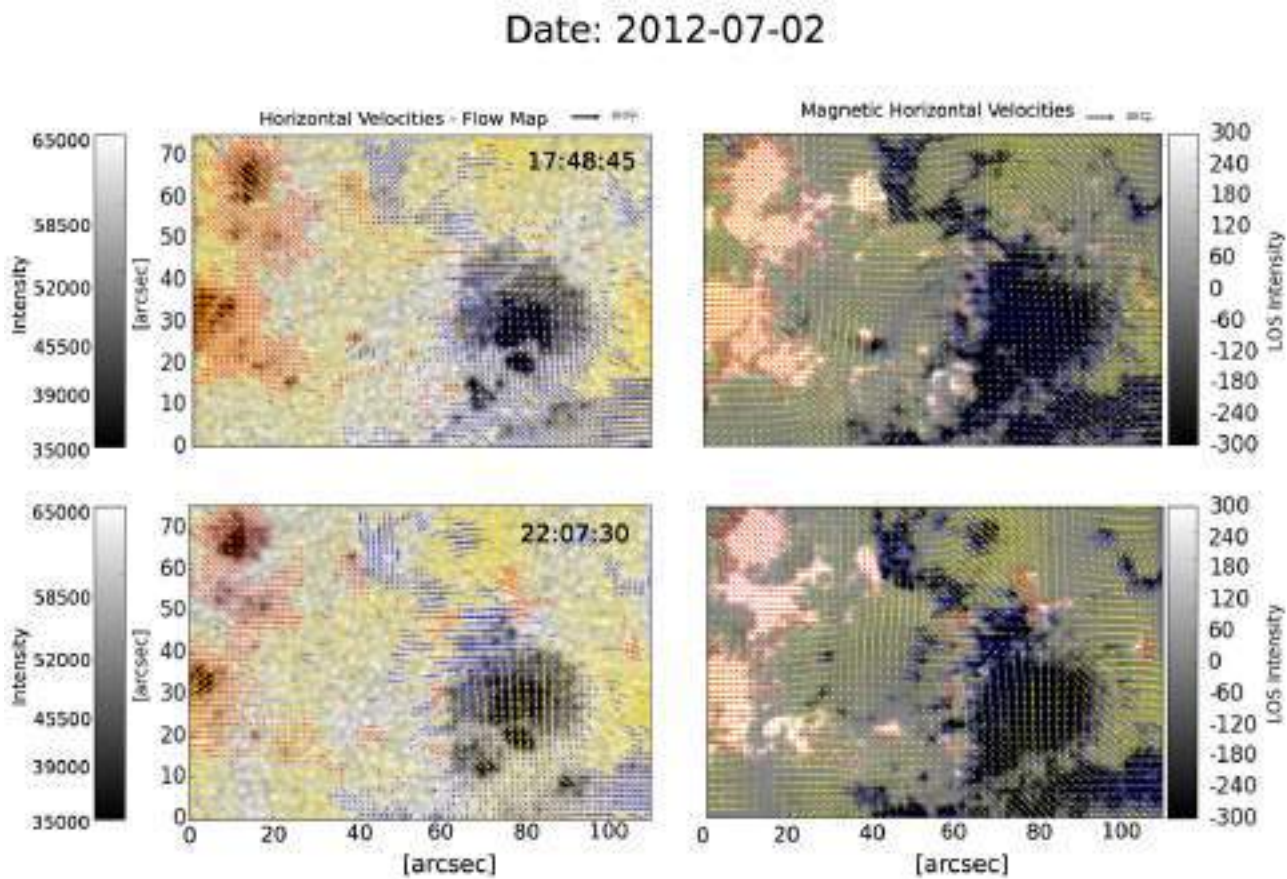
Date: 2012-07-02



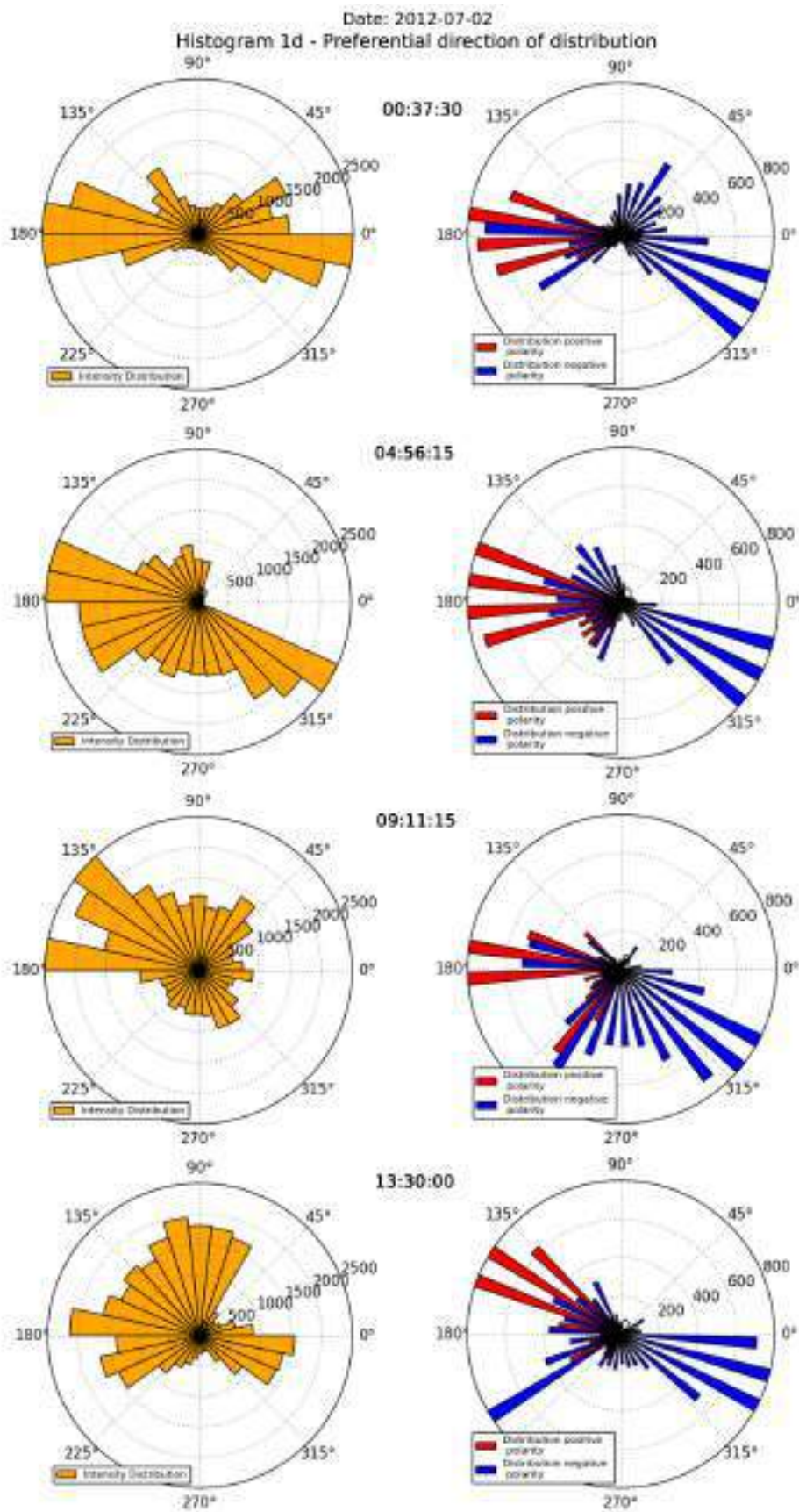


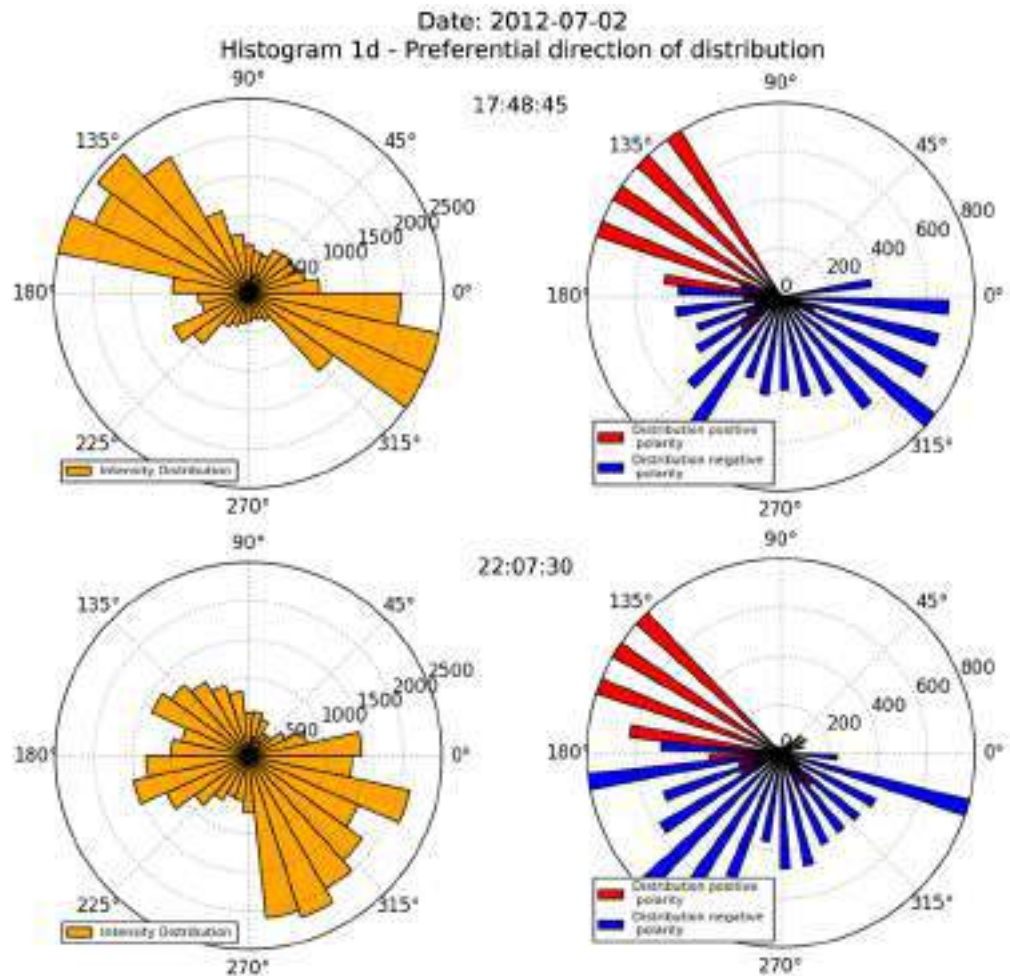
**Figure 4-22.**: Contours obtained from vertical velocities and horizontal proper motions obtained from LOS magnetic fields similar to Fig. (4-11), but for 2012-07-02 from 00:37:30 to 22:07:30 UT.



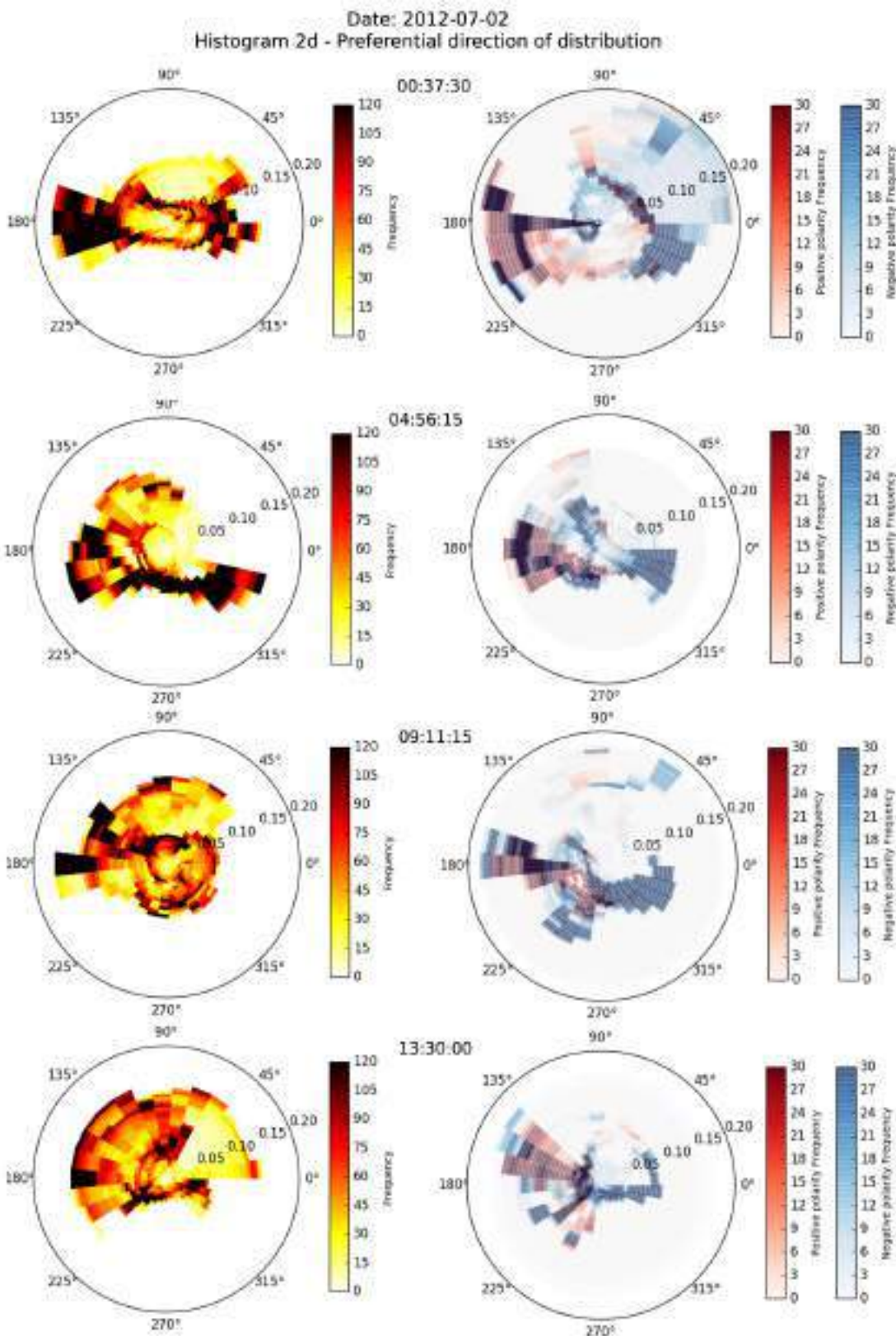


**Figure 4-23.**: Composition image of horizontal velocities split into three different domains according to the magnetic field polarity as explained in Fig. (4-11) (red arrows feature positive polarity fields, blue arrows feature negative polarity, while yellow arrows are plotted in magnetic field free regions).





**Figure 4-24.:** 1-D histograms showing the preferential directions for displacements after AR 1517 reached stability at 2012-07-02 from 00:37:30 to 22:07:30 UT.



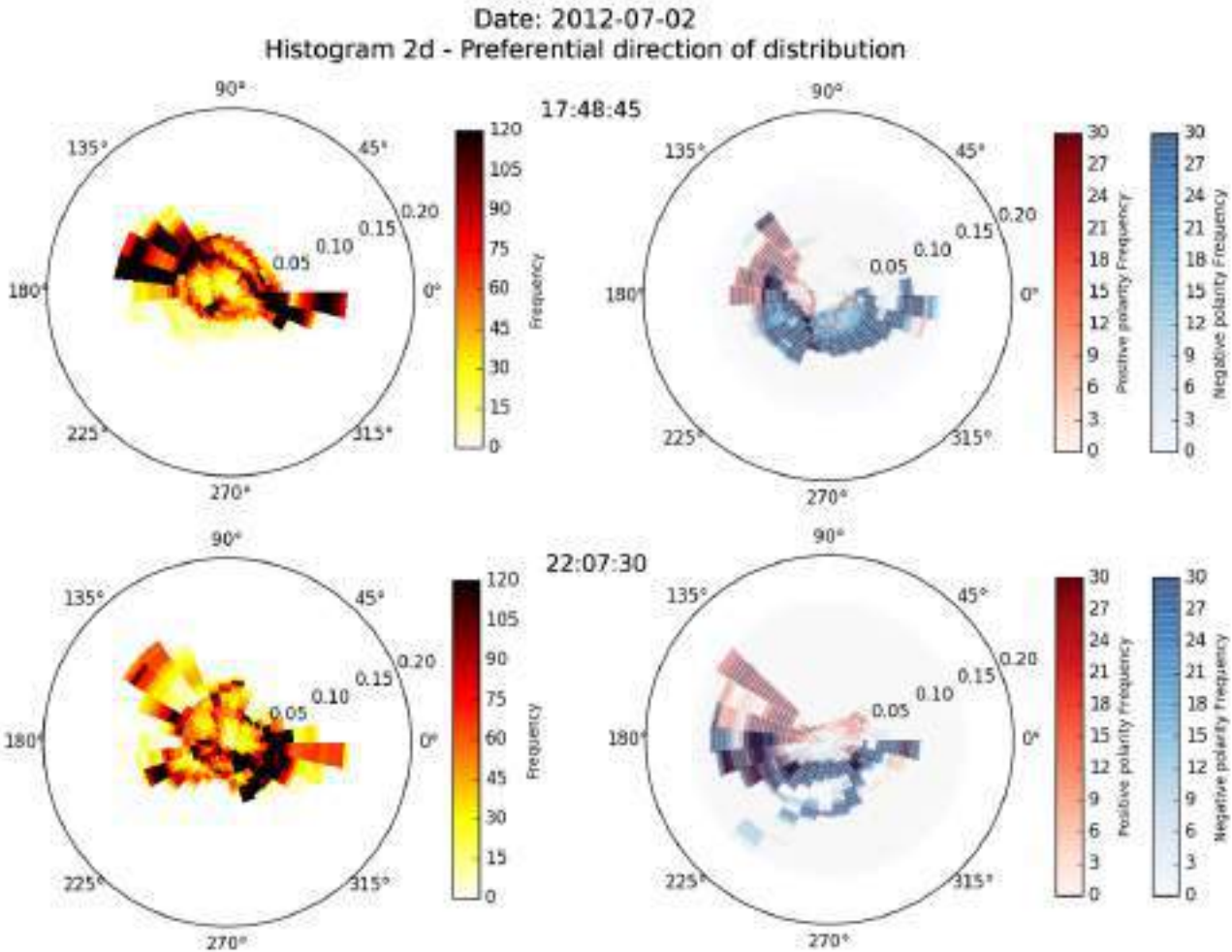


**Figure 4-25.**: 2-D histograms showing the preferential directions for displacements after AR 1517 reached stability at 2012-07-02 from 00:37:30 to 22:07:30 UT.

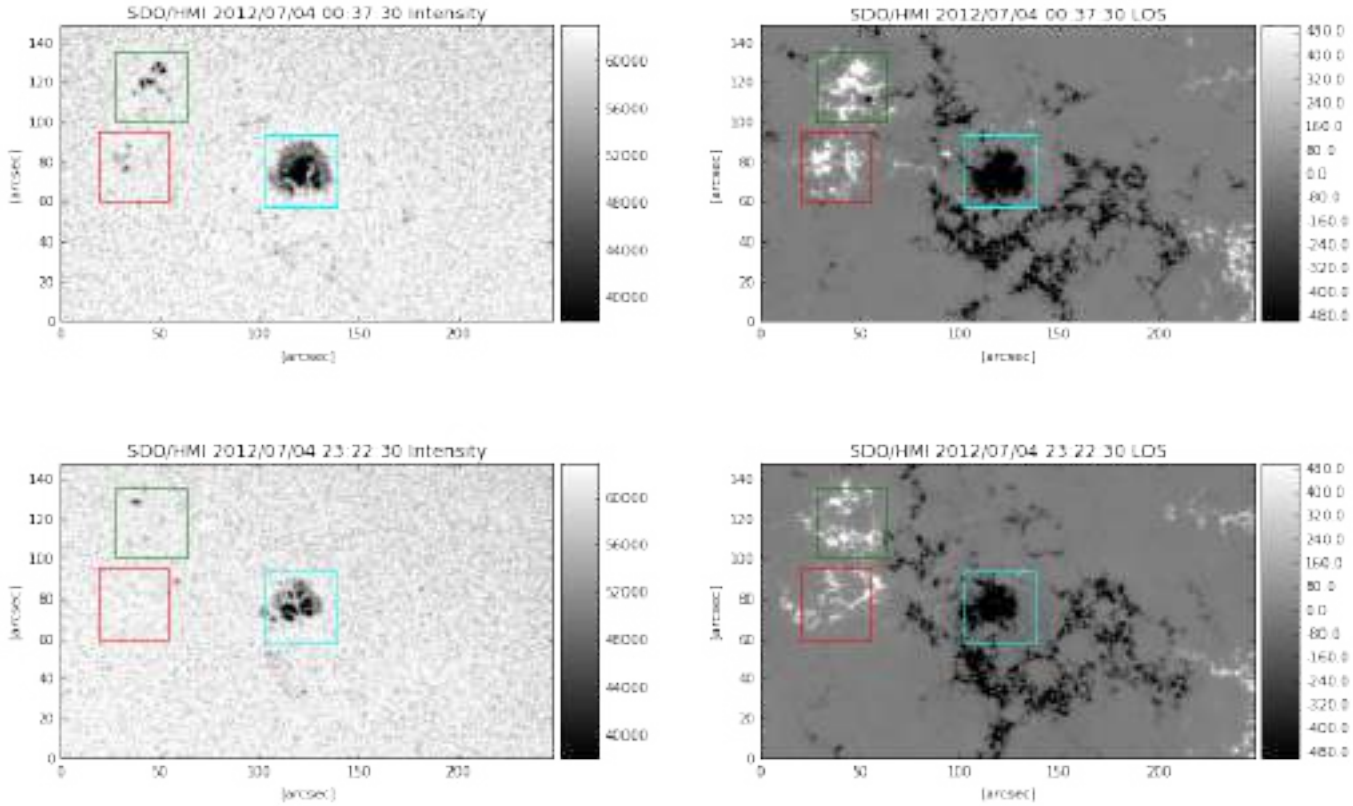
Figure. (4-21, 4-22, and 4-23) present rapid flow emergencies in regions close to the negative polarity zones and more flux emergencies close to the region of positive polarity. A strong change of the preferential flow direction of plasma in the field of view belonging to the negative polarity is also present. Furthermore, it is possible to observe a new direction of general plasma motion for the negative polarity of the active region. One can suppose that this behaviour is caused by the emerging upflowing plasma leading to horizontal movements, which forces this change, modifying the preferential flow directions within the region. The histograms in Fig. (4-24, and 4-25) display preferential directions belonging to range from  $0^\circ - 90^\circ$ , changing direction in time. In the next figures (time instances) these preferential flow directions have been changed. The most frequent and rapid motions can be seen towards the west with flow speeds exceeding velocities of  $0.1 \text{ km s}^{-1}$ .

### Decaying stage

The final stage of each sunspot comprises the decaying state. In the previous chapters, we have already outlined the formation and evolution of the sunspots and established a strong connection between the emergence of plasma and the evolution of the emerging magnetic field. Nevertheless, to get an improved understanding of the physical processes governing the evolution of sunspots, one has to include the study of their decay phase and establish if there is some connection with the magnetic field dissipation or not. On the other hand, understanding the formation and decay processes is important for models of magnetic flux transport to the surface ([Schrijver, 2001];[Wang et al., 2002]). Once the magnetic field of an active region has emerged to the surface and the region has reached its maximum superficial extension and thus its maximum development, the decaying phase starts. There are several models that seek to explain and give a reason for the lifetimes of sunspots. For example, given the size and photospheric conductivity, if purely ohmic dissipation is assumed, sunspots would have lifetimes of about 300 years [Cowling, 1946]. Obviously it is necessary to think about other physical processes which can dissipate the magnetic field on much smaller time scales. Different mechanisms trying to explain the decay of sunspots have been proposed including turbulent diffusion ([Krause and Ruediger, 1975]) or submergence ([Howard, 1992]; [Kálmán, 2001]). A vast majority of the sunspots that begin to decay (featuring a decreasing magnetic flux and area) are surrounded by so-called “moat cells” or ”moat flows”, which will be described in more detail in Chapter 5.

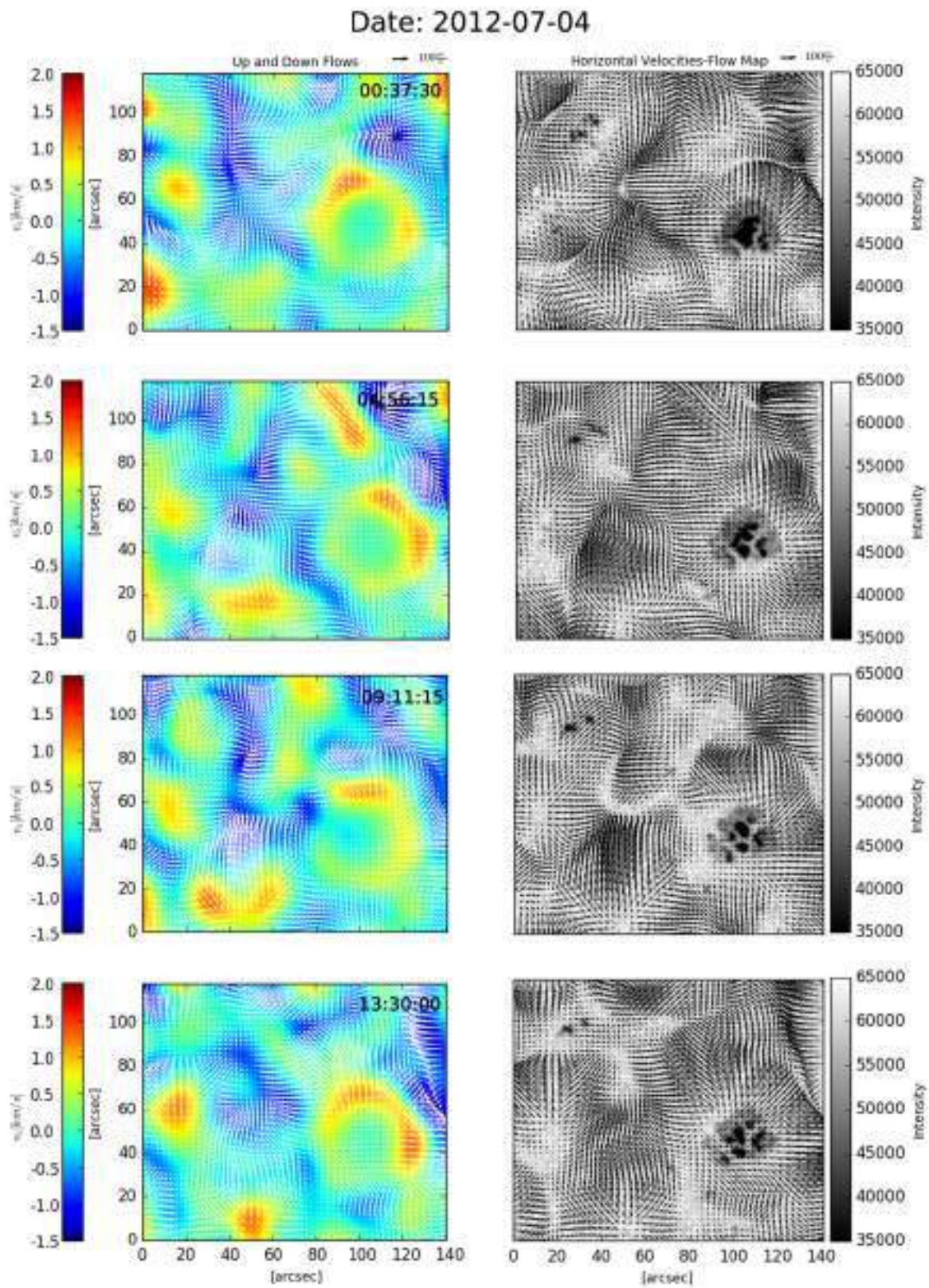
Focusing on the decay of sunspots, the goal here is to shed more light on the involved physical processes by analysing data taken from AR 1517 throughout the day 04-07-2012. During this time period it is possible to evidence the decay of the active region, although it is not enough to study the total disappearance of the active region, since, when it gets closer to the limb, the LCT algorithm becomes unreliable as previously commented. Figure (4-26) shows how the amount of magnetic flux changes and decays during the evolving day. In the continuum intensity images one can see how the pores in the demarcated ROI (red square) are at that stage almost gone while the pores within the green box start to disappear.

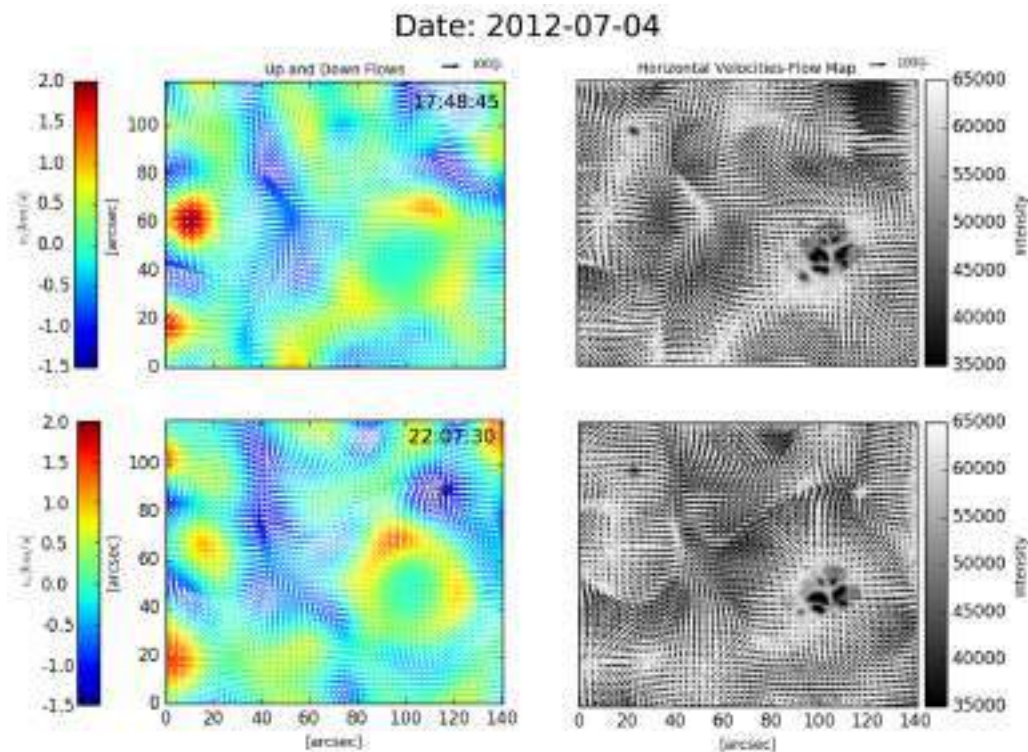
Magnetograms clipped in the range [-500,500] Gauss. The enclosed sunspot (within the cyan box taken in the intensity image) decays too. The penumbra becomes weaker and its area is decaying. The magnetic region with stronger magnetic fields, and thus containing more magnetic flux, survives longer than the pores which already disappeared (or being close to disappearance) at the end of this day.



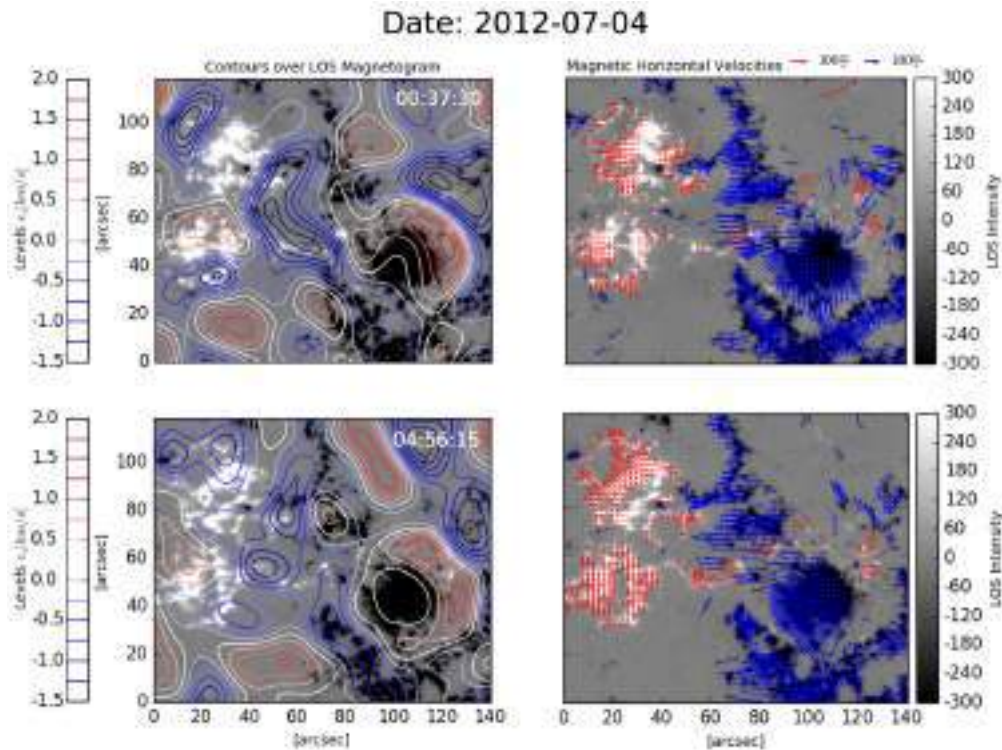
**Figure 4-26.**: Comparison between the early stage of the sunspot at 2012-07-04 and decaying phase, the same day.

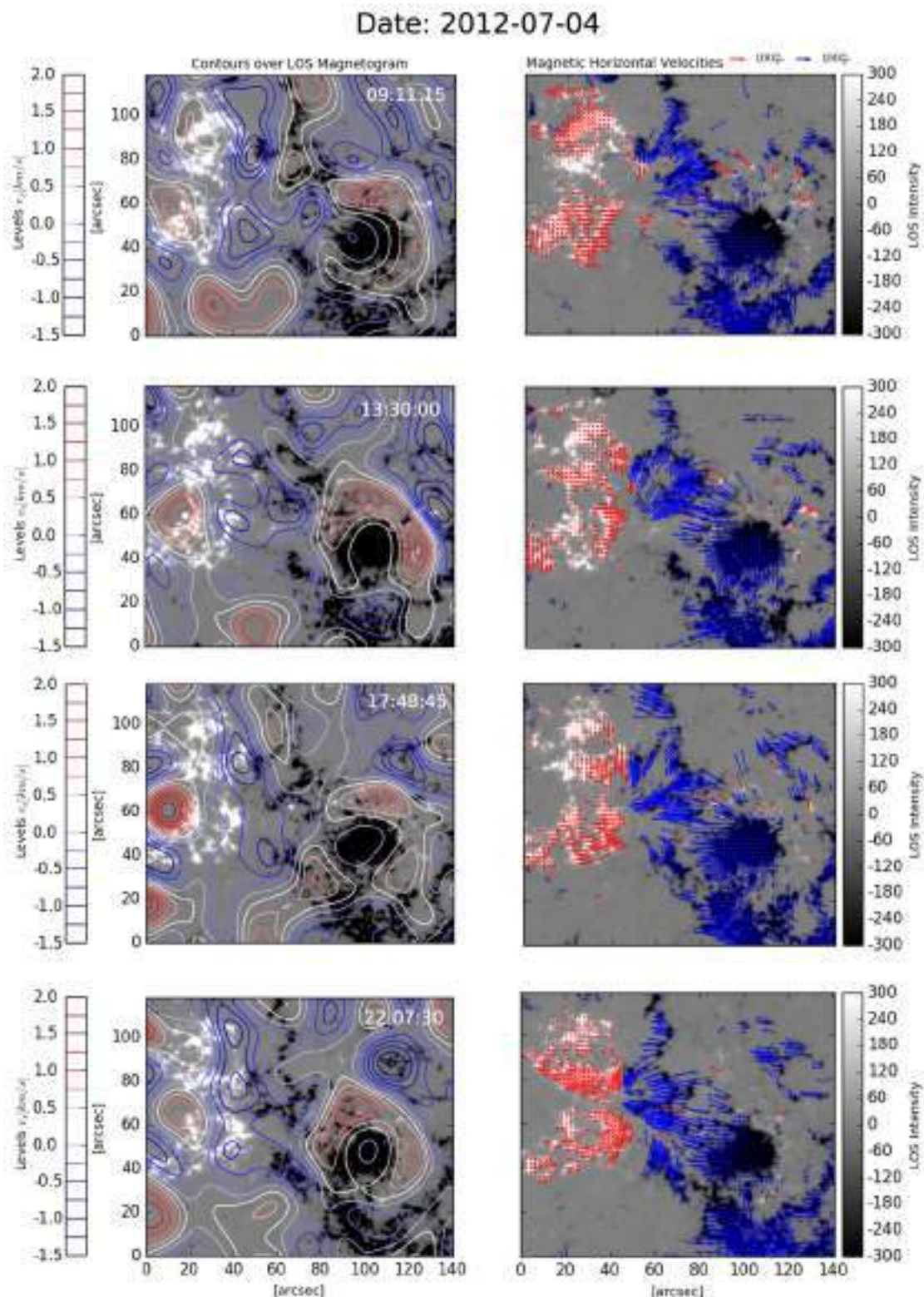
There are two basic ways for sunspots to decay: fragmentation and gradual decay. The pores on the right region show a fragmentation, maybe caused by the strong upward plasma emerging in the middle of the pores as shown in Fig. (4-27), whereas the main sunspot in this AR shows a gradual decay. In the case of the sunspot, the reduction in field strength and area could be originating from upward and downward plasma motions that enclose the sunspot, forcing the magnetic flux tubes, initially encapsulated within the umbra, to be transported through the penumbra (in a way, they are torn out of the sunspot) and thus at the end producing a diminishing of its area ([Cowling, 1946]).



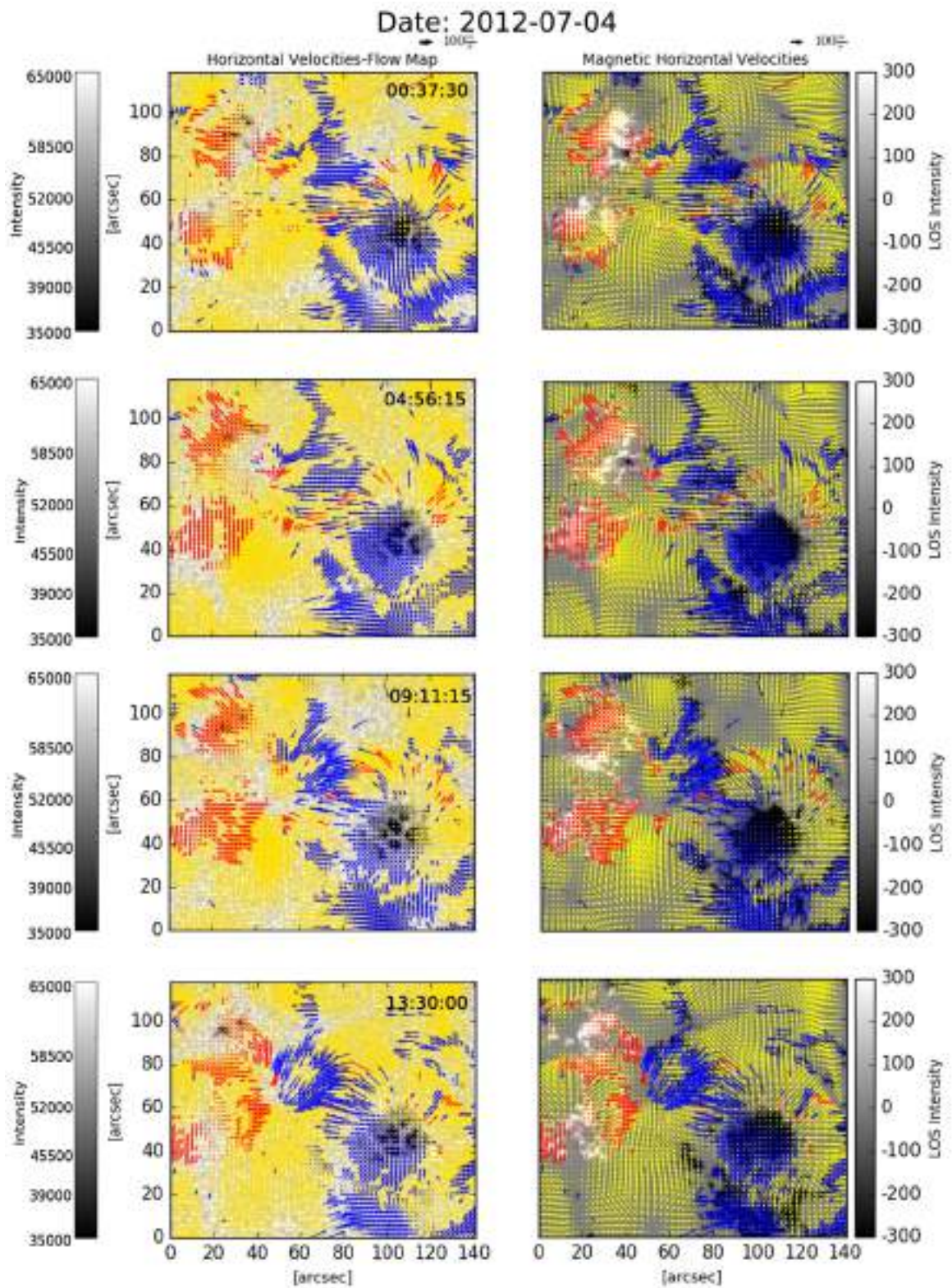


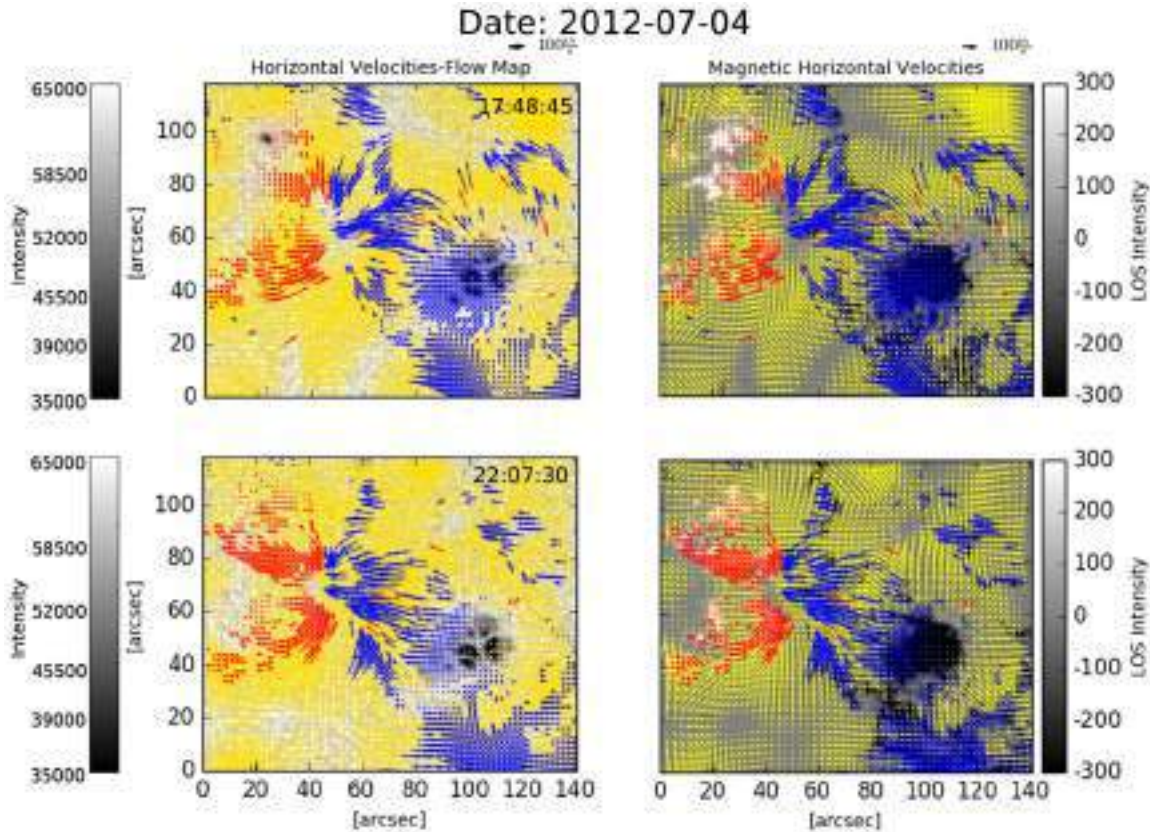
**Figure 4-27.:** Horizontal and vertical velocities for the decaying phase of AR 1517 on 2012-07-04 from 00:37:30 to 22:07:30 UT. The description for the figures is the same as in Fig. (4-9).





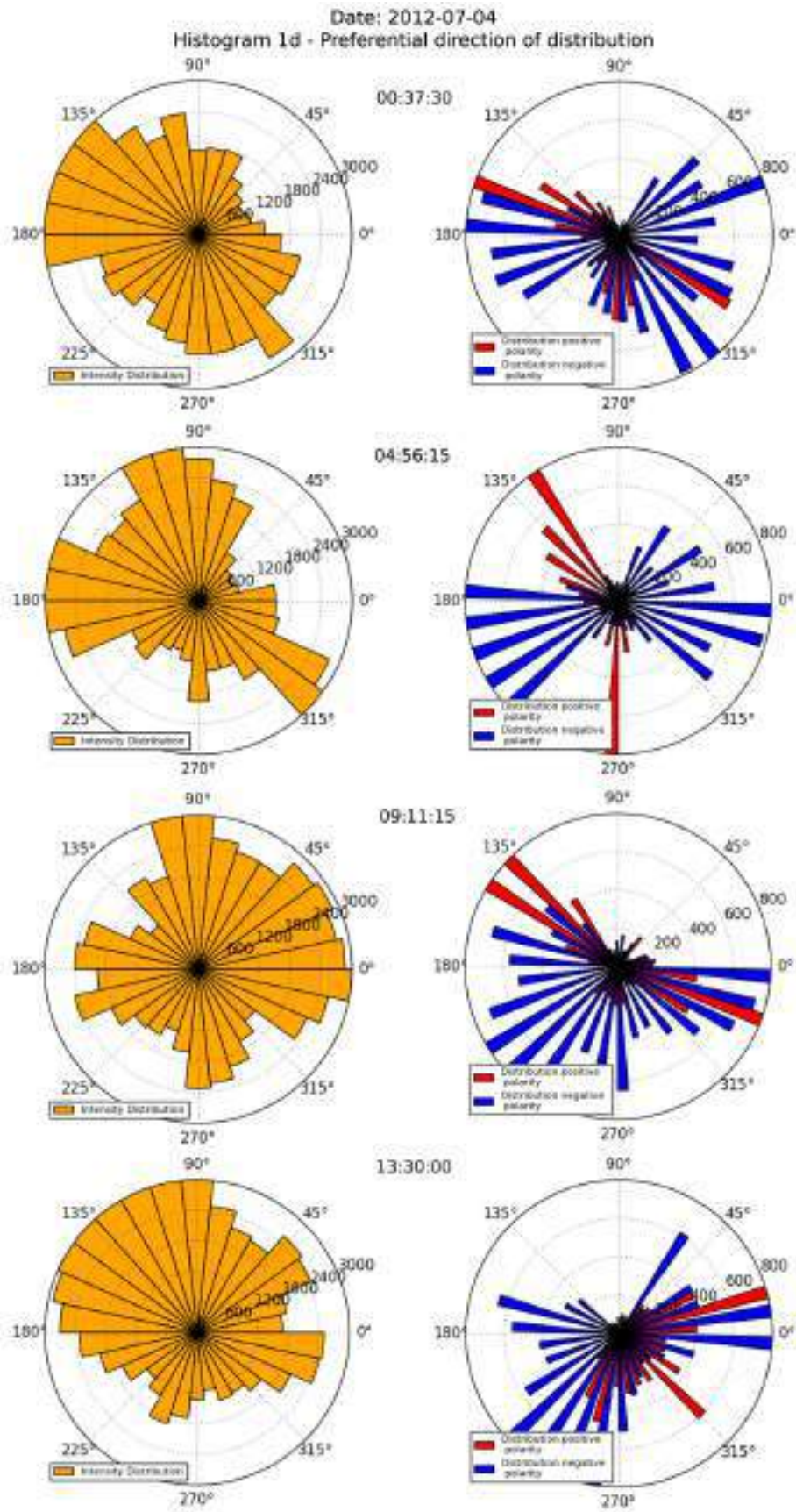
**Figure 4-28.:** Contours obtained from vertical velocities and horizontal proper motions obtained from LOS magnetic fields similar to Fig. (4-11), but for 2012-07-04 from 00:37:30 to 22:07:30 UT.

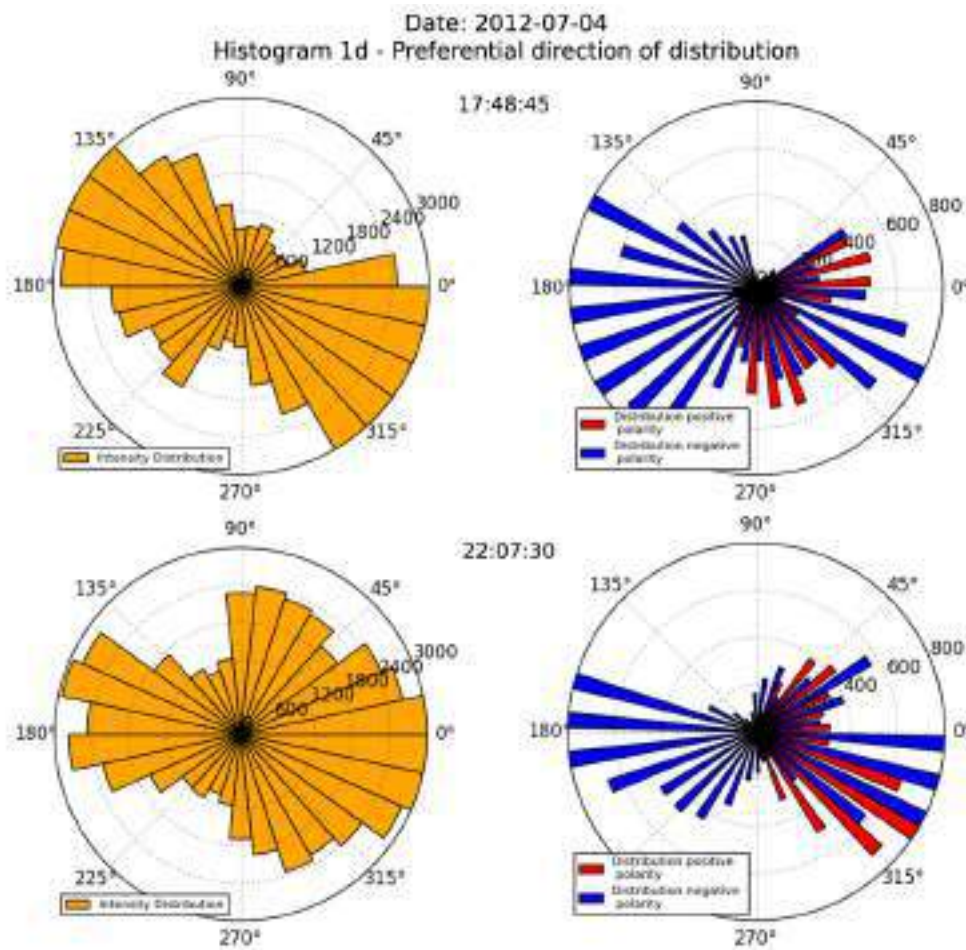




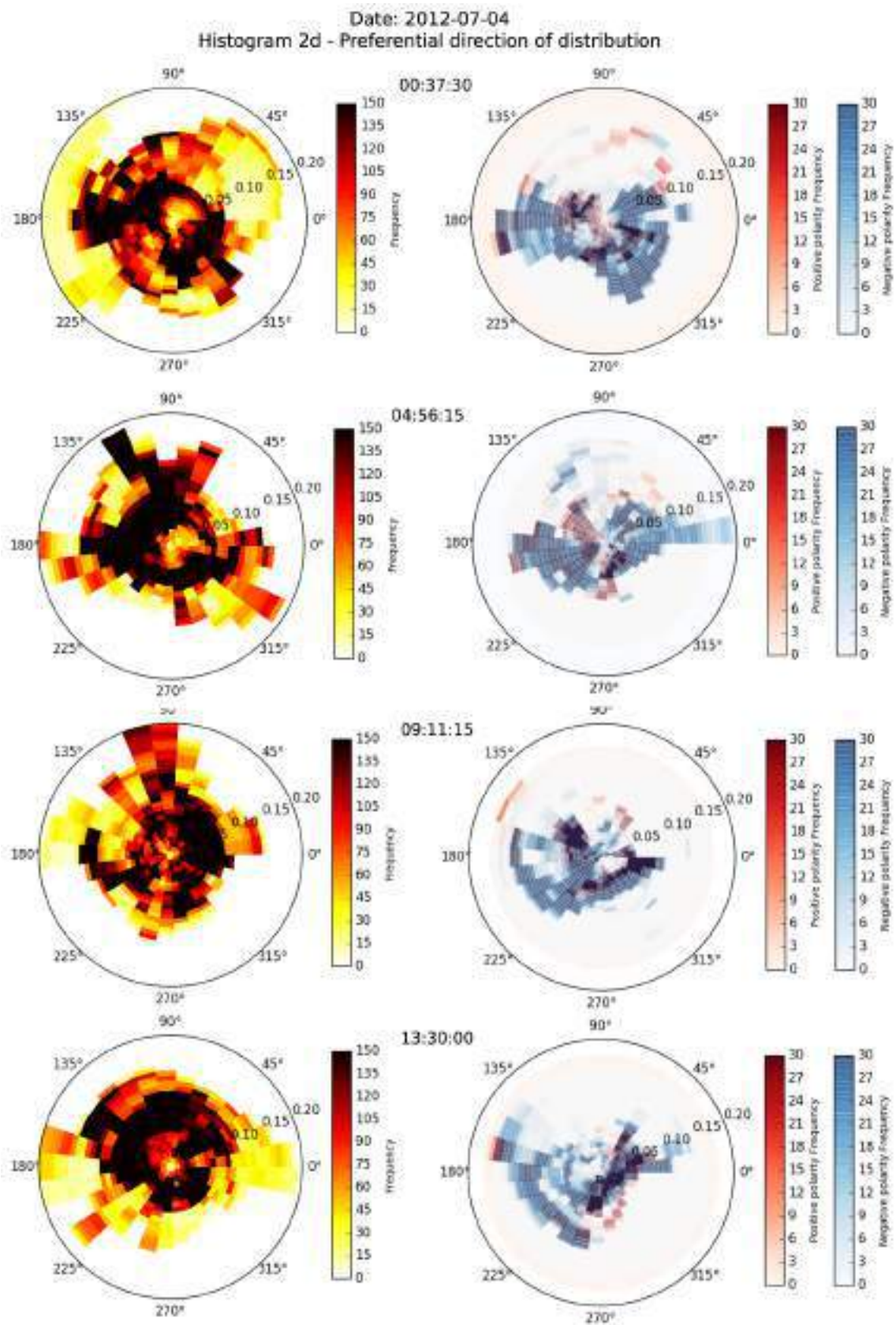
**Figure 4-29.:** The figures show a composition of vector field velocities for the plasma displacements (yellow sectors) and magnetic polarities proper motions (red arrows: positive polarity; blue arrows: negative polarity) for time: 2012-07-04 from 00:37:30 to 22:07:30 UT.

Figure (4-29) depicts the interaction between the plasma as well as the magnetic elements and the preferential direction of both, the plasma flows and the horizontal magnetic displacements. It is possible to identify a preferential direction in the composition of horizontal velocity fields and the histograms of the negative magnetic elements (see Figs. 4-30, 4-31). The identified preferential motion points to the direction of the left-bottom corner and directed into the direction of the sink, detected in the vertical velocity maps, which are centered roughly at the coordinates ( $x = 40, y = 60$ ) arcsec. The 1-D polar histograms show the diminishing of the positive elements; the preferential direction as indicated by the plasma flows (continuum intensity velocity maps) is similar to the motions shown by the positive elements. The 2-D histograms give us some additional clues, namely that the plasma is moving in the horizontal direction faster than the corresponding magnetic field elements. Besides, the fastest flow direction is towards the upper-left corner.





**Figure 4-30.**: 1-D histograms showing the preferential directions for displacements after AR 1517 started to decay at 2012-07-04 from 00:37:30 to 22:07:30 UT.



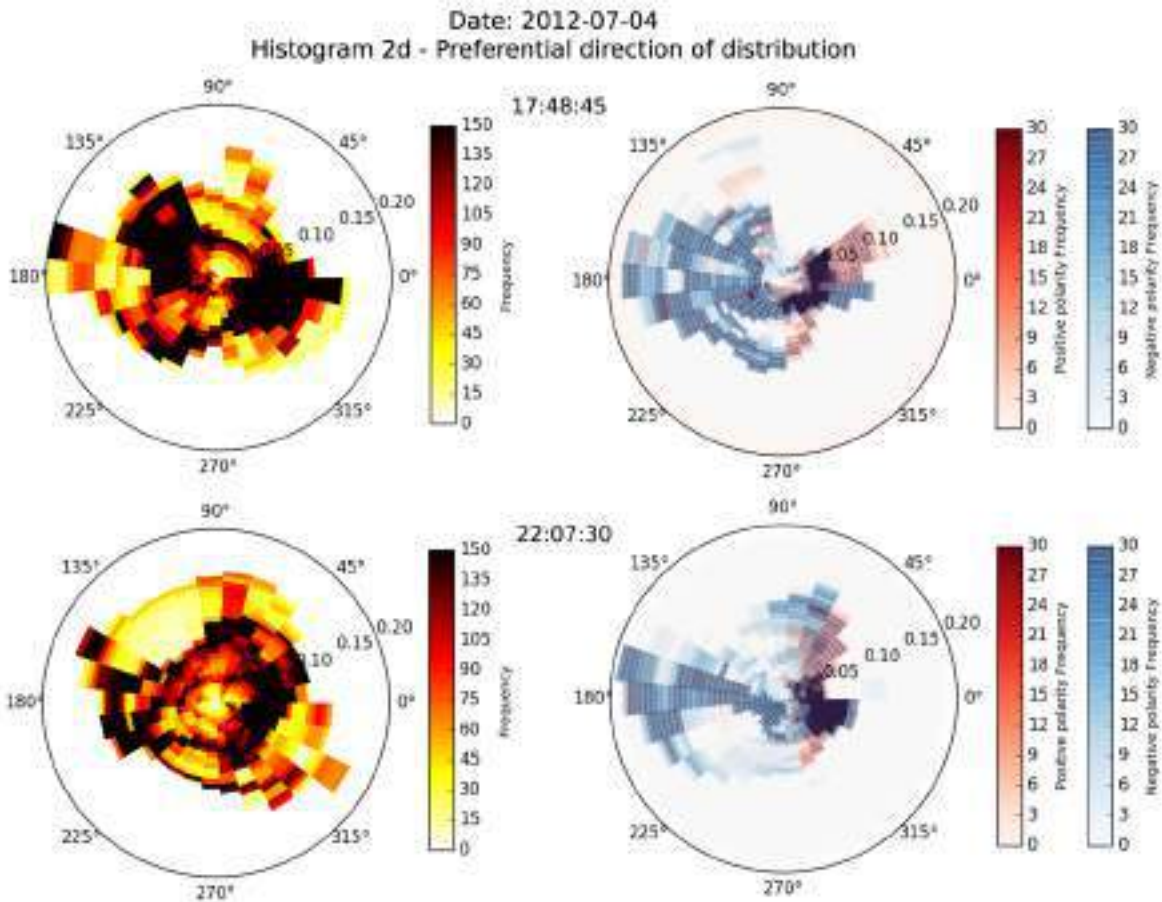


**Figure 4-31.:** 2-D histograms showing the preferential directions for displacements after AR 1517 started to decay at 2012-07-04 from 00:37:30 to 22:07:30 UT.

## Emergence and pore formation in AR 1190

In contrast to the previous analyzed emergence of AR 1517, this active region does not exhibit strong changes in the continuum intensity. However the exploding granule can be clearly observed in the evolution of the LOS magnetogram (see Fig.(4-32)).

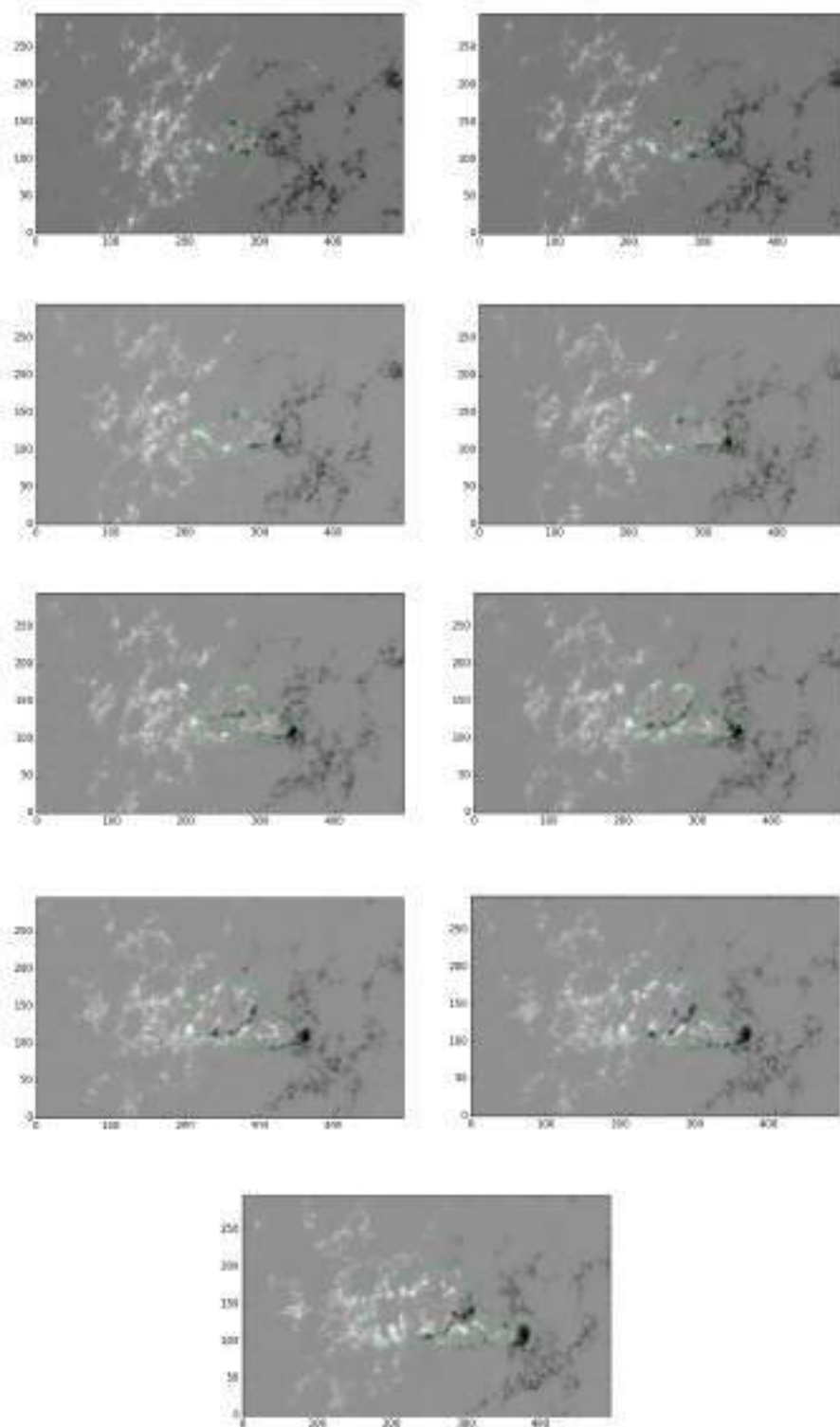


**Figure 4-32.:** Time evolution of exploding mesogranule in AR 1190. The green contour shows the temporal evolution of the mesogranular magnetic field emergence. One can see how a second emergence appears next to the first one and push it to the right. The axes are in arcsec.

Figures 4-33 and 4-34 illustrate the evolution of a solar pore during the formation and emergence of AR 1190. Similarly as in Fig. (4-9) of Section 4.7.1, Fig. (4-33) shows on the left again the color-coded vertical velocity map in  $\text{km s}^{-1}$  clipped in the range  $[-1.5, 2.0] \text{ km s}^{-1}$ ; the horizontal velocity field is given by the overplotted arrows. The right images display the intensity maps obtained from SDO/HMI; the horizontal velocity field is overplotted. These velocities were calculated over a 15 minutes average and a window size of  $FWHM = 20$  arcsec from intensity images, similarly as in Section 4.7.1. Figure (4-34) shows on the left a LOS magnetogram clipped in the range  $[-300, 300]$  Gauss with an overlapping contour map of vertical velocities acquired from the intensity image data<sup>2</sup>. The color-coded contours show the velocity level in  $\text{km s}^{-1}$ . The right images depicts the same LOS magnetogram with the velocity field estimated with the magnetic field data using the same initial values for the LCT technique.

Positive magnetic fields are represented in red and negative magnetic fields, in blue. The neutral region has been calculated within the  $[\pm 50]$  Gauss, similarly as in Section 4.7.1.

During the whole evolution the emergence of a strong magnetic bubble can be observed as well as its corresponding vertical velocity field. Figures 4-33 and 4-34 show how a second magnetic bubble starts to emerge inside the first one. This one is even stronger than the previous one, pushing out the just previously emerged magnetic field and becoming more important at later stages in its evolution. In the magnetogram one can observe the new positive magnetic elements emerging within the pre-existing negative magnetic elements. The plasma features upward flows through positive regions and downward directed flows through the negative regions.

Although Figs. 4-36 and 4-37 show a preferential flow direction to the right, the distribution of angles shows that there is, in addition, a strong component in the left direction for the positive component. However, this is not true when one inspects the general distribution of angles for all plasma velocities which is rather uniform. On the other hand, although they appear like a uniform distribution of angles, 2D histograms show speeds with greater magnitudes towards the right, solving the puzzle for the increased velocities due to the second upward bubble.

The first emergence does not show high upwards directed vertical speeds on  $v_z$  maps. However, when the second magnetic emergence appears, this picture changes dramatically. We can now observe higher velocities and increases in the velocity of the former emergence. Figures 4-36 and 4-37 show that the preferential direction of the negative polarity is to the right hand side, concluding that the preferential direction of the plasma motions is governed by the emergence of the positive flux on the FOV. The 2-D histograms display the preference mentioned before and shows that the larger magnitudes (higher plasma speeds) follow the same direction as the magnetic elements which is imposed by the magnetic emergence.

---

<sup>2</sup>In total we created here 15 different contour levels to enable a detailed inspection of the data.

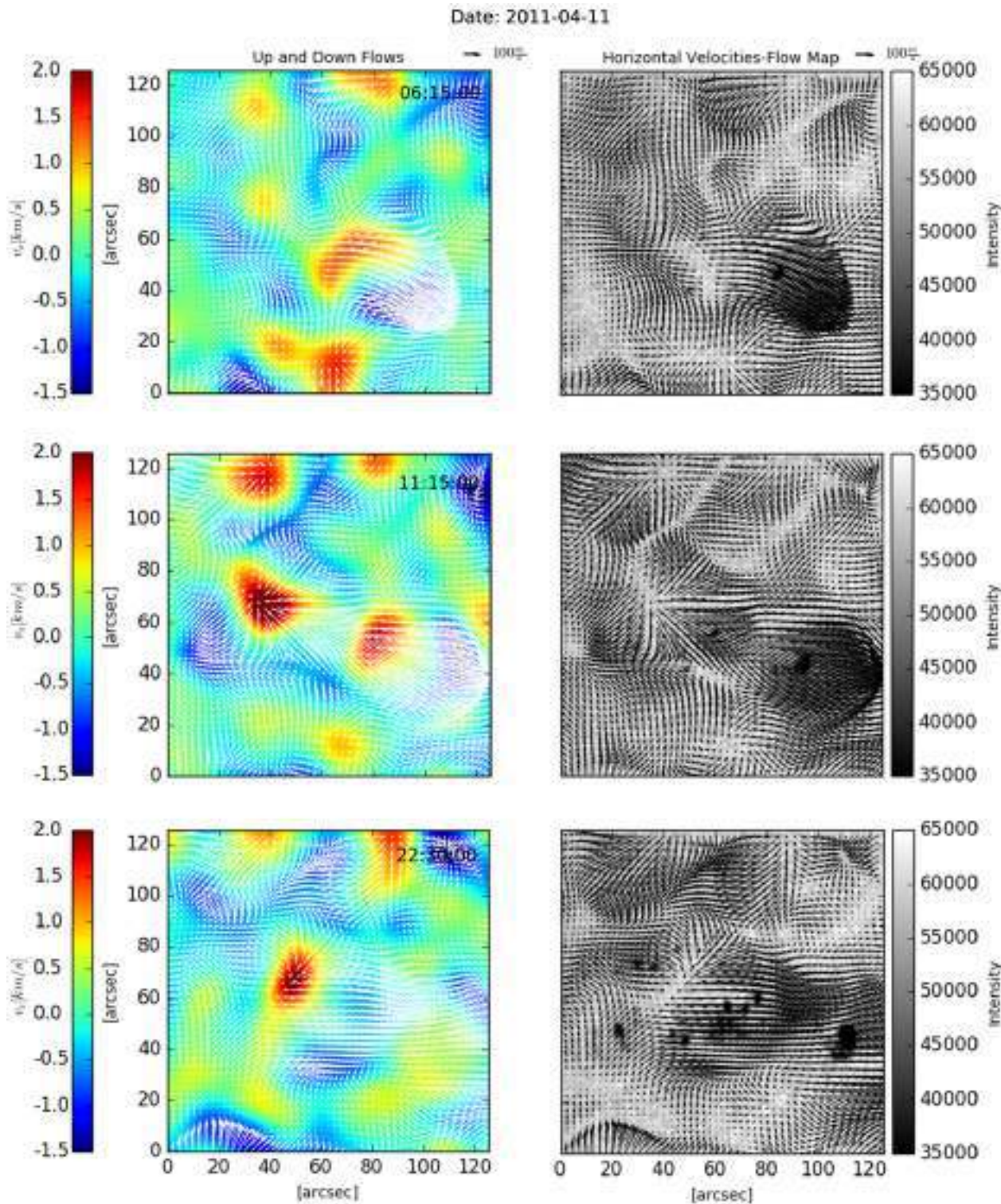


**Figure 4-33.:** Horizontal and vertical velocities during the formation of AR 1190 on 2011-04-11 at 06:15:00, 11:15:00, and 22:30:00. The description is similar as in Section 4.7.1.

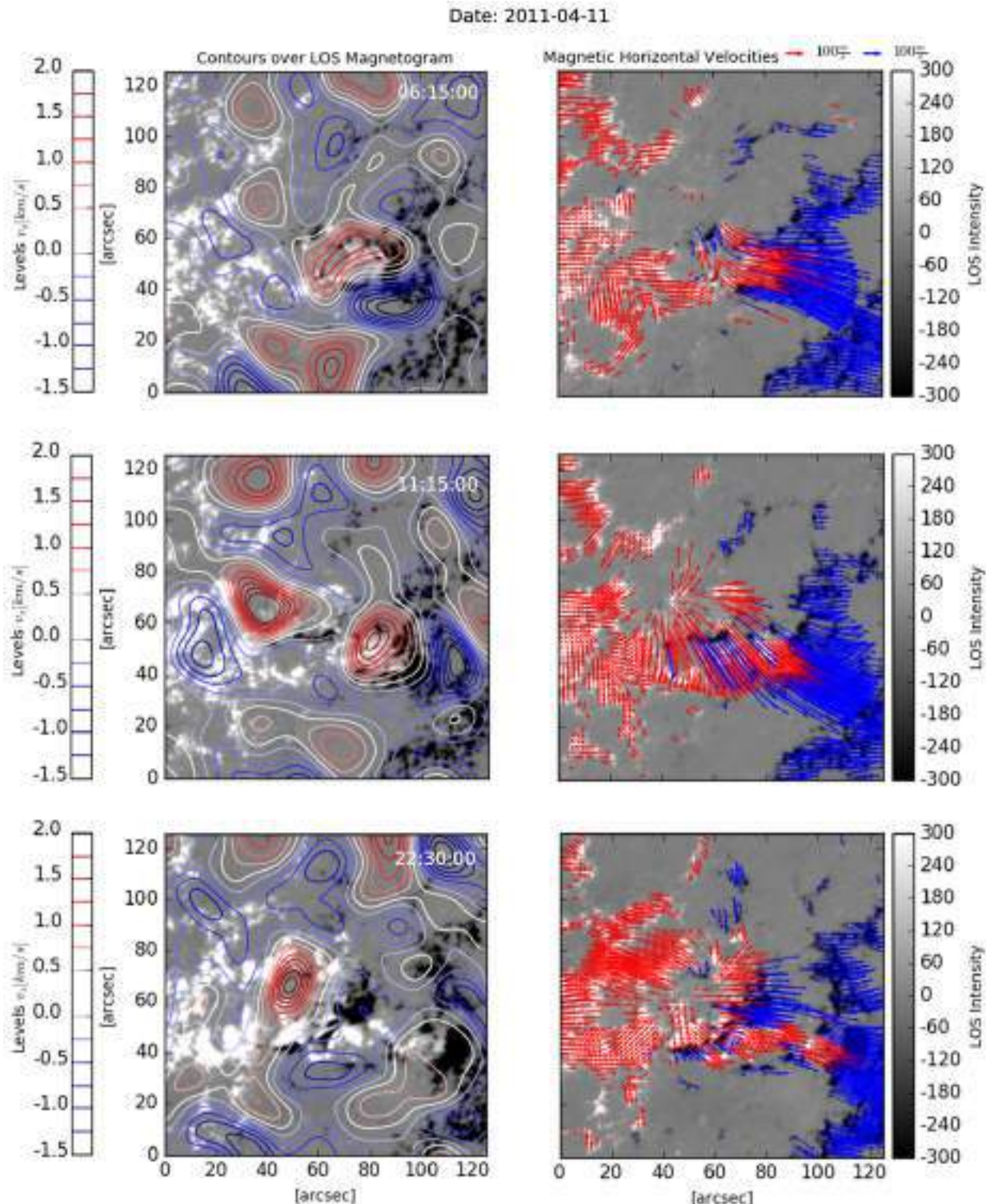


**Figure 4-34.**: Contours obtained from vertical velocities and horizontal proper motions obtained from LOS magnetic fields during the formation of AR 1190 on 2011-04-11 at 06:15:00, 11:15:00, and 22:30:00. The description is similar as in Section 4.7.1.

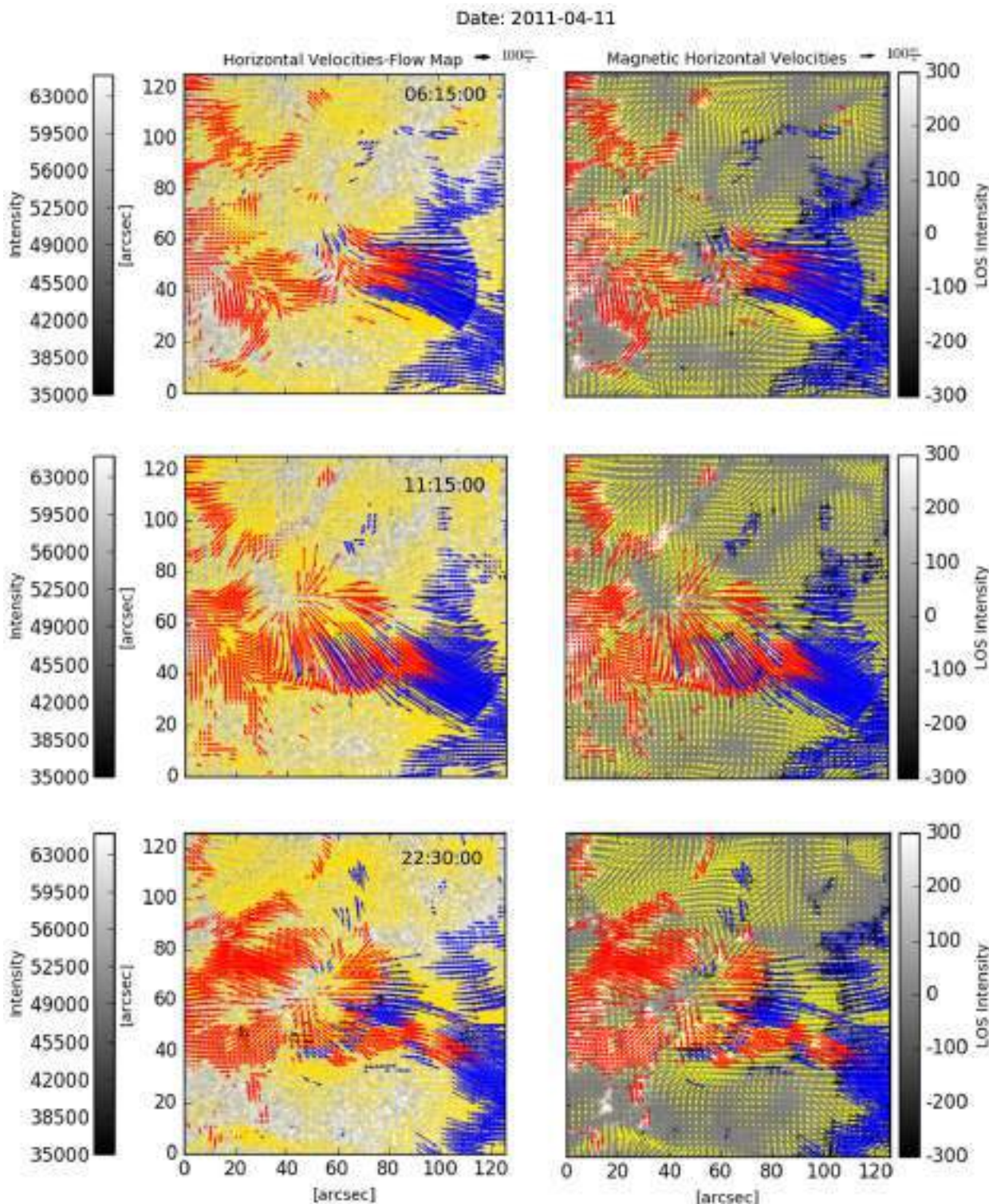


**Figure 4-35.:** The figures show a composition of vectors field velocities for the plasma displacements (yellow sectors) and magnetic polarities proper motions (red arrows: positive polarity; blue arrows: negative polarity) during the formation of AR 1190 on 2011-04-11 at 06:15:00, 11:15:00, and 22:30:00. The description is similar as in Section 4.7.1.

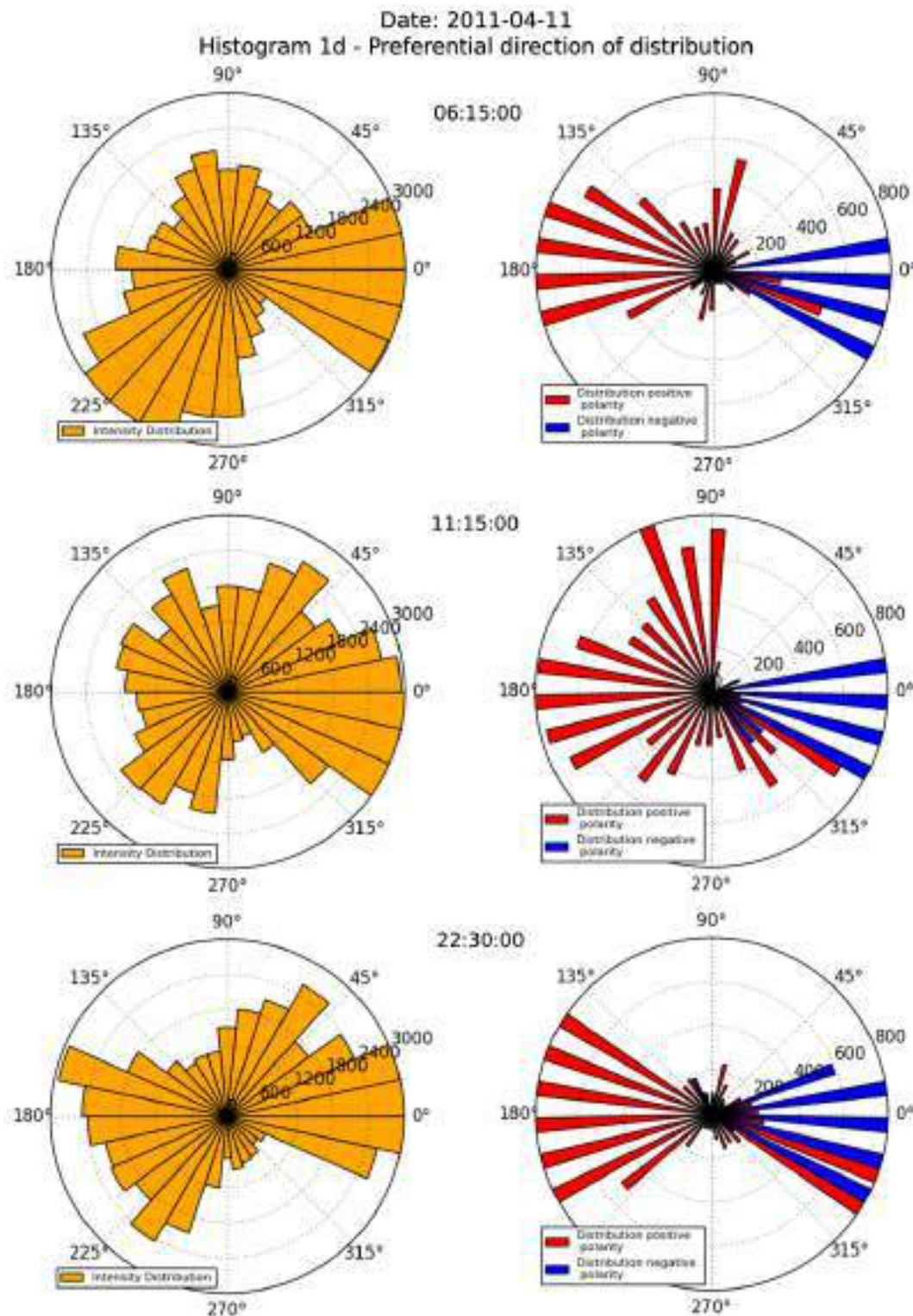


**Figure 4-36.:** 1-D histograms showing the preferential directions for displacements during the formation of AR 1190 on 2011-04-11 at 06:15:00, 11:15:00, and 22:30:00. The description is similar as in Section 4.7.1.

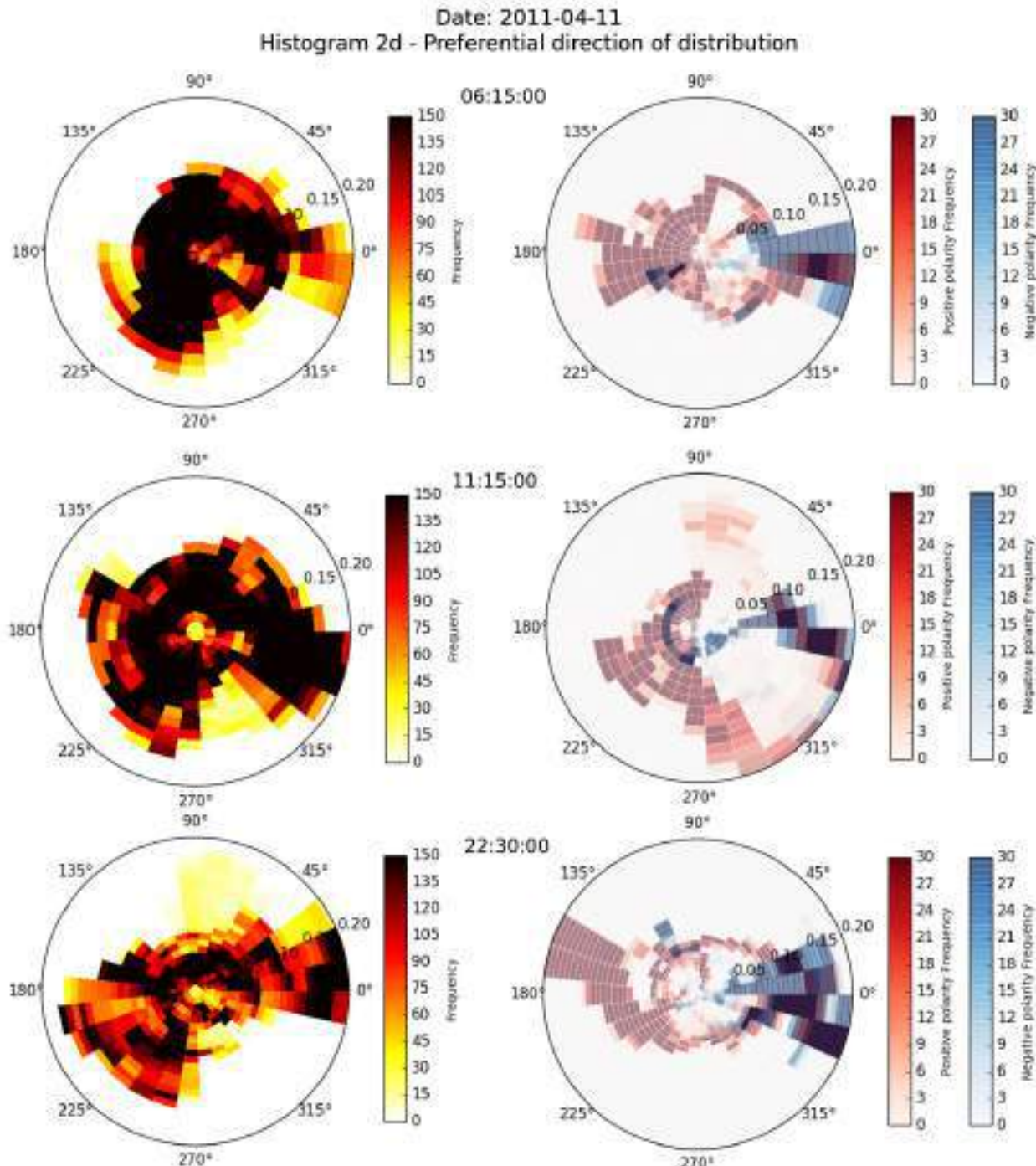


**Figure 4-37.:** 2-D histograms showing the preferential directions for displacements during the formation of AR 1190 on 2011-04-11 at 06:15:00, 11:15:00, and 22:30:00. The description is similar as in Section 4.7.1.

## Emergence and pore formation AR 1762

Following the analysis of AR 1190 and AR 1517, we will compare the emergence of the magnetic bubble with the evolution in the continuum intensity maps. The AR 1762 (Date: 2013-06-01 02:00:00 to 22:00:00), evolves much faster than the previously analyzed ARs. Figures (4-38 & 4-39) show the temporal evolution of the whole region. On the left side the evolution of the LOS magnetic field is shown together with contours outlining the region of flux emergence; the right panel displays the intensity map with the same contour overplotted (contour originating from the magnetogram). Figures 4-40 and 4-41 show three exemplary images for this active region. The region presents faster vertical outward flows during the emergence of positive magnetic field in the center of our FOV. In images that are not shown in this work due to page limiting factors<sup>3</sup>, it can be observed how the AR is emerging very rapidly in comparison with the previous ARs. As it has previously been mentioned, a second region of magnetic field emergence is observed. However, the vertical velocity map in that case shows that the newly emerging flux is expanding horizontally slower than the pre-existing magnetic structure. The preferential motions are along the horizontal directions ( $0^\circ$  and  $180^\circ$ ) during the evolution of the region giving an appearance like that the whole active region is stretching out (see Figs. 4-42, 4-43 and 4-44). Furthermore, it can be that the positive magnetic field is responsible for this behavior due to its large magnetic field strength and its strong velocity magnitude, which is directed in the right direction and thus pushing the plasma in the same direction.

---

<sup>3</sup>All plots and composition of velocity fields are available in the authors's GitHub repository:<https://www.github.com/Hypnus1803>

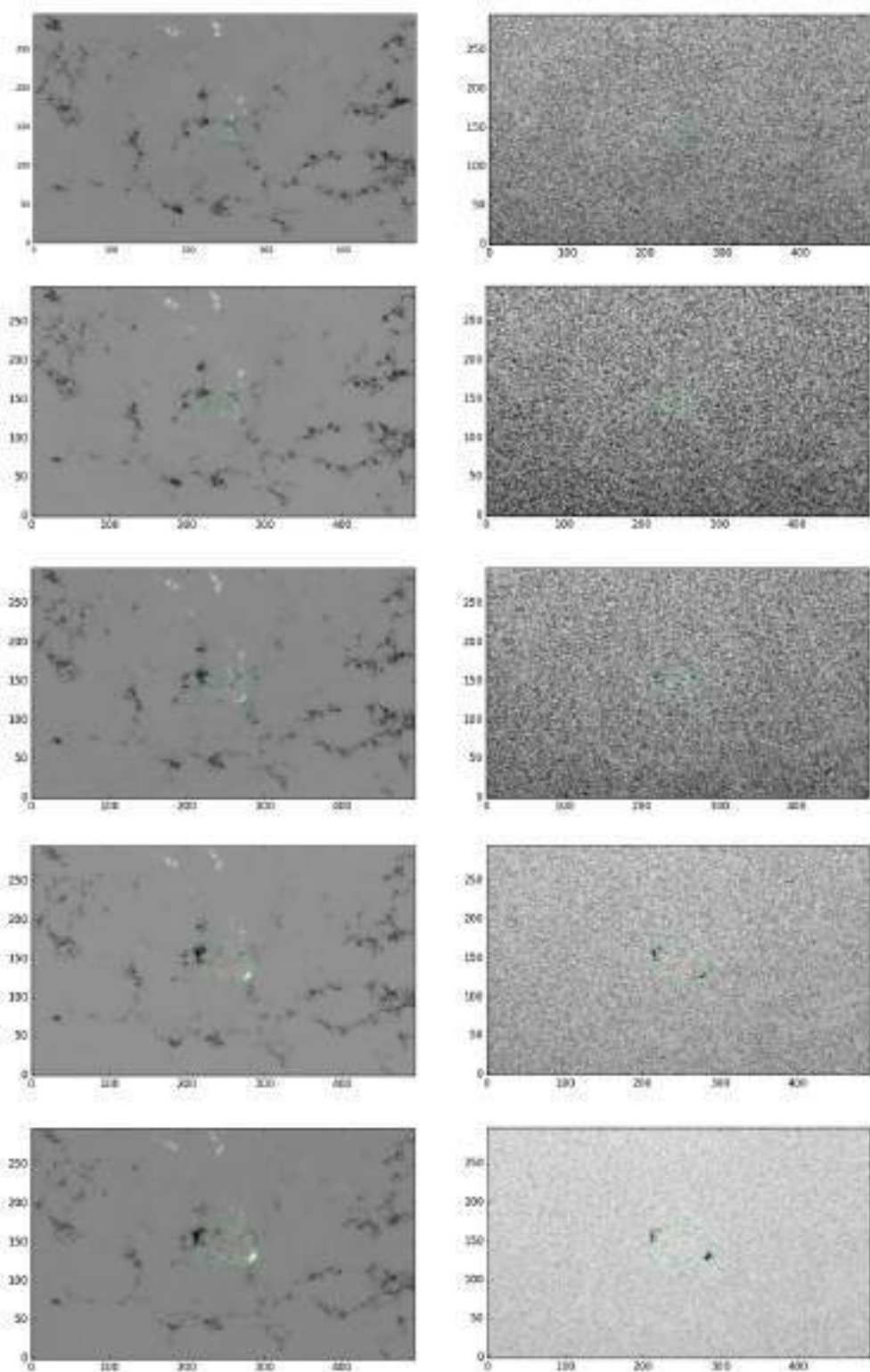


**Figure 4-38.:** Evolution of active region 1762 from 02:00 to 6:00 UT on 01-June-2013. Positive polarity emergence starts to push out the pre-existent magnetic field. The axes are in arcsec.

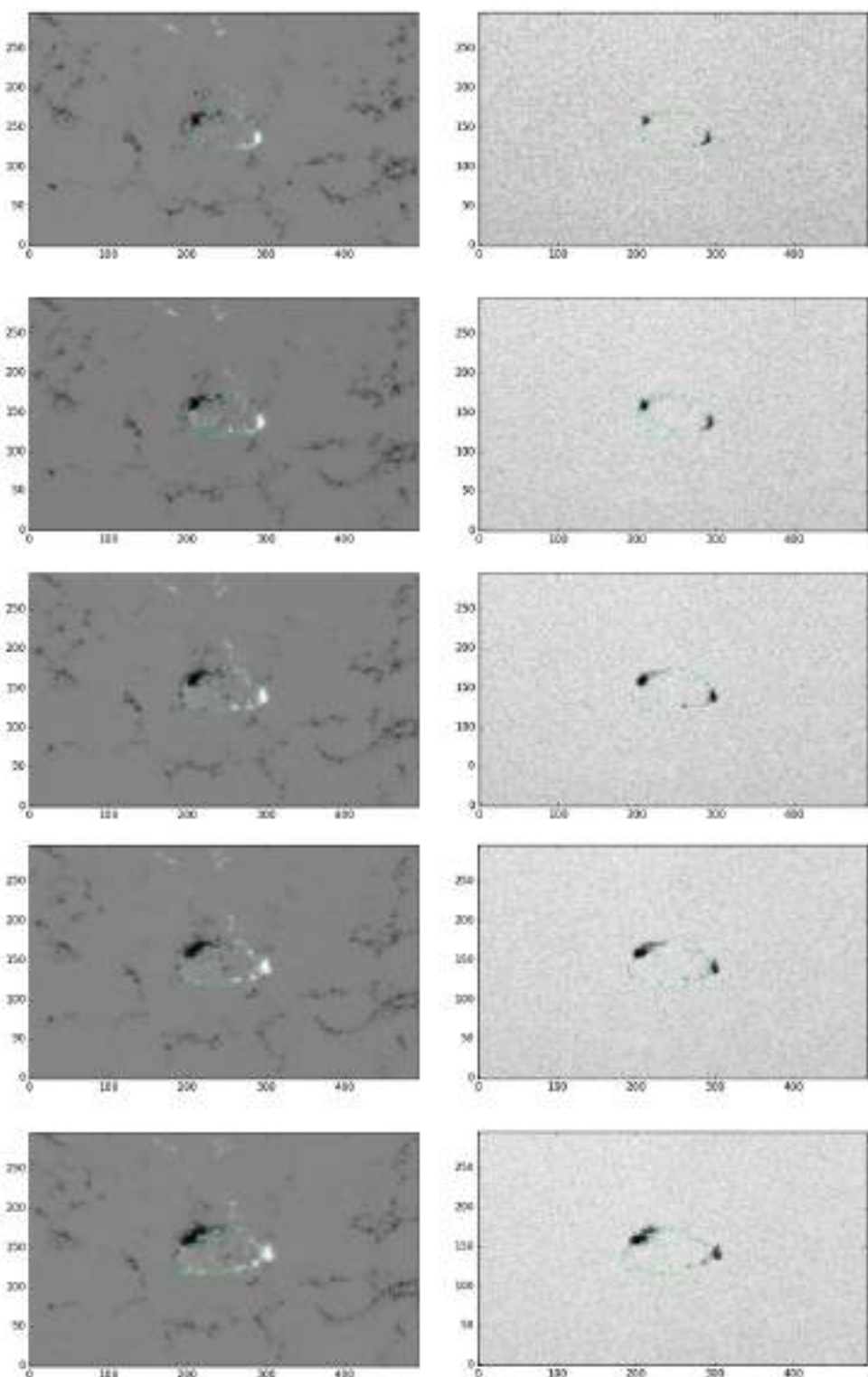


**Figure 4-39.:** Evolution of active region 1762 from 07:00 to 11:00 UT for the same day. A new and different magnetic bubble emerges within the left side of the old emergence. The axes are in arcsec.

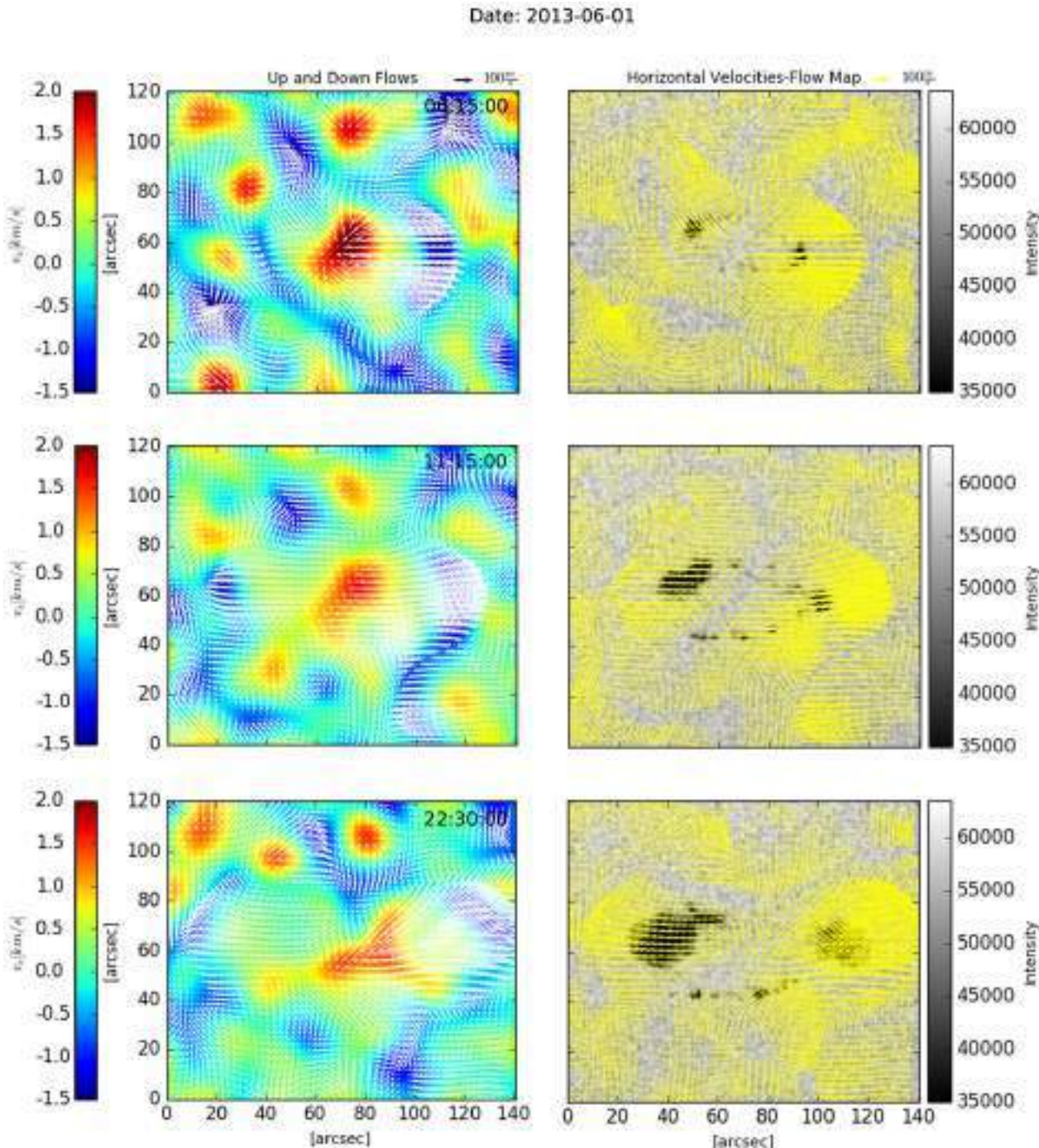


**Figure 4-40.:** Horizontal and vertical velocities during the formation of AR 1762 on 2013-06-01 at 06:15:00, 11:15:00, and 22:30:00. The description is similar as in Section 4.7.1.

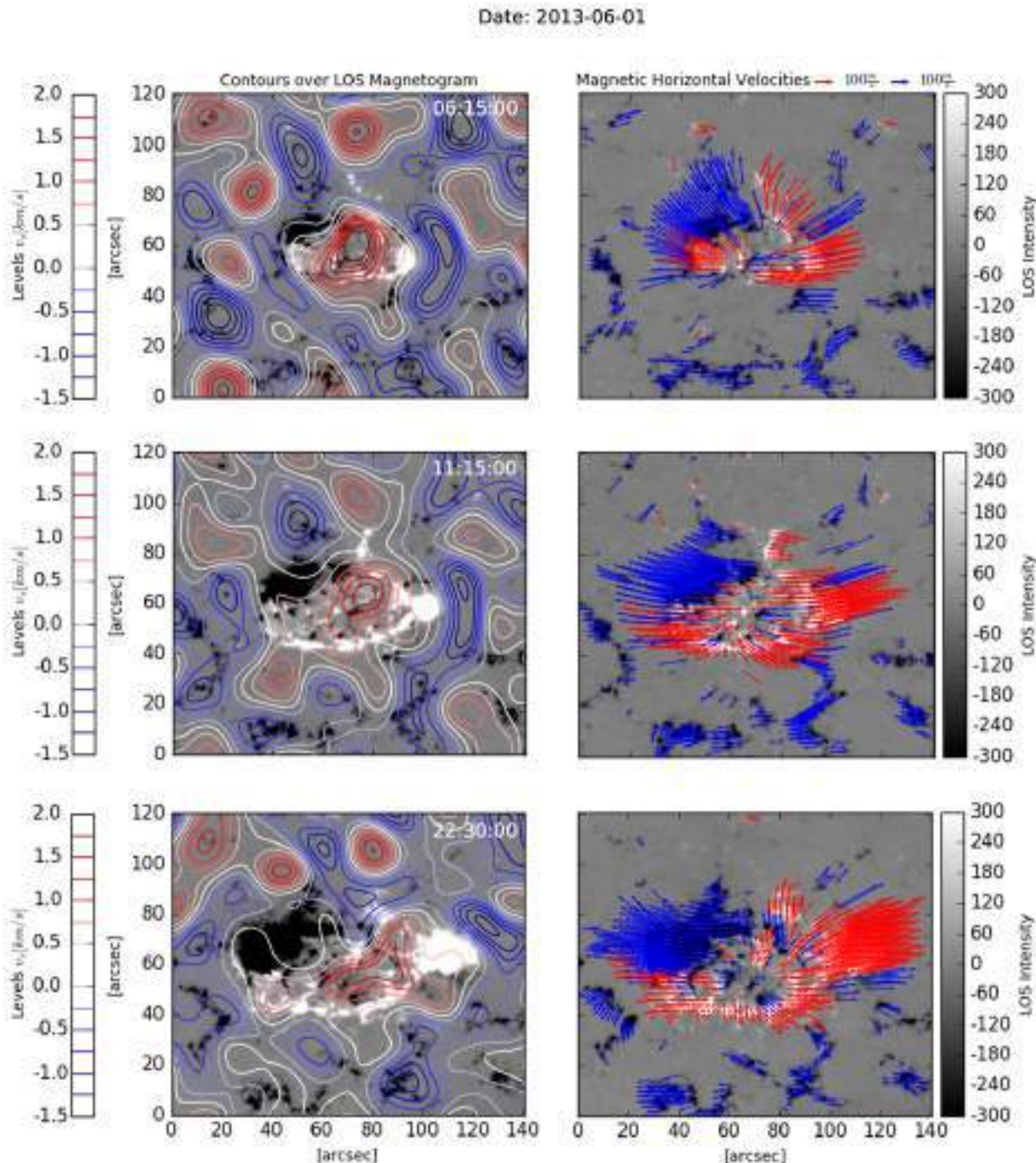


**Figure 4-41.:** Contours obtained from vertical velocities and horizontal proper motions obtained from LOS magnetic fields during the formation of AR 1762 on 2013-06-01 at 06:15:00, 11:15:00, and 22:30:00. The description is similar as in Section 4.7.1.

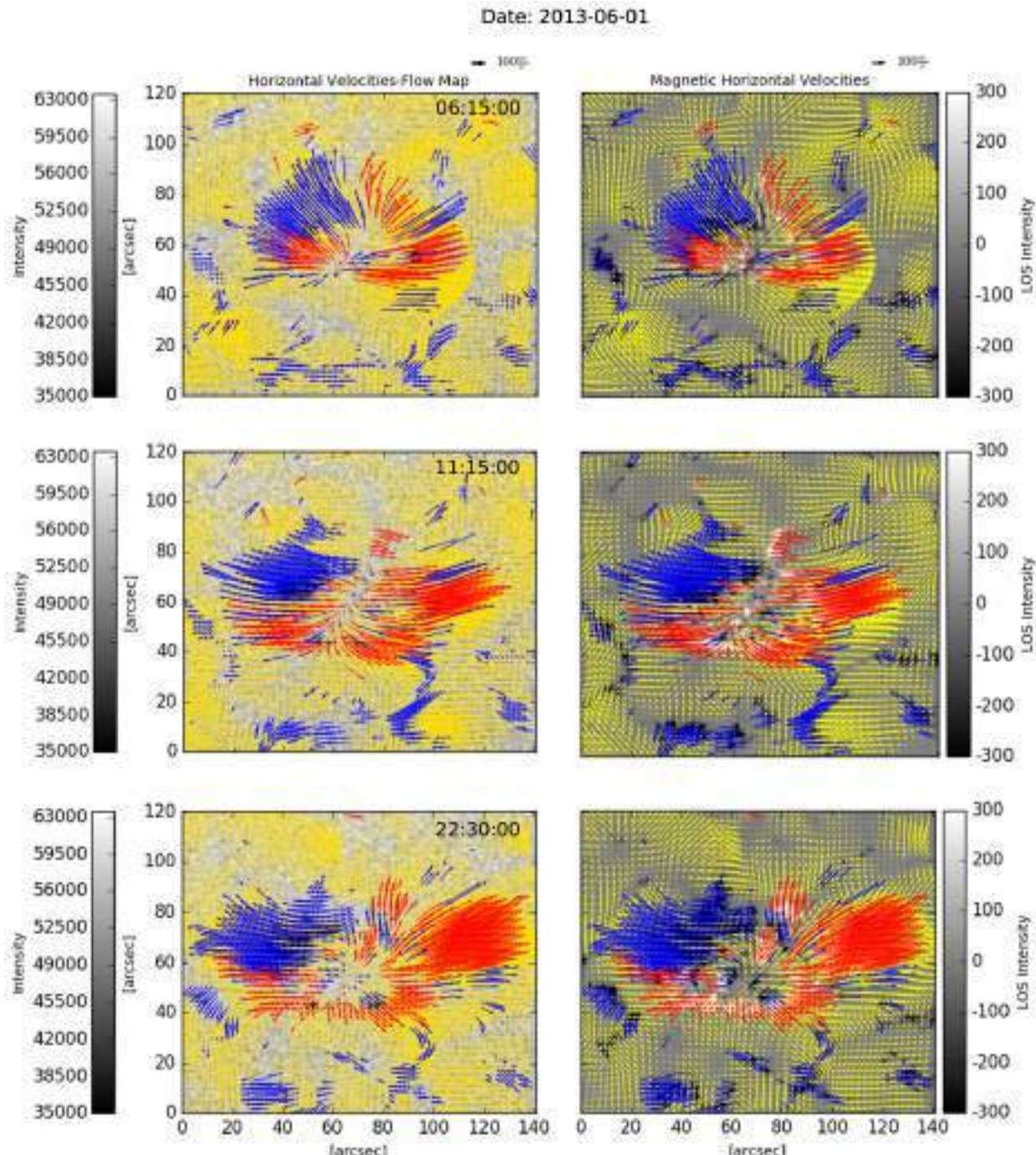


**Figure 4-42.**: The figures shows a composition of vector field velocities for the plasma displacements (yellow sectors) and magnetic polarities proper motions (red arrows: positive polarity; blue arrows: negative polarity) during the formation of AR 1762 on 2013-06-01 at 06:15:00, 11:15:00, and 22:30:00. The description is similar as in Section 4.7.1.

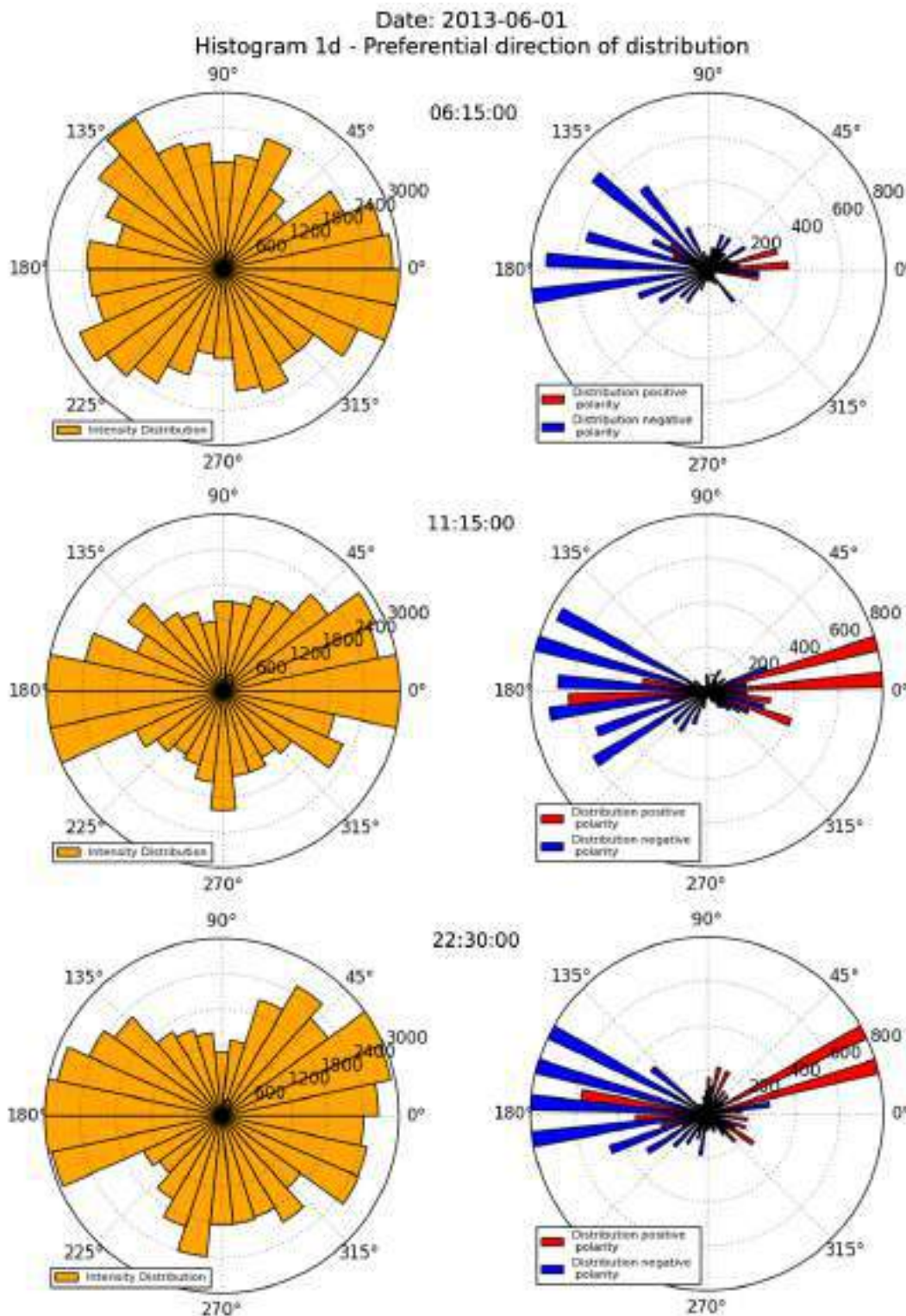


**Figure 4-43.: 1-D histograms showing the preferential directions for displacements during the formation of AR 1762 on 2013-06-01 at 06:15:00, 11:15:00, and 22:30:00. The description is similar as in Section 4.7.1.**

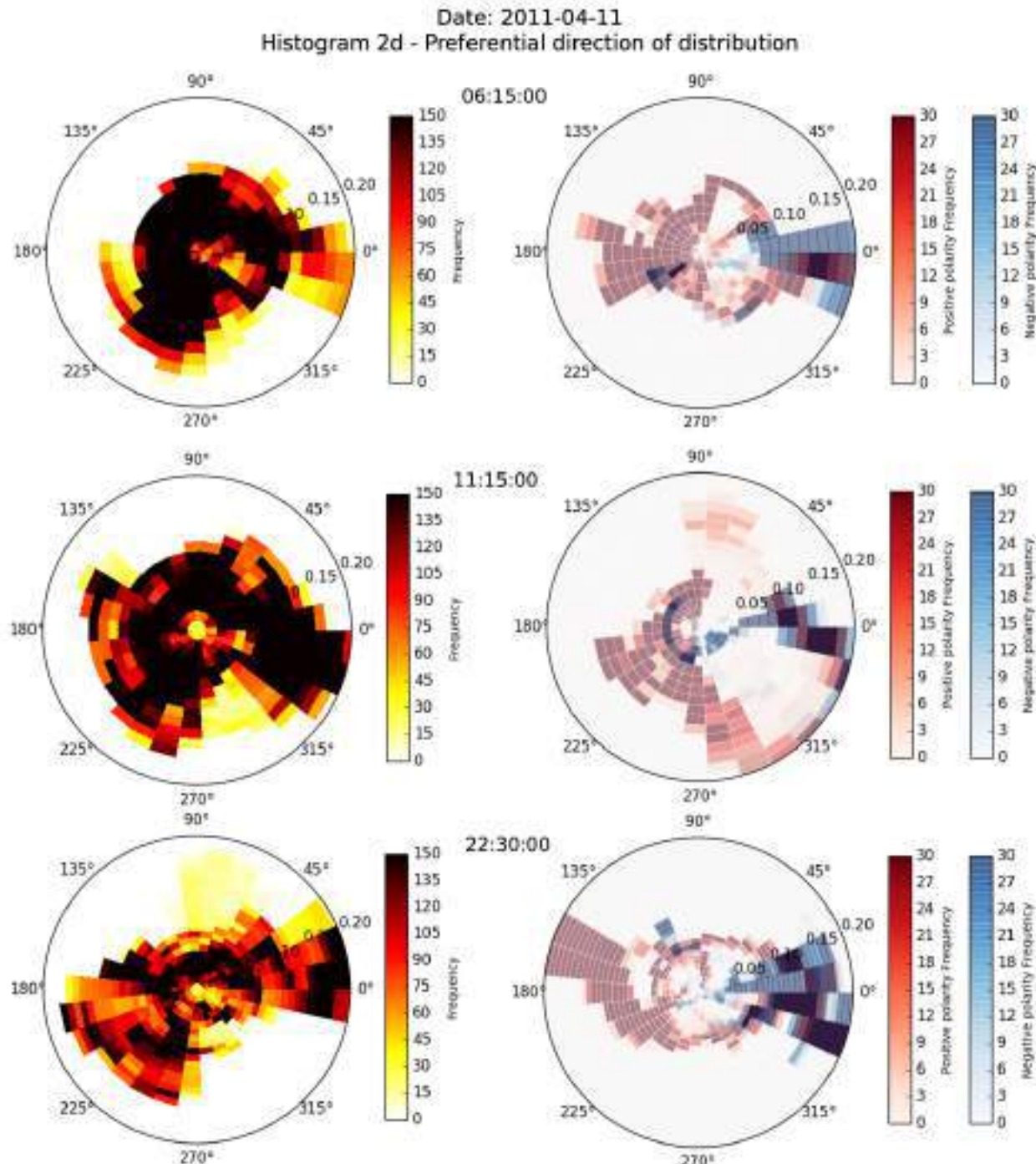


**Figure 4-44.**: 2-D histograms showing the preferential directions for displacements during the formation of AR 1762 on 2013-06-01 at 06:15:00, 11:15:00, and 22:30:00. The description is similar as in Section 4.7.1.

# 5. Identification of Moat Flows around Sunspots

## 5.1. Introduction

When a sunspot reaches its maximum development and all the magnetic flux has emerged to the solar surface, its penumbra reaches also a mature stage around it. The penumbra is usually surrounded by an annular region, that is referred to as the “moat cell” or “moat flows”. This ringed region normally shows plasma flows radially directed away from the sunspot. This chapter will be dedicated to the study of these “moat flows”. Moat flows have usually been directly related with the penumbra of sunspots and were firstly detected by [Sheeley, 1969]. The existence of moat flows could be linked to the existence or non-existence of the penumbra. Several authors argue that the existence of a penumbra is not a prerequisite to form moat flows near the umbra ([Deng et al., 2007]; [Verma et al., 2012]; [Balthasar, 2013]). On the other hand, [Vargas Domínguez, 2008] concluded that moat flows can only be found around sunspots which have an entirely developed penumbra. It is believed that the shape of the moat cells depends on the magnetic environment. The size of the moat is within the range of 10 to 20 Mm or even up to the supergranular size. This chapter is motivated by the results obtained in [Vargas Domínguez, 2009]. An analysis will be done for a sample of sunspots which have not a fully developed penumbra around the umbra.

## 5.2. Observations and Data

Using the Helioviewer GUI [ESA, 2016] an exhaustive search through five years of observationally data obtained between 2011 and 2015 has been performed. The selection criterion for our data was that the chosen sunspots do not show a full penumbra around the umbra. A continuum intensity data set has been used from SDO/HMI and within this chapter we will focus on three selected regions for our analysis. As previously explained in section 3.2, the images have been rotated considering the instrument and satellite position using the rotation function within Scipy libraries. The p-mode filtering has also been applied to the time series, using a threshold of  $4 \text{ km s}^{-1}$ . We will focus on AR 1517 described in the previous section and extend the study to ARs 1676 (on Feb 22, 2013) and 1176 (on March 27, 2011) shown in Fig. 5-1), to be able to compare the results with the ones obtained by [Strecker et al., 2015].

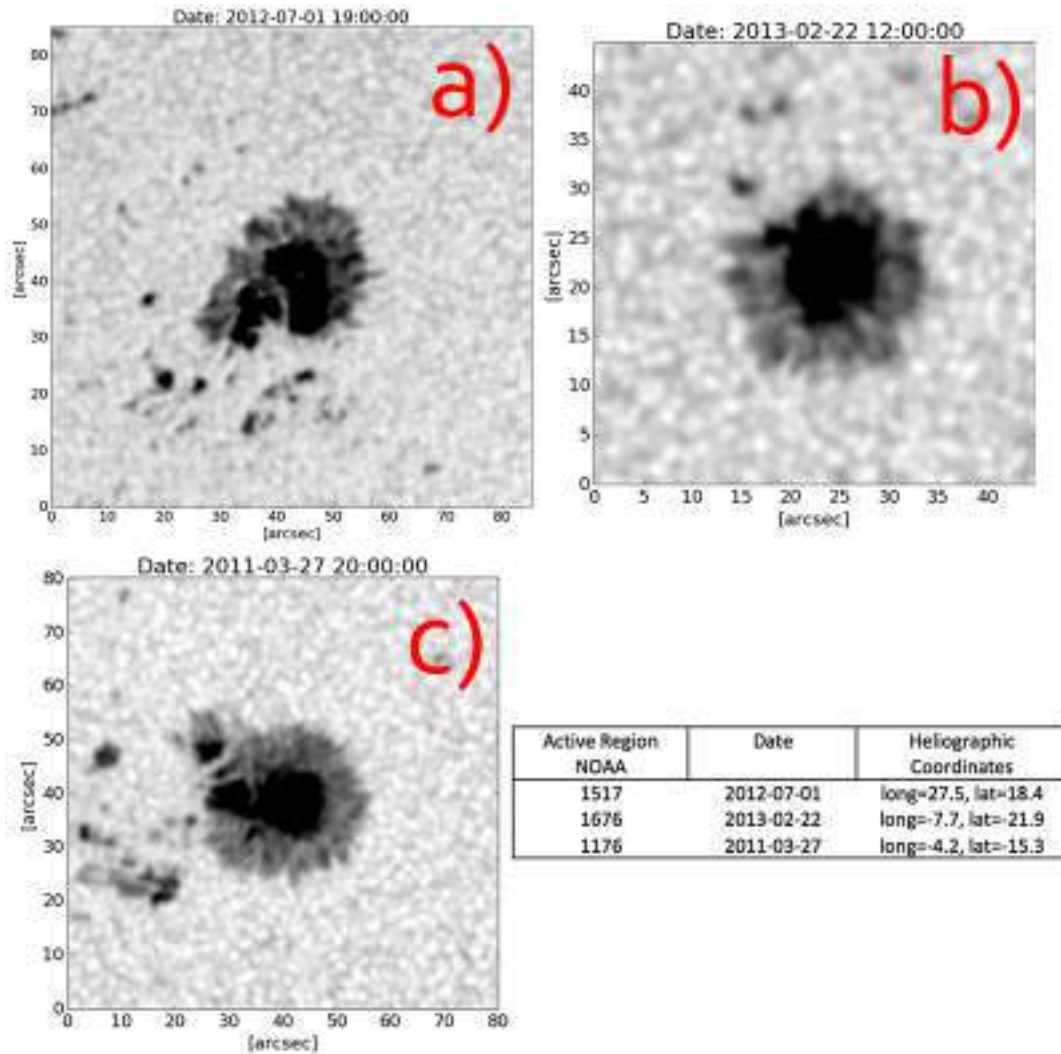


**Figure 5-1.:** The three sunspots of ARs 1517, 1676 and 1176. The table on the lower right corner contains characteristics for each AR.

## De-projection

Due to the studied sunspots being distributed in different regions along the solar disk<sup>1</sup> (the positions are given in HelioGraphic (HG) coordinates), the proper motions calculated with the LCT technique are actually projections of the “real” horizontal velocities of the sunspot on the perpendicular plane of the LOS. For this reason, it is necessary to de-project the tangent surface to the center of the sunspot plane to make a good analysis of the behavior of these displacements obtained with the LCT algorithm.

Considering Fig. (5-2) (extracted from [Vargas Domínguez, 2009]) a coordinate system SX,

<sup>1</sup>They are not exactly positioned in the center of the solar disk.

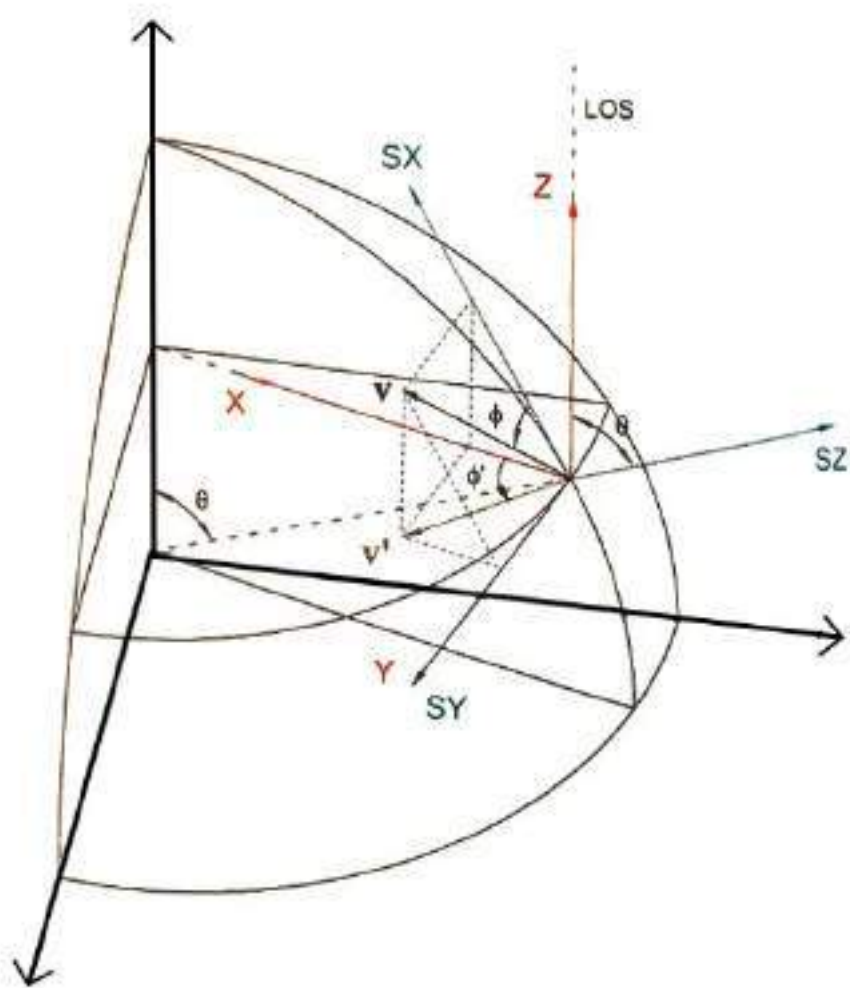


**Figure 5-2.**: Representation of both coordinate eigensystems of the sunspot. The first one is describing the system coordinate over the sunspot, with the SZ-axis normal to the tangent surface on the center of the sunspot. The second one describes the coordinate system for the observer with the Z-axis coinciding with the LOS. Taken from [Vargas Domínguez, 2009]).

SY and SZ, which we call SS (Sunspot System) where the SZ axis is normal to the tangent surface, is assumed for each sunspot.

While the real vectors of the velocity field  $v(v, \phi)$  are determined on the plane formed by the SX- and SY-axis, the projected velocity field  $v'(v', \phi')$  is the only one we can directly determine on the X-Y plane. However, it is possible to construct a transformation that maps the coordinates of the projection into the sunspot plane coordinates. Based on Fig. (5-2), we establish a relationship given by Eq. (5-1) and (5-2) between the magnitudes and angles ( $v(v, \phi) \rightarrow v'(v', \phi')$ ) which allows to find a suitable de-projection for our observations. These equations are transcribed from [Vargas Domínguez, 2009].

$$v'^2 = (v \sin \phi)^2 + (v \cos \phi \cos \theta)^2 = v^2(\sin^2 \phi + \cos^2 \phi \cos^2 \theta) \quad (5-1)$$

$$\tan \phi' = \frac{v \sin \phi}{v \cos \phi \cos \theta} = \frac{\tan \phi}{\cos \theta} \quad (5-2)$$

### 5.3. Masking Velocities to outline Moat Flows

In [Vargas Domínguez, 2009] a masking method has been proposed to find the moat flows which we will employ in this work.

As mentioned in the previous section to obtain a “more realistic” determination of photospheric plasma displacements around sunspots it is necessary to compute velocity maps and de-project them for each AR.

In Eq. (5-1 & 5-2) the values for the angles are expressed in HelioGraphic coordinates. This heliographical position is taken at the center of the FOV. Moreover, we assume that it shows only small changes within the entire FOV. After that, we will use a threshold of  $\sim 0.2$  km s $^{-1}$  which we defined as the best lower limit for the moat flows.

In our work we will use this threshold value, whereas in [Vargas Domínguez, 2009] the authors used a different threshold because the conditions of observations and data were different.

The reason for using this particular threshold is that it was easier to visually identify radial outflows around the sunspots compared to other regions in the FOV. The different stages of the whole masking treatment are summarized and described as follows:

1. We selected a FOV close to the sunspot which is smaller than the original FOV (to remove edge effects).
2. A binary mask is created where sunspots and pores are masked. This is done by intensity thresholding of the umbra and penumbra.
3. The proper motions are computed using the LCT algorithm; the velocity field is masked using a binary mask to plot the flow map within regions showing the granulation pattern.
4. The necessary and discussed de-projections are calculated by using Eqs. (5-1 & 5-2) to determine the de-projected vector map, represented in a gray-scale map. The color-code represents the velocity magnitudes in  $\text{km s}^{-1}$ .
5. Using an intensity threshold, we create a new binary mask where all the de-projected velocities with values over  $0.2 \text{ km s}^{-1}$  are set to “1” and all the rest to “0”.
6. The newly created mask is then applied to the flow map calculated in item 3) obtaining the velocity field for those velocities with magnitudes greater than  $0.2 \text{ km s}^{-1}$ . In a next step we can visually identify the radially outward directed flows within this flow map. These flows correspond to the previously mentioned in section 5.1.
7. Finally, we create another mask which will only show the radial flows found visually in the item above and plot this new flow map to generate a flow map with moat regions.

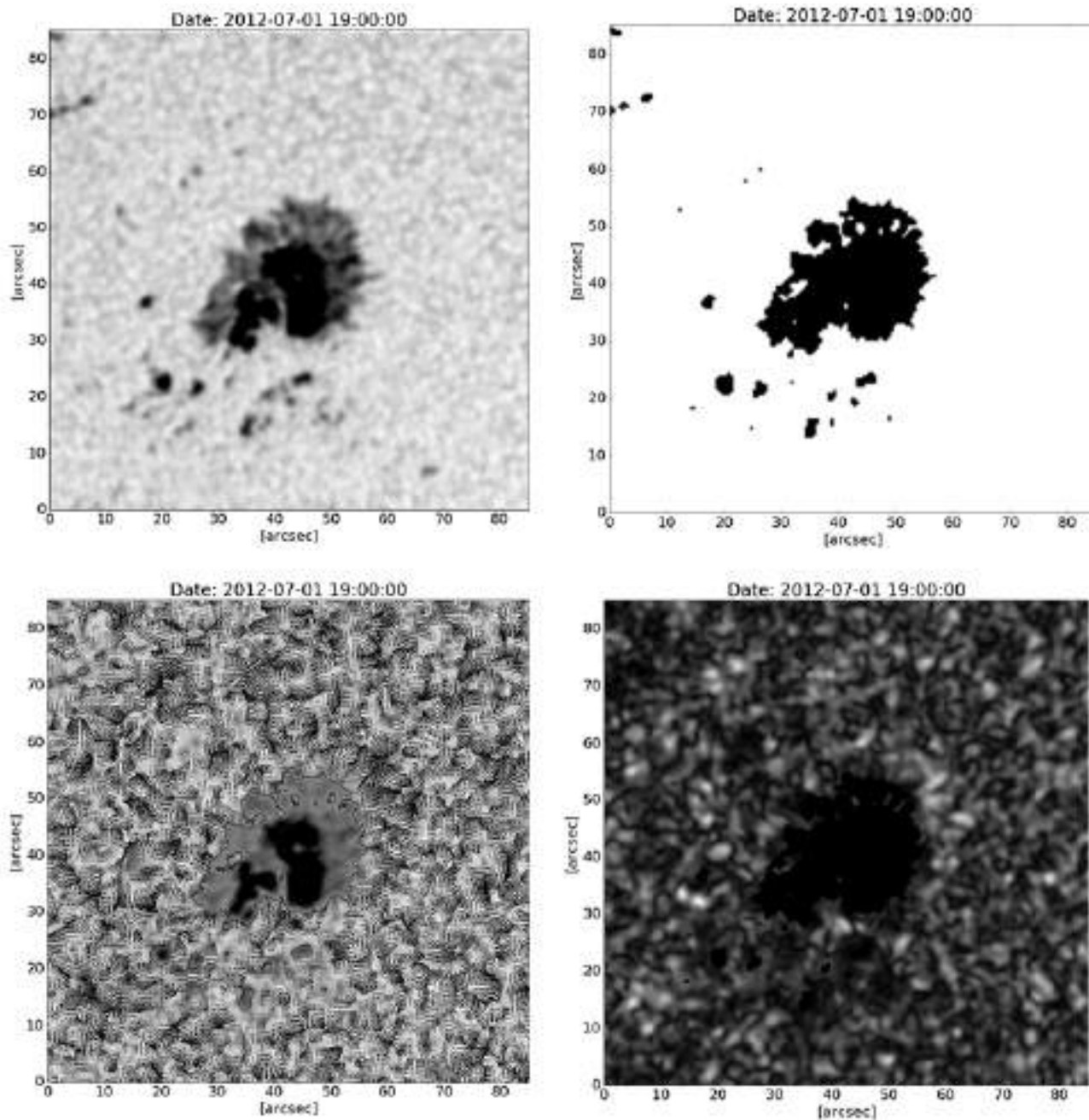


**Figure 5-3.:** Different processing steps for the analysis of moat flows. 1) FOV; 2) masking the sunspot; 3) flow map over the granular area; 4) de-projection of the velocity field.

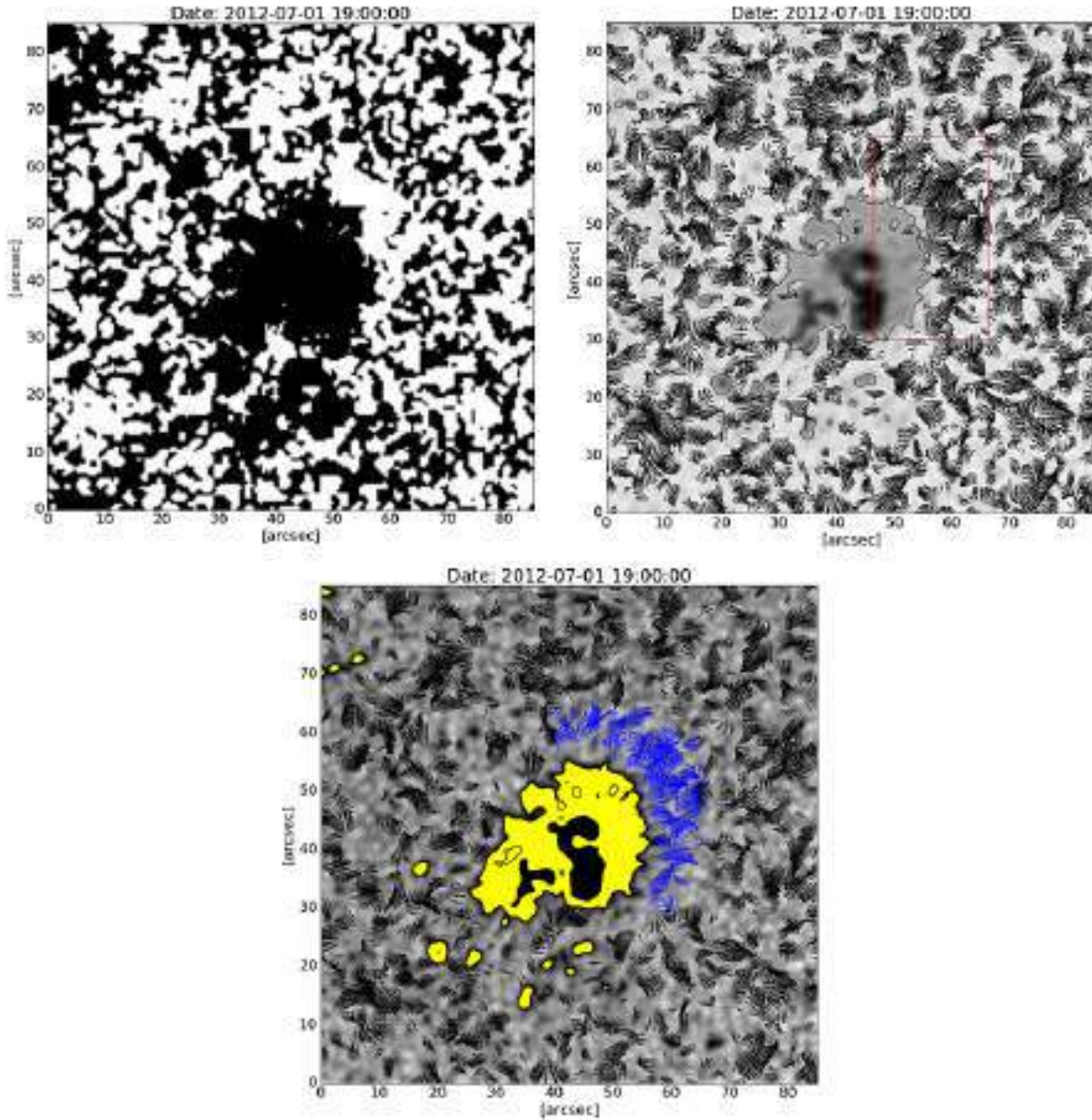


**Figure 5-4.**: The final processing steps for the detection of the moat flows. 5) mask, using the threshold proposed for this work over the de-projected map; 6) masking the flow map with the outcome of process step; 7) covering with blue vectors the selected masked moat flows.

## 5.4. Moat Flows around Sunspots

This analysis was made by applying the LCT technique to calculate the velocity fields around selected sunspots using different masks. We use different temporal series with lengths of days. A  $FWHM = 1.5$  arcsec tracking window is used to calculate the flow maps over a temporal average of one hour. Figures (5-3 & 5-4) show all the previously described steps, also suggested by [Vargas Domínguez, 2009]. The existence of radial outward flows coincide with the moat flows description. For easier distinction purposes, the penumbra region was colored in yellow whereas the umbra is shown in solid black. The blue vectors field represents the moat flows obtained with the threshold of  $v > 0.2 \text{ km s}^{-1}$  derived from the de-projected magnitudes map. Figure (5-5) shows clear radial displacements. This is in perfect agreement with the statement given in [Vargas Domínguez, 2008] where the author claims that if there is no penumbra surrounding the whole umbra, one would not be able to detect any moat flows. This is in strong contrast to the statement of [Strecker et al., 2015]. These authors stated that in this particular region they found moat flows where there is no penumbra using spectropolarimetric techniques. Figure (5-6) is an excellent example for such flows around sunspots without full penumbra around the umbra. These flows show even a shape resembling that of the penumbra. The AR 1517 shows a similar behavior, but in some regions, even for those where a penumbra exists, it is not clear that certain proper motions are linked to moat flows. A reason for this might be that the penumbra is not directed radially outward from the umbra in these areas and thus it can produce a different flow pattern within the surrounding granulation.

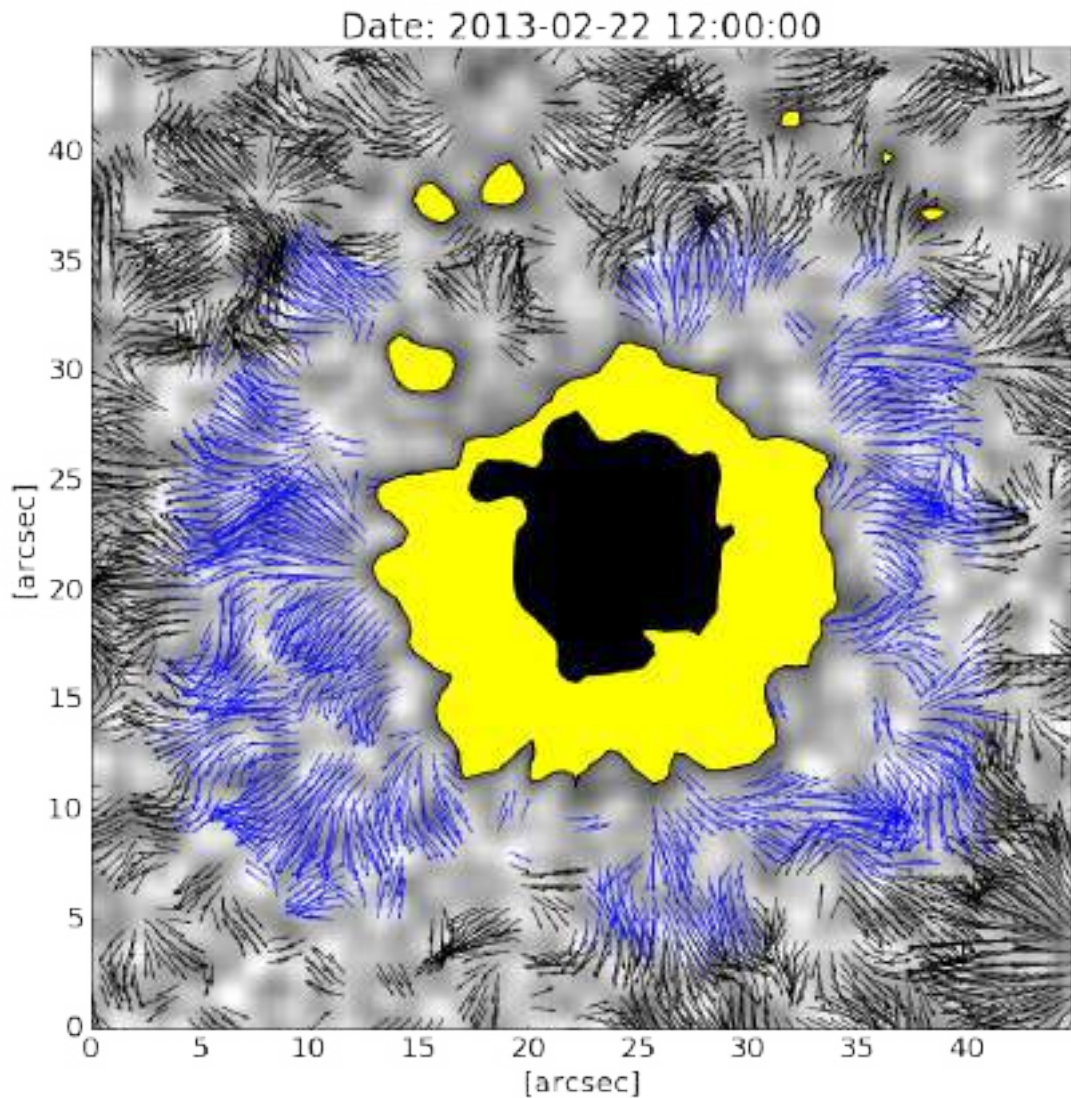


**Figure 5-5.:** AR 1676: This active region was chosen to compare with the work of [Strecker et al., 2015] in which the authors claim that for this particular sunspot moat flows exist, even when the sunspot does not display a penumbra.

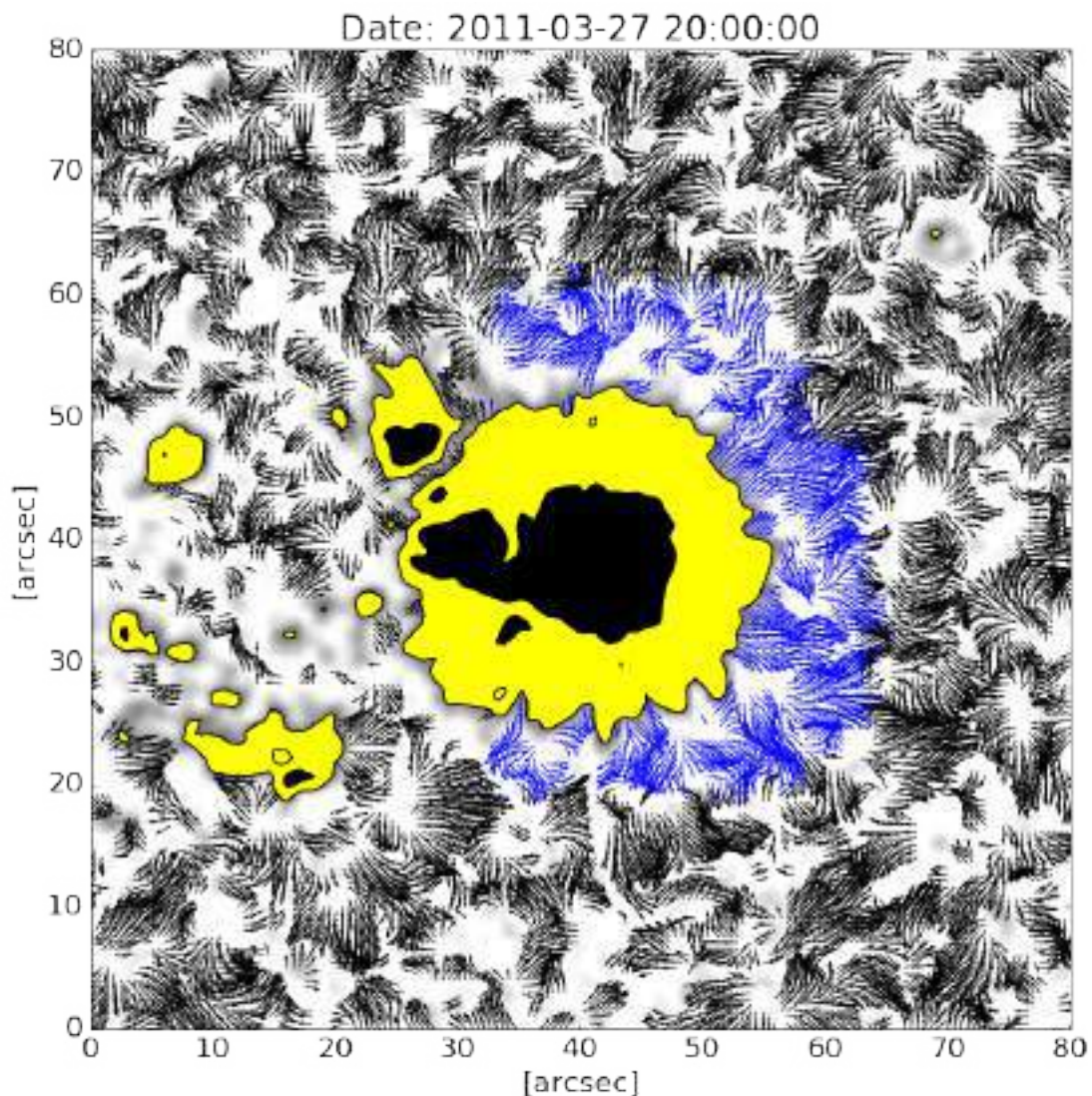


**Figure 5-6.:** AR 1176: This active region shows a perfect behaviour of moat flows at the places where a penumbra exists.

## 6. Summary

This thesis work is devoted to the observation and analysis of solar active regions. In particular, we studied the dynamic behavior of the plasma around sunspots and solar pores during the whole evolution at the photospheric level. For this aim we analyzed data obtained by the space telescope Solar Dynamics Observatory (SDO). The data, firstly, are corrected with the methods described in Chapter 4 of this document, thus generating in this way time series of the evolution of active regions comprising their formation, stability and decay phase.

Local Correlation Tracking (LCT) techniques have been used to infer proper motions of structures within the field of view. For the optimal development of the present work, a Graphical User Interface (GUI) was developed, which helps to find the best parameters. The GUI shows good results embedding efficiently calculations and graphical results. All graphics and practically the whole analysis were performed using computational tools created in Python programming language as well as specialized libraries for solar data analysis SunPy. LCT algorithms and subfiltering codes to remove p-modes were written, adapted, and improved in Python from original codes in IDL.

We are mainly interested in the photospheric horizontal flows around sunspots and pores at different scales, such as granular scales and mesogranular-sized convective cells. A sample that includes several sunspots which can be continuously monitored during the three evolutionary stages, as well as sunspots with different penumbral configurations were analyzed. In total this amounted to detailed analyses of three active regions covering the full evolution.

Using specific parameters for the LCT technique, one can detect a strong co-temporal correlation between an emergence of mesogranular-sized granules in intensity images, and the emergence of positive magnetic field in line-of-sight (LOS) magnetograms. The movies displaying the evolution of each of the studied regions can be found in the GitHub repository<sup>1</sup>. One of the analyzed cases shows an explosive bubble emerging in the regions where the magnetic field increases. At the same time the active region starts to be formed. Several images, statistical analysis and histograms show the horizontal proper displacements of plasma and magnetic field.

Moreover, three active regions displaying partial penumbrae were studied. From this study the following major results were obtained:

- The reason for using a particular threshold is that it is easier to visually identify radial

---

<sup>1</sup>GitHub repository: <https://www.github.com/Hypnus1803>

outflows around the sunspots compared to other regions in the FOV. This difference may be caused by differences between data sources and data features.

- Moat flows are oriented along the direction of the filaments always outwards from the penumbra.
- Regions next to the core of the umbra which do not display a penumbra, do not show moat flows.
- A special focus was put on a region which was chosen to be compared in full detail with the main findings of [Strecker et al., 2015]. However, using the LCT technique, one can see that there is no evidence for their reported moat flows.

In all studied cases we found evidence for the presence of explosive mesogranular-sized granules. These strong upflowing events seem to initiate, or, to tune down the statement slightly, to start the formation and evolution of the active region. The histograms shown in this work display the plasma behavior during the absence and the presence of the magnetic field showing preferential directions at each phase of the evolutionary stages.

The LCT technique uses parameters directly related with the different features. If we change certain basic parameters, the results will display distinct properties in their dynamic and behavior. It is because of the spatial size of this structure is linked with the apodization window of this technique.

For future results, it is necessary to increase the study to other active regions and the amount of data. If we want to link the results obtained in this work with the “real” behavior of plasma surrounding the sunspots, we need to repeat this analysis in different active regions that support the conclusions here.

On the other hand, the GUI continues to be developed, improving existing tools for easier handling of data, faster access to data, and visualization of the proper motions obtained using the LCT algorithm.

# Bibliography

- [Astropy Collaboration, 2013] Astropy Collaboration, e. a. (2013). Astropy: A community Python package for astronomy. *Astronomy & Astrophysics*, 558:A33.
- [Athay, 1976] Athay, R. G. (1976). *The solar chromosphere and corona: Quiet Sun*. Reidel Publishing Company, Holland.
- [Babcock, 1961] Babcock, H. W. (1961). The Topology of the Sun's Magnetic Field and the 22-YEAR Cycle. *ApJ*, 133:572.
- [Balthasar, 2013] Balthasar, H. e. a. (2013). Properties of a Decaying Sunspot. *Central European Astrophysical Bulletin*, 37:435–446.
- [Bethe, 1939] Bethe, H. A. (1939). Energy Production in Stars. *Physical Review*, 55:434–456.
- [Biermann, 1941] Biermann, L. (1941). Der gegenwärtige Stand der Theorie konvektiver Sonnenmodelle. *Vierteljahrsschrift der Astronomischen Gesellschaft*, 76:194–200.
- [Bonet et al., 1982] Bonet, J. A., Ponz, J. D., and Vazquez, M. (1982). On the width distribution of penumbral filaments in sunspots. *Solar Physics*, 77:69–75.
- [Brandenburg, 2011] Brandenburg, A. e. a. (2011). Detection of negative effective magnetic pressure instability in turbulence simulations. *The Astrophysical Journal Letters*, 740(2):L50.
- [Cheung and Isobe, 2014] Cheung, M. C. M. and Isobe, H. (2014). Flux emergence (theory). *Living Reviews in Solar Physics*, 11(3).
- [Cook et al., 1987] Cook, J. W., Lund, P. A., Bartoe, J.-D. F., Brueckner, G. E., Dere, K. P., and Socker, D. G. (1987). Statistical Properties of Small High-Velocity Events in the Solar Transition Region. In Linsky, J. L. and Stencel, R. E., editors, *Cool Stars, Stellar Systems and the Sun*, volume 291 of *Lecture Notes in Physics*, Berlin Springer Verlag, page 150.
- [Cowling, 1946] Cowling, T. G. (1946). The growth and decay of the sunspot magnetic field. *Monthly Notices of the Royal Astronomical Society*, 106:218.
- [Danilovic, 2010] Danilovic, S. e. a. (2010). Transverse Component of the Magnetic Field in the Solar Photosphere Observed by SUNRISE. *Astrophysical Journal Lectures*, 723:L149–L153.

- [De Pontieu, 2007a] De Pontieu, B. e. a. (2007a). A Tale of Two Spicules: The Impact of Spicules on the Magnetic Chromosphere. *Publications of the Astronomical Society of Japan*, 59:S655–S662.
- [De Pontieu, 2007b] De Pontieu, B. e. a. (2007b). Chromospheric Alfvénic Waves Strong Enough to Power the Solar Wind. *Science*, 318:1574.
- [De Pontieu, 2009] De Pontieu, B. e. a. (2009). Observing the Roots of Solar Coronal Heating in the Chromosphere. *Astrophysical Journal Lectures*, 701:L1–L6.
- [De Pontieu, 2011] De Pontieu, B. e. a. (2011). The Origins of Hot Plasma in the Solar Corona. *Science*, 331:55.
- [del Toro Iniesta, 2001] del Toro Iniesta, J. C. (2001). Sunspot Magnetic Fields. In Mathys, G., Solanki, S. K., and Wickramasinghe, D. T., editors, *Magnetic Fields Across the Hertzsprung-Russell Diagram*, volume 248 of *Astronomical Society of the Pacific Conference Series*, page 35.
- [Deng et al., 2007] Deng, N., Choudhary, D. P., Tritschler, A., Denker, C., Liu, C., and Wang, H. (2007). Flow Field Evolution of a Decaying Sunspot. *ApJ*, 671:1013–1021.
- [Dollfus, 1953] Dollfus, A. (1953). La largeur de la raie 6374Å et la température de la couronne solaire. *Comptes Rendus de l'Académie Des Sciences*, 236:996–998.
- [Dwivedi and Narain, 2006] Dwivedi, B. N. and Narain, U. (2006). *Physics of the Sun and its Atmosphere*. World Scientific, Meerut, India.
- [ESA, 2016] ESA (2016). JHelioviewer. <http://www.jhelioviewer.org/about.html>. Accessed: 2016-09-30.
- [Gilbert et al., 2000] Gilbert, H. R., Holzer, T. E., Burkepile, J. T., and Hundhausen, A. J. (2000). Active and eruptive prominences and their relationship to coronal mass ejections. *ApJ*, 537:503–515.
- [Gombosi, 1998] Gombosi, T. I. (1998). *Physics of the Space Environment*. Cambridge University Press, Cambridge.
- [Grotrian, 1931] Grotrian, W. (1931). Ergebnisse der Potsdamer Expedition zur Beobachtung der Sonnenfinsternis am 9. Mai 1929 in Takengon (Nordsumatra). 6. Mitteilung. Über die Intensitätsverteilung des kontinuierlichen Spektrums der inneren Korona. Mit 8 Abbildungen. (Eingegangen am 27. Juni 1931). *Zeitschrift für Astrophysik*, 3:199.
- [Guerrero and Käpylä, 2011] Guerrero, G. and Käpylä, P. J. (2011). Dynamo action and magnetic buoyancy in convection simulations with vertical shear. *Astronomy & Astrophysics*, 533:A40.

- [Hale, 1908] Hale, G. E. (1908). On the Probable Existence of a Magnetic Field in Sun-Spots. *ApJ*, 28:315.
- [Hale et al., 1919] Hale, G. E., Ellerman, F., Nicholson, S. B., and Joy, A. H. (1919). The Magnetic Polarity of Sun-Spots. *ApJ*, 49:153.
- [Hansen, 1994] Hansen, C. J., K. S. D. (1994). *Stellar Interior Physical Principles, Structure, and Evolution*.
- [Harra, 2000] Harra, L. K. (2000). Explosive events on the sun. *Philosophical Transactions of the Royal Society*, 360:2757–2771.
- [Hathaway, 2000] Hathaway, D. e. a. (2000). The photospheric convection spectrum. *Solar Physics*, 193:299–312.
- [Hathaway, 2015] Hathaway, D. H. (2015). The solar cycle. *Living Reviews in Solar Physics*, 12(1):1–87.
- [Hathaway et al., 2013] Hathaway, D. H., Upton, L., and Colegrove, O. (2013). Giant Convection Cells Found on the Sun. *Science*, 342:1217–1219.
- [Howard, 1992] Howard, R. F. (1992). The growth and decay of sunspot groups. *solphys*, 137:51–65.
- [Howard et al., 1990] Howard, R. F., Harvey, J. W., and Forgach, S. (1990). Solar surface velocity fields determined from small magnetic features. *solphys*, 130:295–311.
- [Hundhausen, 1999] Hundhausen, A. (1999). Coronal Mass Ejections. In Strong, K. T., Saba, J. L. R., Haisch, B. M., and Schmelz, J. T., editors, *The many faces of the sun: a summary of the results from NASA's Solar Maximum Mission.*, page 143.
- [Hunter, 2007] Hunter, J. D. (2007). Matplotlib: A 2d graphics environment. *AIP - Computing in Science & Engineering*, 9.
- [Hurlburt and Rucklidge, 2000] Hurlburt, N. E. and Rucklidge, A. M. (2000). Development of structure in pores and sunspots: flows around axisymmetric magnetic flux tubes. *Monthly Notices of the Royal Astronomical Society*, 314:793–806.
- [Jones et al., 01 ] Jones, E., Oliphant, T., Peterson, P., et al. (2001–). SciPy: Open source scientific tools for Python. [Online; accessed 2016-08-24].
- [Jurčák, 2014] Jurčák, J. e. a. (2014). Orphan penumbrae: Submerging horizontal fields. *Astronomy & Astrophysics*, 564:A91.
- [Kálmán, 2001] Kálmán, B. (2001). Submergence of magnetic flux in interaction of sunspot groups. *Astronomy & Astrophysics*, 371:731–737.

- [Keenan, 1938] Keenan, P. C. (1938). Dimensions of the Solar Granules. *ApJ*, 88:360.
- [Krause and Ruediger, 1975] Krause, F. and Ruediger, G. (1975). On the turbulent decay of strong magnetic fields and the development of sunspot areas. *solphys*, 42:107–119.
- [Leighton, 1964] Leighton, R. B. (1964). Transport of Magnetic Fields on the Sun. *ApJ*, 140:1547–1562.
- [Leighton, 1969] Leighton, R. B. (1969). A Magneto-Kinematic Model of the Solar Cycle. *ApJ*, 156:1–26.
- [Lisle et al., 2004] Lisle, J. P., Rast, M. P., and Toomre, J. (2004). Persistent North-South Alignment of the Solar Supergranulation. *ApJ*, 608:1167–1174.
- [Loptien, 2016] Loptien, B. e. a. (2016). The shrinking sun: A systematic error in local correlation tracking of solar granulation. *Astronomy & Astrophysics*, 590:A130.
- [Machado et al., 1980] Machado, M. E., Avrett, E. H., Vernazza, J. E., and Noyes, R. W. (1980). Semiempirical models of chromospheric flare regions. *ApJ*, 242:336–351.
- [Mark Summerfield, 2007] Mark Summerfield (2007). *Rapid GUI programming with Python and Qt*. Prentice Hall.
- [Maunder, 1904] Maunder, E. W. (1904). Note on the distribution of sun-spots in heliographic latitude, 1874-1902. *Monthly Notices of the Royal Astronomical Society*, 64:747–761.
- [McIntosh, 2011] McIntosh, S. W. e. a. (2011). Alfvénic waves with sufficient energy to power the quiet solar corona and fast solar wind. *Nature*, 475:477–480.
- [Mitalas and Sills, 1992] Mitalas, R. and Sills, K. R. (1992). On the photon diffusion time scale for the sun. *Astrophysical Journal*, 401:759–760.
- [Molowny-Horas, 1994] Molowny-Horas, R. (1994). Proper motion measurements of umbral and penumbral structure. *solphys*, 154:29–39.
- [Moses et al., 1994] Moses, D., Cook, J. W., Bartoe, J.-D. F., Brueckner, G. E., Dere, K. P., Webb, D. F., Davis, J. M., Harvey, J. W., Recely, F., Martin, S. F., and Zirin, H. (1994). Solar fine scale structures in the corona, transition region, and lower atmosphere. *ApJ*, 430:913–924.
- [Mullan, 2010] Mullan, D. J. (2010). *Physics of the Sun- A first course*. CRC Press, U. S. A.
- [November and Simon, 1988] November, L. J. and Simon, G. W. (1988). Precise proper-motion measurement of solar granulation. *ApJ*, 333:427–442.

- [November, 1981] November, L. J. e. a. (1981). The detection of mesogranulation on the sun. *Astrophysical Journal Lectures*, 245:L123–L126.
- [Oda, 1984] Oda, N. (1984). Morphological study of the solar granulation. III - The meso-granulation. *solphys*, 93:243–255.
- [Palacios, 2012] Palacios, J. e. a. (2012). Magnetic field emergence in mesogranular-sized exploding granules observed with sunrise/IMaX data. *Astronomy & Astrophysics*, 537:A21.
- [Papoulis and Pillai, 2002] Papoulis, A. and Pillai, U. (2002). *Probability, Random Variables and Stochastic Processes*. McGraw Hill, fourth edition.
- [Parker, 1970] Parker, E. N. (1970). The Origin of Solar Magnetic Fields. *Annual Review of Astronomy and Astrophysics*, 8:1.
- [Parker, 1988] Parker, E. N. (1988). Nanoflares and the solar X-ray corona. *ApJ*, 330:474–479.
- [Petrovay, 2010] Petrovay, K. (2010). Solar Cycle Prediction. *Living Reviews in Solar Physics*, 7(6).
- [Potts, 2003] Potts, H. E. e. a. (2003). Reduction of interpolation errors when using local correlation tracking for motion detection. *solphys*, 217:69–78.
- [Rast, 1995] Rast, M. P. (1995). On the nature of 'exploding' granules and granule fragmentation. *ApJ*, 443:863–868.
- [Rieutord and Rincon, 2010] Rieutord, M. and Rincon, F. (2010). The sun's supergranulation. *Living Reviews in Solar Physics*, 7(2).
- [Roudier et al., 2003] Roudier, T., Lignieres, F., Rieutord, M., Brandt, P. N., and Malherbe, J. M. (2003). Families of fragmenting granules and their relation to meso- and supergranular flow fields. *Astronomy & Astrophysics*, 409:299–308.
- [Roudier and Muller, 2004] Roudier, T. and Muller, R. (2004). Relation between families of granules, mesogranules and photospheric network. *Astronomy & Astrophysics*, 419:757–762.
- [Roudier, 1999] Roudier, T. e. a. (1999). Determination of horizontal velocity fields at the sun's surface with high spatial and temporal resolution. *Astronomy & Astrophysics*, 349:301–311.
- [Rutten, 2002] Rutten, R. J. (2002). Solar Atmosphere Models. *Journal of Astronomical Data*, 8(8).

- [Schmidt, 1991] Schmidt, H. U. (1991). Sunspots. *Geophysical and Astrophysical Fluid Dynamics*, 62:249–270.
- [Schmidtke, 2015] Schmidtke, G. (2015). History of extreme ultraviolet solar measurements in XX-XXI centuries: from balloons to the International Space Station as instrumental platforms. *Journal of Optical Technology*, 82:185–196.
- [Schrijver, 2001] Schrijver, C. J. (2001). Catastrophic cooling and high-speed downflow in quiescent solar coronal loops observed with TRACE. *solphys*, 198:325–345.
- [Schüssler et al., 2003] Schüssler, M., Shelyag, S., Berdyugina, S., Vögler, A., and Solanki, S. K. (2003). Why Solar Magnetic Flux Concentrations Are Bright in Molecular Bands. *Astrophysical Journal Lectures*, 597:L173–L176.
- [Schwabe, 1844] Schwabe, M. (1844). Sonnenbeobachtungen im Jahre 1843. Von Herrn Hofrat Schwabe in Dessau. *Astronomische Nachrichten*, 21:233.
- [Schwarzschild, 1958] Schwarzschild, M. (1958). *Structure and evolution of the stars*. Princeton U.P., Princeton.
- [Sheeley, 1969] Sheeley, Jr., N. R. (1969). The Evolution of the Photospheric Network. *solphys*, 9:347–357.
- [Shibata and Magara, 2011] Shibata, K. and Magara, T. (2011). Solar flares: Magnetohydrodynamic processes. *Living Reviews in Solar Physics*, 8(6).
- [Simnett et al., 1997] Simnett, G. M., Alissandrakis, C. E., and Vlahos, L., editors (1997). *Solar and Heliospheric Plasma Physics*, volume 489 of *Lecture Notes in Physics*, Berlin Springer Verlag.
- [Simon et al., 1991] Simon, G. W., Title, A. M., and Weiss, N. O. (1991). Modeling mesogranules and exploders on the solar surface. *ApJ*, 375:775–788.
- [Simon and Weiss, 1991] Simon, G. W. and Weiss, N. O. (1991). Convective structures in the sun. *Monthly Notices of the Royal Astronomical Society*, 252:1P–5P.
- [Solanki, 2003] Solanki, S. K. (2003). Sunspots: An overview. *Astronomy & Astrophysics Review*, 11:153–286.
- [Steiner, 2000] Steiner, O. (2000). *Chromosphere: Magnetic Canopy*.
- [Strecker et al., 2015] Strecker, H., Schmidt, W., and Bello González, N. (2015). The evolution of the moat flow around sunspots.

- [SunPy Community et al., 2015] SunPy Community, Mumford, S. J., Christe, S., Perez-Suarez, D., Ireland, J., Shih, A. Y., Inglis, A. R., Liedtke, S., Hewett, R. J., Mayer, F., Hughitt, K., Freij, N., Meszaros, T., Bennett, S. M., Malocha, M., Evans, J., Agrawal, A., Leonard, A. J., Robitaille, T. P., Mampaey, B., Campos-Rozo, J. I., and Kirk, M. S. (2015). SunPy-Python for solar physics. *Computational Science and Discovery*, 8(1):014009.
- [Thomas, 2010] Thomas, J. H. (2010). Theoretical Models of Sunspot Structure and Dynamics. *Astrophysics and Space Science Proceedings*, 19:229–242.
- [Thomas and Weiss, 1992] Thomas, J. H. and Weiss, N. O. (1992). The theory of sunspots. In Thomas, J. H. and Weiss, N. O., editors, *NATO Advanced Science Institutes (ASI) Series C*, volume 375 of *NATO Advanced Science Institutes (ASI) Series C*, pages 3–59.
- [Title et al., 1986] Title, A. M., Tarbell, T. D., Simon, G., and the SOUP Team (1986). White-light movies of the solar photosphere from the soup instrument on spacelab 2. *Advances in Space Research*, 6:253–262.
- [Title et al., 1989] Title, A. M., Tarbell, T. D., Topka, K. P., Ferguson, S. H., Shine, R. A., and SOUP Team (1989). Statistical properties of solar granulation derived from the SOUP instrument on Spacelab 2. *ApJ*, 336:475–494.
- [Utz et al., 2014] Utz, D., del Toro Iniesta, J. C., Bellot Rubio, L. R., Jurčák, J., Martínez Pillet, V., Solanki, S. K., and Schmidt, W. (2014). The Formation and Disintegration of Magnetic Bright Points Observed by Sunrise/IMaX. *ApJ*, 796:79.
- [Utz et al., 2009] Utz, D., Hanslmeier, A., Möstl, C., Muller, R., Veronig, A., and Muthsam, H. (2009). The size distribution of magnetic bright points derived from Hinode/SOT observations. *Astronomy & Astrophysics*, 498:289–293.
- [van der Walt et al., 2011] van der Walt, S., Colbert, S. C., and Varoquaux, G. (2011). The numpy array: A structure for efficient numerical computation. *AIP - Computing in Science & Engineering*, 13:22–30.
- [Vargas Domínguez, 2009] Vargas Domínguez, S. (2009). *Study of horizontal flows in solar active regions based on high-resolution image reconstruction techniques*. PhD thesis, PhD Thesis, 2009.
- [Vargas Domínguez et al., 2012] Vargas Domínguez, S., van Driel-Gesztelyi, L., and Bellot Rubio, L. R. (2012). Granular-Scale Elementary Flux Emergence Episodes in a Solar Active Region. *solphys*, 278:99–120.
- [Vargas Domínguez, 2008] Vargas Domínguez, S. e. a. (2008). Moat Flow in the Vicinity of Sunspots for Various Penumbra Configurations. *ApJ*, 679:900–909.

- [Verma et al., 2012] Verma, M., Balthasar, H., Deng, N., Liu, C., Shimizu, T., Wang, H., and Denker, C. (2012). Horizontal flow fields observed in Hinode G-band images. II. Flow fields in the final stages of sunspot decay. *Astronomy & Astrophysics*, 538:A109.
- [Wang et al., 2002] Wang, T., Solanki, S. K., Curdt, W., Innes, D. E., and Dammasch, I. E. (2002). Doppler Shift Oscillations of Hot Solar Coronal Plasma Seen by SUMER: A Signature of Loop Oscillations? *Astrophysical Journal Lectures*, 574:L101–L104.
- [Yi et al., 1992] Yi, Z., Darvann, T. A., and Molowny Horas, R. L. (1992). Software for solar image processing. Proceedings. *LEST Foundation, Technical Report*, 56.
- [Zwaan, 1978] Zwaan, C. (1978). On the Appearance of Magnetic Flux in the Solar Photosphere. *solphys*, 60:213–240.